METALLIC LINE PROFILES IN CEPHEID VARIABLES

A THESIS
SUBMITTED IN PARTIAL FULFILMENT
OF THE REQUIREMENTS FOR THE DEGREE
OF
DOCTOR OF PHILOSOPHY IN ASTRONOMY
IN THE
UNIVERSITY OF CANTERBURY
BY

MICHAEL D. ALBROW

University of Canterbury
1994

Contents

List of Tables

List of Figures

Abstract

A grid of synthetic line profiles incorporating a new treatment of macroturbulence is calculated for a Cepheid atmosphere in radial motion. Projection factors are determined to be up to 10 per cent higher than previous calculations. A relationship is found between the asymmetry of the line profiles and γ, the ratio of pulsational velocity to line half-width at half-height.

A programme of high-resolution spectroscopic observations of Cepheids has been carried out at Mt John University Observatory for several years. Radial velocities and asymmetries have been measured for selected metallic lines and the asymmetries compared with those of the synthetic profiles.

The line profiles from the observations show a larger asymmetry than the synthetic profiles at phases of inward pulsational velocity. The asymmetry at phases of outward velocity is smaller and in agreement with the synthetic profiles for some Cepheids. However, for others the asymmetry at phases of outward pulsation is in the direction expected for inward motion.

A hydrodynamic model of an 11-day Cepheid has been calculated. A set of flux-constant, line-blanketed model atmospheres have been converged based on the density structure predicted by the hydrodynamic model.

A method for calculating the source function and mean intensity in a moving atmosphere has been developed and incorporated into the ATLAS code. Synthetic line profiles have been calculated from the set of dynamic model atmospheres.

A function giving the contribution of different atmospheric layers to the absorption of a spectral line has been derived. Flux contribution contour diagrams based on this function have been introduced and used to study the effects that velocity fields in a stellar atmosphere have on spectral line formation.

In the presence of a constant velocity, the trailing wing of a spectral line is no longer formed at deep atmospheric layers close to the continuum. The presence of

a velocity gradient can have a large effect on the region of line formation. Multiple centres of absorption, separated in wavelength and in physical depth, can occur which will not usually be resolved by observation. The use of spectral lines of different strength and excitation potential to probe depth-dependent phenomena in pulsating stars, will give incorrect results if based on static models of line formation depths.

Projected radial velocities of spectral lines, synthesised from the set of dynamic model atmospheres, represent the motion of a mass zone in the hydrodynamic model with an rms error of $\sim$ 1 km s^{-1} if bump phases are excluded. A mapping of the radial velocities to the motion of the photospheric radius has an rms error of $\sim$ 5 km s^{-1}. This is due to a changing phase lag between the photospheric radius and the line formation region. In particular, the radial velocities significantly overestimate the photospheric velocity for $\sim$ 0.1 cycle near radial velocity maximum.

The inverse line asymmetry observed in some Cepheids during phases of expansion may be due to velocity gradients in their atmospheres or to radial macroturbulence. The enhanced asymmetry in Cepheids at contraction phases is most likely due to an increase in anisotropic macroturbulence.

Chapter 1

Introduction

1.1 Historical review

The first recorded observations of Cepheids were in 1784 and 1785 when Edward Piggot and John Goodricke respectively discovered the variability of η Aquilae and δ Cephei. Up until the early years of the 20th century, Cepheid light curves were well observed and the variability thought to be the result of binary motion. The first detection of radial velocity variations was by Belopolsky (1895) for δ Cephei (as reported by Hearnshaw 1986). Radial velocities were recorded for several other Cepheids over the next decade but the variations were still thought to be the result of binary motion. Orbital solutions were often calculated and theories of tidal distortion invoked to explain the radial velocity curves (Campbell 1901).

From 1910 onwards, the pulsation hypothesis became more accepted as surface temperature changes were detected. In 1912, Henrietta Leavitt discovered a correlation between the brightnesses and periods of variable stars in the Small Magellanic Cloud. Because these stars were all at the same distance, this implied a relation between the periods and luminosities. A theoretical foundation for stellar pulsation came with the work of Eddington (1918a, b) who studied linear adiabatic radial pulsations and derived the period – mean density relation.

The main importance of Cepheids to modern astronomy is in their use as relative and absolute distance indicators to nearby galaxies. Reviews of the history and current status of Cepheid period-luminosity and period-luminosity-colour relations have been given by Fernie (1969) and Feast & Walker (1987).

A primary method for determining radii and distances for Cepheid variables,

and hence calibrating the period-luminosity and period-luminosity-colour relations, is the Baade-Wesselink technique (Wesselink 1946). Reviews of the Baade-Wesselink method and its different formulations have been given by Gautschy (1987) and Moffett (1989). There are three main versions of the method in use today; the maximum likelihood method (Balona 1977), the surface brightness method (Barnes, Evans & Parsons 1976, Barnes et al. 1977), and the CORS method (Caccin et al. 1981). The three methods differ in their use of colour photometry but are essentially equivalent in their use of spectroscopic measurements to derive absolute radius changes. Stellar radial velocities are measured, converted into pulsational velocities, and integrated with respect to time, to provide the total distance the line forming region of the atmosphere has moved through. The relative change in radius of the star can be inferred from changes in luminosity and temperature derived from colour photometry. These relative and absolute changes in radius together give the radius of the star and hence its absolute magnitude and distance. The major source of error in Baade-Wesselink applications has always been the determination of effective temperatures from photometric colours. The advent of optical interferometric methods for determining angular diameters will replace the photometric aspects of the Baade-Wesselink method. It is appropriate that further study be made of the uncertainties in the spectroscopic determination of pulsational velocities.

The traditional assumption has been that the velocity of the stellar atmosphere is related to the observed radial velocity of absorption lines in the stellar spectra by a simple ratio, the projection factor. This factor is greater than unity because the observed spectral line flux is a sum of the surface intensities over the stellar disk, different parts of which have different velocities in the observer's line of sight.

Asymmetry of metallic lines in Cepheid spectra has been noticed as long ago as the 1950s (van Hoof & Deurinck 1950). Van Hoof & Deurinck's analysis of coudé spectrograms of η Aql revealed visibly asymmetric lines which they found to be consistent with geometric projection of a Gaussian line profile. Indeed, they regarded their observations as evidence of the reality of radial pulsations in Cepheid atmospheres. Since that time, observational studies of the line profiles of Cepheids have concentrated almost exclusively on strong lines, in particular Hα (Rogers & Bell 1968, Wallerstein 1972, 1973). More recently, profile variations of metallic lines in near infrared and optical spectra of several Cepheids have

been reported by Sasselov, Lester & Fieldus (1989), Sasselov & Lester (1990) and Butler (1993). Attempts at determining velocity stratification in Cepheid atmospheres using radial velocity differences between lines of different excitation potential have been made by, for example, Sanford (1956) and Butler (1993).

1.2 Cepheid models

1.2.1 Hydrodynamic models

The first detailed models of Cepheid pulsation were the linear, non-adiabatic calculations of Baker & Kippenhahn (1962, 1965) and Cox (1963). These envelope models were successful in explaining many of the properties of pulsating stars. In particular, the He II and (to a lesser extent) the H I ionisation zones were found to be the driving source for Cepheid pulsations through the κ and γ mechanisms. Linear calculations also answered questions of stability of the star in different pulsation modes, finding many models to be unstable in both the fundamental and first overtone modes.

Nonlinear calculations soon followed (Cox, Brownlee & Eilers 1966, Cox et al. 1966, King et al. 1966, Christy 1967, Stobie 1969a, b, c) enabling investigations of the self-excitation of pulsations, modal selection and the shapes of light and velocity curves. A comprehensive review of the theory of radial stellar pulsation is given by Cox (1974).

1.2.2 Line spectra

It has become commonplace for astronomers to calculate theoretical spectral line profiles based on static model atmospheres. Such calculations are of major use in stellar abundance analyses (Lambert 1968, Lambert & Warner 1968, Gustafsson et al. 1975) and in investigations of stellar populations of galaxies (see the review of Bruzual 1992). Commonly used computer codes for synthesising spectra from static model atmospheres include SPECTRUM (Cottrell & Norris 1978) and SYNTHE (Kurucz 1970) based on Kurucz's model atmosphere code, ATLAS. It is not uncommon for such static model calculations to be used for abundance determinations of Cepheids and other pulsating stars (e.g. Luck & Lambert 1981). These static codes can give accurate results only if there are no velocity gradients in the line forming regions of the stellar atmosphere.

When determining synthetic spectra from dynamic atmospheres, one needs

to consider more carefully the radiative transfer processes. An early formulation of the radiative transfer equations in a non-static medium was given by Chandrasekhar (1945) along with some analytical solutions for idealised situations. In more recent times, numerical techniques have been developed for solution of multi-level non-LTE line transfer problems in moving atmospheres with plane parallel and spherical geometry (Hummer & Rybicki 1968, Kunasz & Hummer 1974). Reformulation of the equations for the comoving frame has been shown to introduce greater computational efficiency (Mihalas, Kunasz & Hummer 1975).

One of the most pressing needs in the study of stellar pulsation is for a hydrodynamic code with a full treatment of radiative transfer. In the absence of such a code, there have been several approaches by different workers in the field. Karp (1975a) used gray radiative transfer for the energy equation of his hydrodynamic code and the integral of the Planck function to compute line profiles (Karp 1973, 1975b). Bowen (1988) added some radiative terms to hydrodynamic models of Mira atmospheres. Bessell et al (1989) used a hydrodynamic code to generate density structures for a Mira model at various phases. A model atmosphere code (Schmid-Burgk & Scholz 1984) was used to calculate temperature structures for those models in spherical geometry. Fokin (1991) has solved the non-LTE transfer equation for a three-level hydrogen atom in a pulsating W Vir model. Sasselov & Raga (1992) have recently produced a stable semi-empirical iterative hydrodynamic code, HERMES, which perhaps represents the best attempt to date at modelling shocked dynamic atmospheres. Applications to Cepheid chromospheres have been reported by Sasselov & Lester (1994a, b, c).

1.2.3 Contribution functions

To study velocities in stellar atmospheres spectroscopically, we require a function which describes the depth of formation of spectral lines. This 'contribution function' gives the relative contribution of different atmospheric layers to an absorption line. This should be distinguished from a contribution function to the emergent intensity as the regions contributing to each of these can be quite different. As discussed by Magain (1986), an extreme example of this occurs for the case of a telluric line, where the region of origin of the intensity of the line (i.e. the stellar photosphere) is clearly different from the region of line opacity (the Earth's atmosphere). Different contribution functions to the depression in emergent intensity have been derived by various authors over the years. Magain

(1986) has shown the shortcomings of these and derived the correct form for the contribution function to the relative depression in intensity.

Some properties of spectral lines, such as asymmetry, are dependent on the line flux profile rather than the emergent intensity profile at any point on the stellar surface. To study the depth dependent effects of such properties, the contribution function to the depression in the spectral line flux is required. An attempt at deriving the contribution function to the relative flux depression was made by Achmad, de Jager & Nieuwenhuijzen (1991), but the transfer equation could not be separated into known and unknown parts.

1.3 Outline of the thesis

This thesis makes an observational and theoretical study of the spectral line profiles of Cepheids.

In Chapter 2 synthetic line profiles for simple radial motion are calculated from a grid of static model atmospheres with effective temperatures and gravities in the range occupied by Cepheids. The line profiles are calculated for an Fe I line and artificial values of $\log gf$ are used to simulate lines of different strength. Macroturbulent broadening is incorporated by considering three different models – isotropic, radial and radial-tangential. Spectral line bisectors are calculated for all of the profiles and are used to determine projection factors and line asymmetries.

Chapter 3 describes the programme of spectroscopic observations of Cepheids carried out at the Mt John University Observatory. Radial velocity curves for the programme stars are determined from bisectors of the 6546 Å Fe I line. Radius and acceleration curves for the stars are calculated by differentiating and integrating Fourier series fits to the radial velocity curves. Asymmetries for the spectral lines are measured and compared with those obtained from the calculations of Chapter 2.

In Chapter 4 a hydrodynamic code is used to create a pulsating photospheric model of a Cepheid. The outermost layers of this hydrodynamic model are extracted at different pulsation phases to create a series of 'snapshots' of the model. A model atmosphere code is used to converge a temperature structure for each 'snapshot'. The assumption is made that the atmosphere can be treated as being in LTE and that spherical extension is small enough that a plane parallel model is adequate. The resulting model atmospheres are compared with static model

atmospheres having the same effective temperatures.

A technique is developed in Chapter 5 for calculating synthetic spectral line profiles from the dynamic model atmospheres calculated in Chapter 4. Bisectors are determined for these synthetic lines and are used to generate radial velocity curves for the model. Acceleration and radius curves are obtained respectively by differentiating and integrating the radial velocity curves and are then compared to the curves obtained observationally (Chapter 3).

In Chapter 6 a function is derived that gives the contribution of different layers to the depression in the spectral line flux. A 'flux contribution contour' diagram is introduced as a means of representing the location of the absorption in optical depth and wavelength space. Such diagrams are used to compare the location of line absorption centres with velocity fields in the dynamic model atmospheres. The radial velocities calculated in Chapter 5 are compared with the actual velocities of zones in the hydrodynamic model and also with the velocity of the photosphere. The differences between these velocities are discussed from a Baade-Wesselink perspective. Calculations of line profiles are made based on different atmospheric velocity fields to further study the effect of velocity gradients on the asymmetry of spectral lines.

Much of the material in Chapters 2 and 3 of this thesis has previously been published as Albrow & Cottrell (1994). Some of Chapter 3 has also appeared in Wallerstein et al. (1992).

Chapter 2

Projection factors and asymmetries from constant velocity calculations

In this chapter we make a comprehensive study of the projection factors and asymmetries of weak spectral lines calculated from model atmospheres with effective temperatures in the range 4500K - 6000K and log g in the range 1.0 - 2.0. Several different models for macroturbulent broadening are considered. In later chapters we will compare these results with observed spectral lines and lines synthesised from dynamic models.

The projection factor calculations which are most often used by researchers today are those of Parsons (1972), Karp (1975b) and Hindsley & Bell (1986). Parsons (1972) made calculations based on two model atmospheres and two Fe I lines, an Fe II line and Hγ. Projection factors were derived for pulsational velocities of $\sim$ 20 and 40 km s^{-1} and were found to be a function of γ, the ratio of pulsational velocity to line half-width. A value of 1.31 for the projection factor was recommended based on a likely maximum value for γ. Karp (1975b) used three grey atmospheric models and calculated a number of weak and strong line profiles. A weaker dependence on γ was found for the projection factor than that of Parsons (1972), especially when radial velocities were measured at the half-intensity point in the spectral line.

More recently, Hindsley & Bell (1986) have derived projection factors for use when radial velocities are measured by cross correlation with a mask. A computer generated mask similar to that used in the radial velocity spectrometer

at the South African Astronomical Observatory was created. The mask contained 197 lines each of width 0.61 Å. This was cross correlated with synthetic spectra from a range of model atmospheres. No correction was made for differential Doppler shifts across the mask. Values ranging from 1.31 to 1.47 were found for the projection factor depending on the effective temperature, the pulsational velocity and the systemic velocity of the star as well as the method used to determine the radial velocity from the cross correlation dip. Many authors have subsequently extrapolated the scope of the values calculated in this paper by using them for velocities measured by radial velocity spectrometers of different design (e.g. Barnes et al. 1993) or by digital cross correlation of spectra (Côte et al. 1991).

2.1 Line profile calculations

For the calculations presented in this chapter, twelve model atmospheres, with the temperatures and gravities given in Table 2.1, were taken from a recent grid of models (Kurucz 1991, private communication, 1991, 1992). Line profiles were calculated by the method described below for an Fe I line at 6546 Å, with an excitation potential $\chi = 2.76$ eV. In order to consider lines of different strength, several artificial gf values were used for each model.

Since these computations were made, a revised grid of model atmospheres has been issued by Kurucz. (The new solar composition models are on Kurucz CD#13.) Test line profiles have been calculated with these new models for $T_{\rm eff} = 4500$ K and 6000 K and for $\log g = 1.0$ and 2.0. These profiles are identical with those calculated from the earlier grid of models.

For each model atmosphere and gf value, the computer program SPECTRUM (Cottrell and Norris, 1978), an ATLAS derivative, was used to calculate synthetic intensity spectra for 20 equally spaced values of $\mu = \cos\theta$, where θ is the angle from the centre of disc to a point on the stellar surface. Two values of microturbulence, $\xi = 2.5$ km s^{-1} and $\xi = 5.0$ km s^{-1}, were used for each calculation.

Different authors have included macroturbulent effects in different ways in their line profile calculations. Parsons (1972) simply broadened the flux profiles (obtained after disc integration) by convolution with a Gaussian. This represents isotropic macroturbulence which is not observed in stellar atmospheres (Gray 1992). Hindsley & Bell (1986) make no mention of any broadening applied. Karp (1975) convolved flux profiles with a rotational broadening function with

$v \sin i = 10$ km s^{-1}. This was justified by stating that Abt (1958) had shown that this rotation could not be distinguished from a macroturbulence of 7 km s^{-1}, a value typical for Cepheids. In fact, Abt (1958) only compared the effects of radial macroturbulence and rotation, and only for the case where the unbroadened profile is symmetric, i.e. for a non-pulsating star. These effects are not the same for an atmosphere with a radial motion. Duval & Karp (1978) have shown that the effects of rotation on a line profile from a pulsating atmosphere could not be calculated by simply convolving it with a rotational broadening function.

The flux, F_ν, is formed by integrating over the observable stellar hemisphere. Thus

$$F_\nu = 2\pi \int_0^1 I_\nu \mu d\mu \tag{2.1}$$

$$= 2\pi \int_0^1 I_\nu^0 * M \mu d\mu \tag{2.2}$$

where $I_\nu = I_\nu^0 * M$ is the surface intensity at $\mu = \cos\theta$, M is a macroturbulence function and $*$ indicates a convolution. We can see that only some part of I_ν^0 or M which is constant over the stellar surface can be factored out of this integral. This does not occur for an atmosphere in radial motion, except for the case of isotropic macroturbulence. Gray (1992) (see Ch. 18) shows how the flux can usually only be written as a convolution if either the broadening function, or the normalised intensity profiles (before broadening), are independent of position on the stellar disk.

Sasselov & Lester (1990) took the approach of applying the sum of pulsational and rotational Doppler shifts to the intensity at different points on the stellar disk before integrating. This is the correct way to include rotational broadening. The question of Cepheid rotation was addressed by Kraft (1966) who gave statistical and evolutionary arguments against rotation. Benz & Mayer (1982) concluded that rotation has a negligible effect on the observed line broadening in Cepheids while Kovacs & Buchler (1990) calculated a firm upper limit of 10 km s^{-1}, which corresponds to an equivalent turbulent velocity of 7 km s^{-1}. We do not consider rotational broadening here.

We have included macroturbulent effects by using the radial-tangential function, equation 18.7 in Gray (1992),

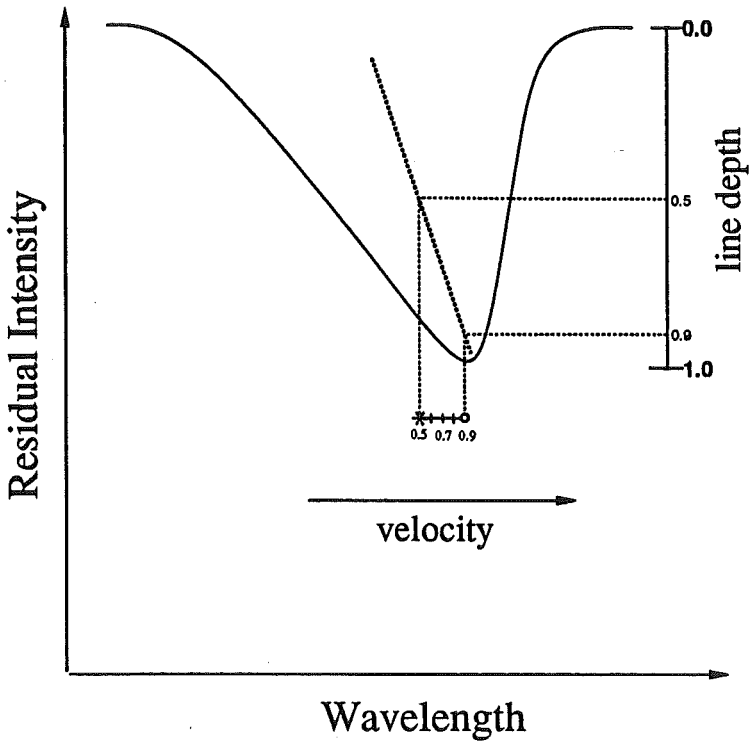

Figure 2.1: Schematic representation of a spectral line showing how we define the line bisector at various depths in the line.

$$M(\Delta\lambda) = \frac{A_R}{\pi^{\frac{1}{2}}\zeta_R cos\theta} exp\left[-\left(\frac{\Delta\lambda}{\zeta_R cos\theta}\right)^2\right] + \frac{A_T}{\pi^{\frac{1}{2}}\zeta_T sin\theta} exp\left[-\left(\frac{\Delta\lambda}{\zeta_T cos\theta}\right)^2\right], \quad (2.3)$$

where $\Delta\lambda$ is the velocity projected onto the line of sight and converted to wavelength units (i.e. M($\Delta\lambda$) is the distribution of macroturbulent Doppler shifts). Here A_R and A_T are the fractions of the stellar surface area having radial and tangential motion respectively and ζ_R and ζ_T are the dispersions of the Gaussian velocity distributions. We have followed Gray (1992) and set $A_R = A_T = 0.5$ and $\zeta_R = \zeta_T = \zeta$, the characteristic macroturbulent velocity.

This function was convolved with each of the twenty intensity profiles at equally spaced $\mu = \cos\theta$, for $\zeta = 7$ km s^{-1} and $\zeta = 10$ km s^{-1}. These intensities were Doppler shifted in turn by each of the pulsational velocities, V_P, given in Table 2.1 and the resultant intensity spectra integrated over the stellar disk to

Table 2.1: Parameters for synthetic line profile calculations.

$T_{\rm eff}$	$\log g$	ξ (km s^{-1})	ζ (km s^{-1})	V_P (km s^{-1})
4500	1.0	2.5	7	10
5000	1.5	5.0	10	20
5500	2.0			30
6000				40
				50

give net flux profiles. These were then convolved with a Gaussian of half-width 0.1 Å to allow for instrumental broadening. This value was obtained from the half-width of arc lines in the comparison spectra of Cepheids on our observational programme.

For comparison with different macroturbulence models, we have also calculated line profiles for radial macroturbulence, $A_T = 0$ in (2.3), and for isotropic macroturbulence.

Fig. 2.1 shows a schematic line profile demonstrating our method for determining velocities using line bisectors. We designate the continuum as being at depth 0 and the core at depth 1. Our radial velocity measurements are the Doppler shift of the bisector between line depths 0.5 (which we indicate with an asterisk) and 0.9 (indicated by an open circle). In this way each radial velocity 'point' becomes a 'vector' (that is a line which indicates the magnitude and direction of asymmetry). Such radial velocities were calculated for the 660 synthetic line profiles calculated for each of the three macroturbulence models, along with their half-widths and equivalent widths. The equivalent widths for all the lines were in the range 65 - 420 mÅ, thereby including lines from different parts of the curve of growth.

2.2 Projection factors

The projection factor, P, to convert the measured radial velocity to the actual pulsational velocity of the star, varies depending on what depth in the line profile the radial velocity is measured. In Figs 2.2 and 2.3 we show the projection factors determined at depths 0.5 and 0.9 for each of the line profiles, $P(0.5)$ and $P(0.9)$,

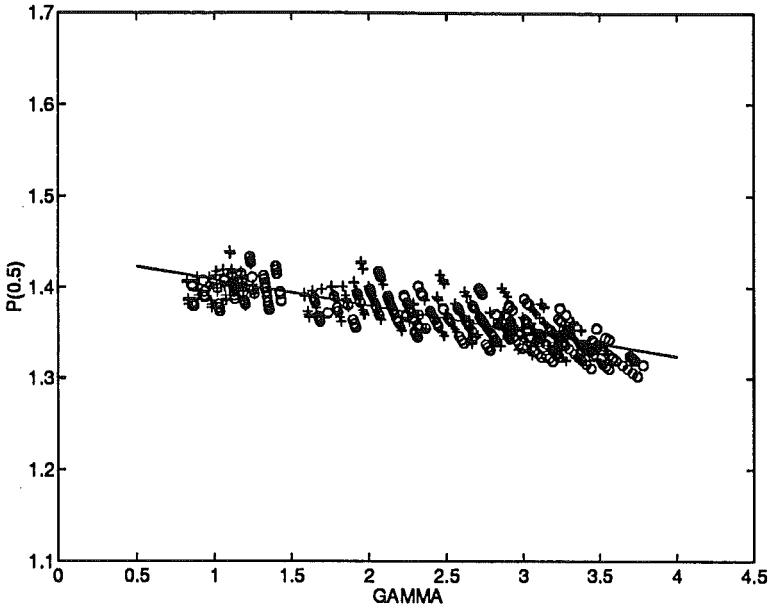

Figure 2.2: Projection factor plotted against γ, the ratio of pulsational velocity to half-width of line for radial-tangential macroturbulence and line depth 0.5. (o) $\zeta = 7$ km s^{-1}; (+) $\zeta = 10$ km s^{-1}; solid line $P(0.5) = 1.436$ - 0.028γ

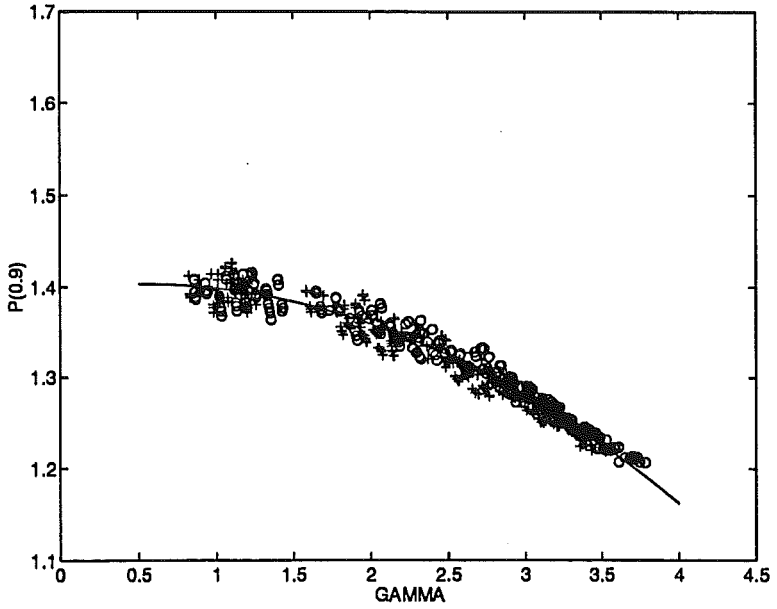

Figure 2.3: As for Fig. 2.2 for line depth 0.9. Solid line $P(0.9) = 1.398 + 0.021\gamma$ - $0.020\gamma^2$.

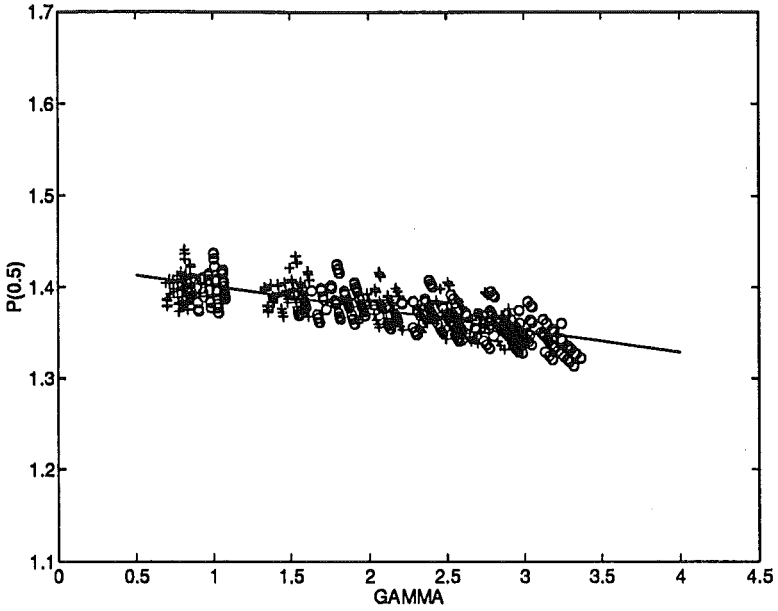

Figure 2.4: Projection factor for isotropic macroturbulence and line depth 0.5. Symbols as in Fig. 2.2. Solid line $P(0.5) = 1.425 - 0.024\gamma$

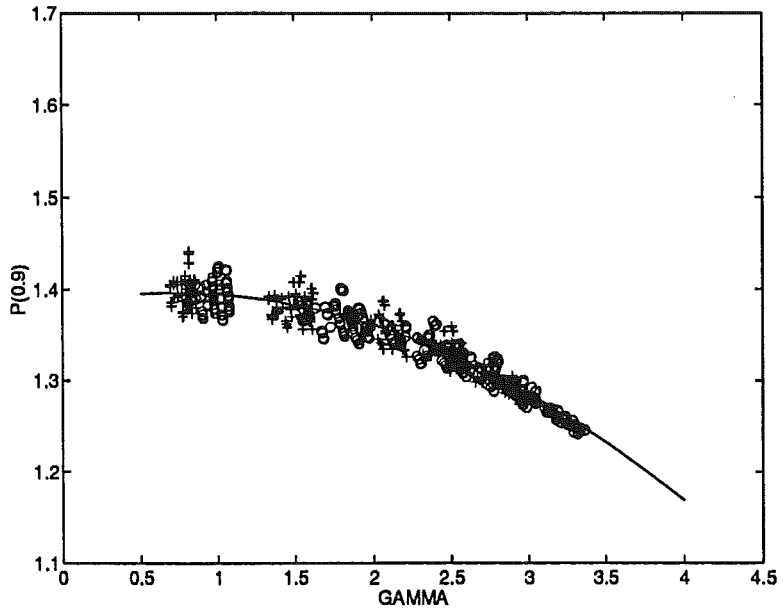

Figure 2.5: As for Fig. 2.4 for line depth 0.9. Solid line $P(0.9) = 1.385 + 0.030\gamma - 0.021\gamma^2$.

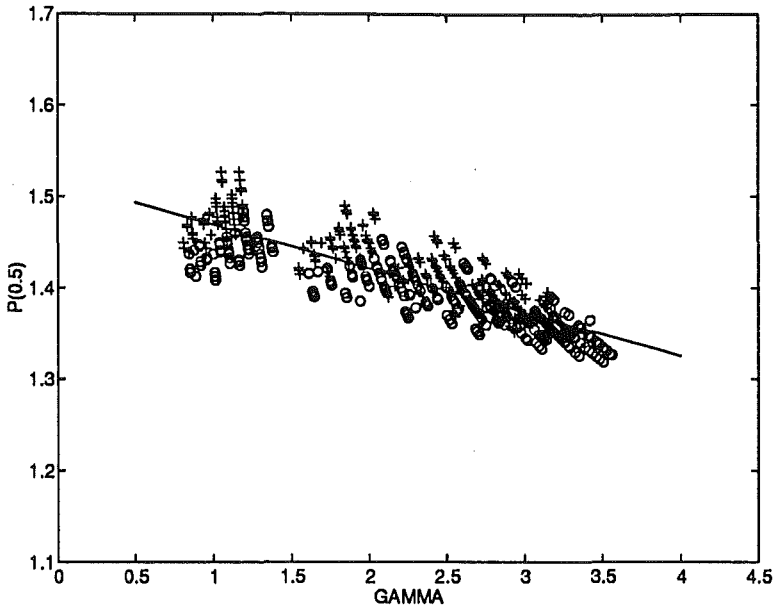

Figure 2.6: Projection factor for radial macroturbulence and line depth 0.5. Symbols as in Fig. 2.2. Solid line $P(0.5) = 1.517 - 0.048\gamma$

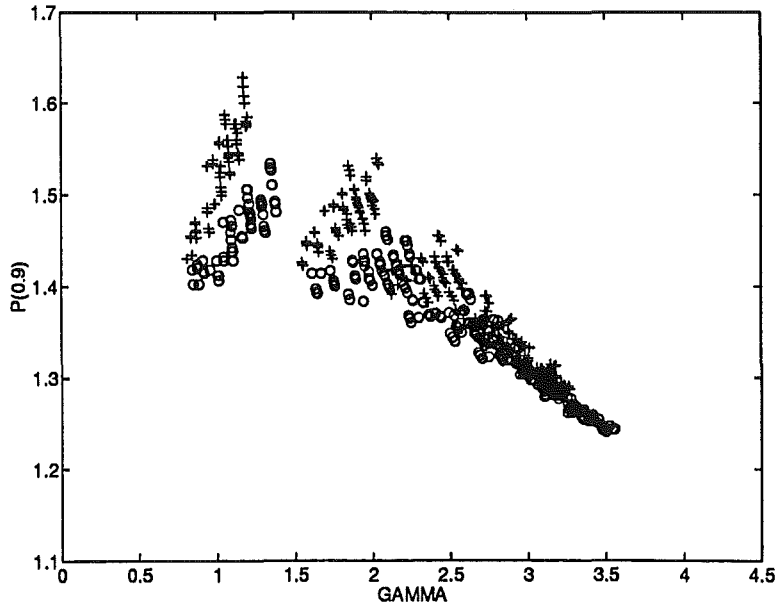

Figure 2.7: As for Fig. 2.6 for line depth 0.9.

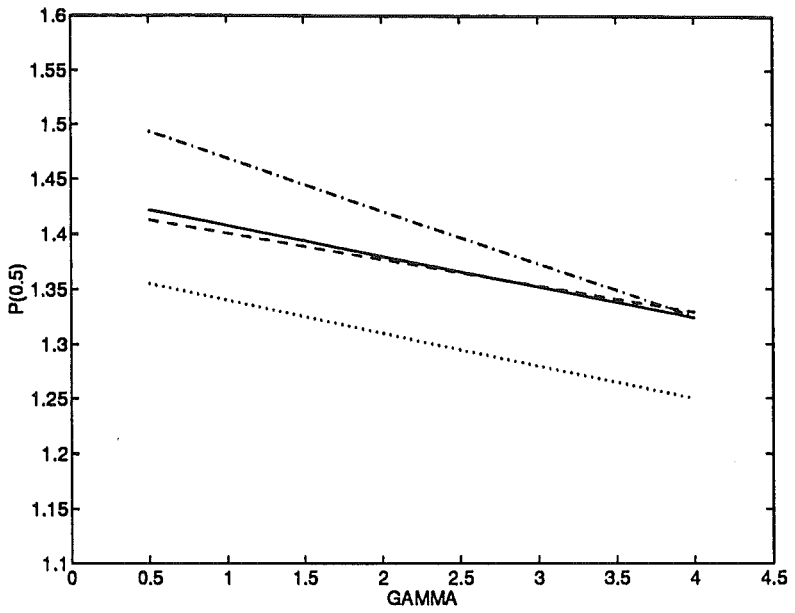

Figure 2.8: Summary of projection factors for different models of macroturbulence for line depth 0.5. ——— radial-tangential, - - - - isotropic, - · - · - radial, ····· Parsons' (1972) relationship P = 1.37 - 0.03 γ.

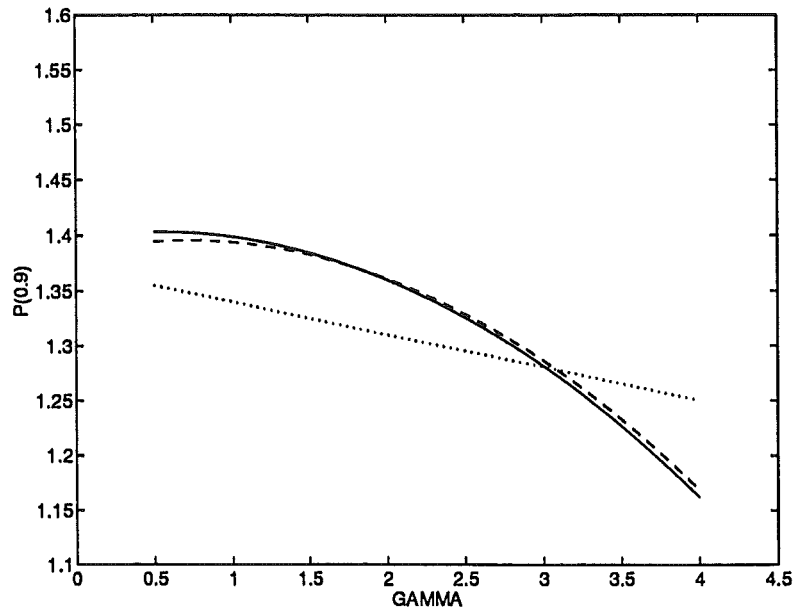

Figure 2.9: As for Fig. 2.8 for line depth 0.9.

for radial-tangential macroturbulence. These are plotted against γ, the ratio of pulsational velocity, V_P, to the half-width at half-height of the line. Parsons (1972) found this to be the main parameter to which P is sensitive. These synthetic factors were least-squares fitted with linear and quadratic functions for P(0.5) and P(0.9) respectively, resulting in the relations

$$P(0.5) = 1.436 - 0.028\gamma \quad (2.4)$$

$$P(0.9) = 1.398 + 0.021\gamma - 0.020\gamma^2, \quad (2.5)$$

which are shown as solid lines in Figs 2.2 and 2.3. These relationships have rms residuals of 0.015 and 0.011 for $P(0.5)$ and $P(0.9)$ respectively. The projection factors derived for isotropic macroturbulence and radial macroturbulence are shown in Figs 2.4–2.7. Fits to those for isotropic macroturbulence give the relations

$$P(0.5) = 1.425 - 0.024\gamma \quad (2.6)$$

$$P(0.9) = 1.385 + 0.030\gamma - 0.021\gamma^2, \quad (2.7)$$

and for radial macroturbulence

$$P(0.5) = 1.517 - 0.048\gamma. \quad (2.8)$$

A fit to P(0.9) for radial macroturbulence was not considered useful. The reason for the large scatter in P(0.9) will be discussed in Section 2.3.

A summary of these derived projection factors is shown in Figs 2.8 and 2.9. The results for radial-tangential broadening are very similar to those obtained for isotropic macroturbulence, while those for radial macroturbulence are somewhat larger. Our results for isotropic macroturbulence are around 10 per cent larger than those obtained by Parsons (1972). This discrepancy may be due to the model atmospheres used by Parsons having a limb darkening different to that of the Kurucz models. Parsons' models also had a relatively large microturbulence which increased with height.

Our Cepheid spectra, discussed in Chapter 3, show lines with γ values mostly in the range $\gamma \leq 2$, so if a constant value for P is required, we recommend using

$$P(0.5) = 1.41 \pm 0.04 \quad (2.9)$$

$$P(0.9) = 1.38 \pm 0.03. \quad (2.10)$$

These are the mean values over the interval $0 < \gamma < 2$ for radial-tangential macroturbulence, with uncertainties due to the gradients of the fitted lines plus the rms

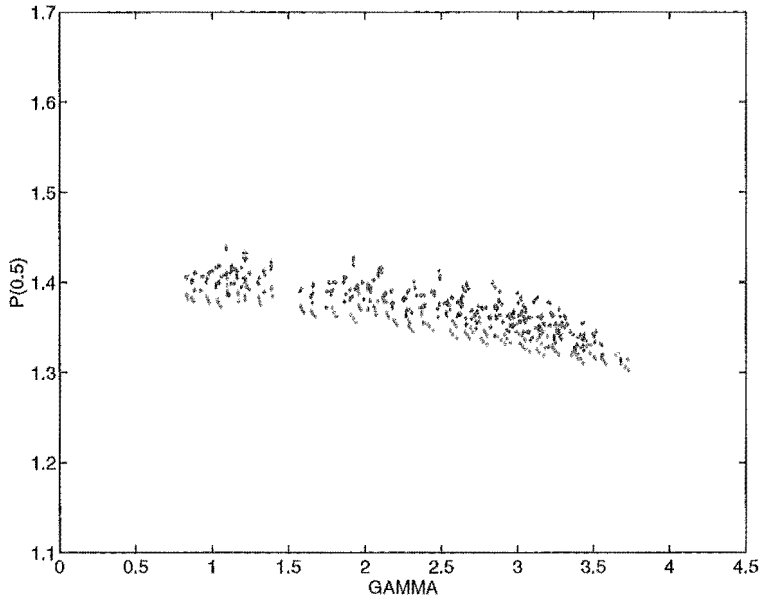

Figure 2.10: Variation of projection factor with $T_{\rm eff}$ for line depth 0.5 and radial-tangential macroturbulence. $T_{\rm eff}$ = 4500; green, 5000; yellow, 5500; blue, 6000; red.

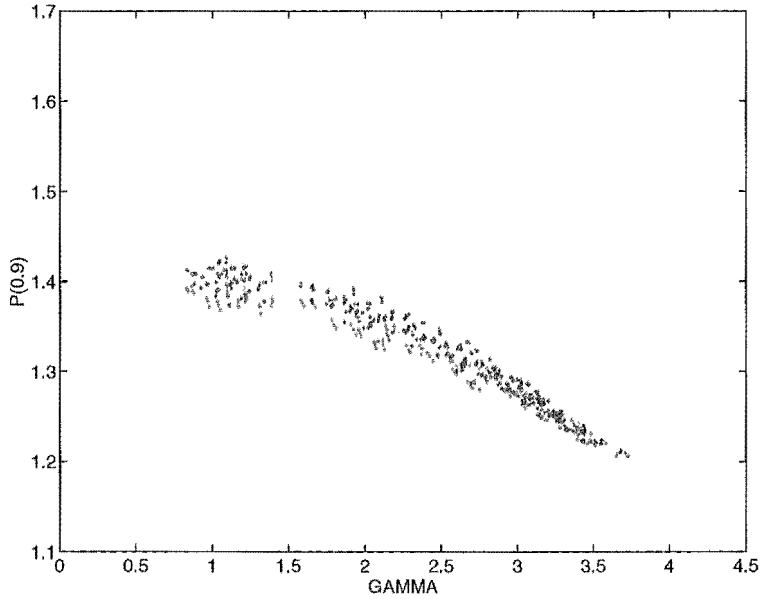

Figure 2.11: As for Fig. 2.10 for line depth 0.9.

residuals. P changes by around 4 per cent over the interval $0 < \gamma < 2$ for depth 0.5 and by around 5 per cent for depth 0.9, indicating that the practice of using a constant projection factor in Baade-Wesselink calculations may be introducing errors of this magnitude. These projection factors are $\sim$ 2 - 8 per cent larger than those in common usage (1.31 – 1.35), indicating a systematic underestimate of Cepheid radii and distances from optical radial velocity measurements. Use of these new values may go some way towards resolving the systematically larger radii and distances reported by Sasselov & Lester (1990) from infrared measurements.

Karp (1975b) found that the projection factor measured at a depth of 0.5 varied more slowly as a function of γ than that measured at depth 0.9. He thus recommended that measurements be taken from a depth of 0.5 in the line profile. This trend is also shown in our data but only for $\gamma > 2$, larger than the values we observe. In stellar spectra there tends to be a problem with line blending when measurements are made higher in the line profile. Our recommendation is that the radial velocity be measured deeper in the line profile (0.9 for example) and that a variable projection factor be used if necessary.

Hindsley & Bell (1986) noticed a trend towards greater projection factors with higher temperature. Their trend is only partially confirmed by our data (see Figs 2.10–2.13). The projection factor increases up to $T_{\rm eff}$ = 5500 K, but decreases slightly again for $T_{\rm eff}$ = 6000 K. This is the same for depths 0.5 and 0.9, although the scatter within each curve of a given temperature is at least comparable to the differences between curves.

2.3 Asymmetries

In order to study the velocity fields in Cepheid atmospheres, the asymmetry of our synthetic spectral lines will be compared with observed Cepheid spectra. For our purposes we make a definition that the asymmetry of a spectral line, A, is the difference between the radial velocity of the bisector at depth 0.9 and at depth 0.5.

In Fig. 2.14 we show the asymmetry on a logarithmic scale, plotted against γ, for radial-tangential broadening. Apart from the considerable scatter at very low asymmetries ($A < 0.1$ km s^{-1}), the relationship is remarkably linear. A linear

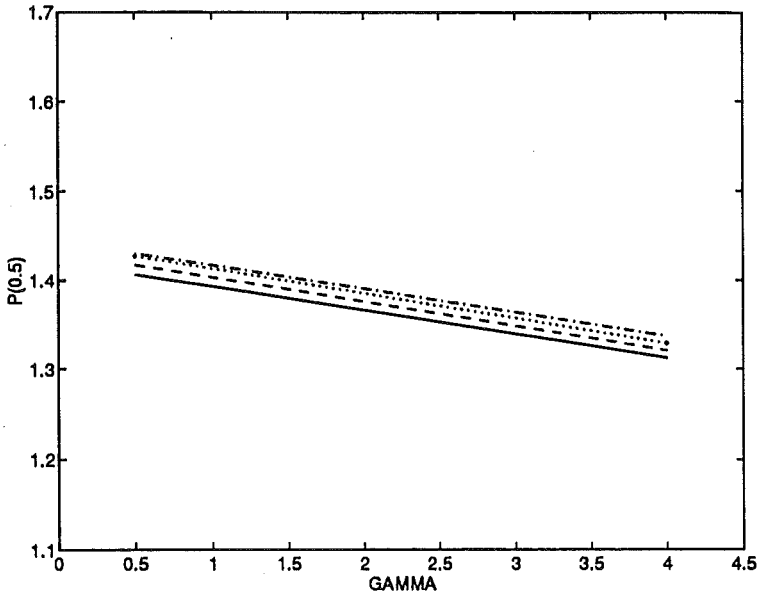

Figure 2.12: Least squares fits to projection factors from Fig. 2.10. ——— $T_{\text{eff}} = 4500$, - - - - 5000, - · - · - 5500, ····· 6000.

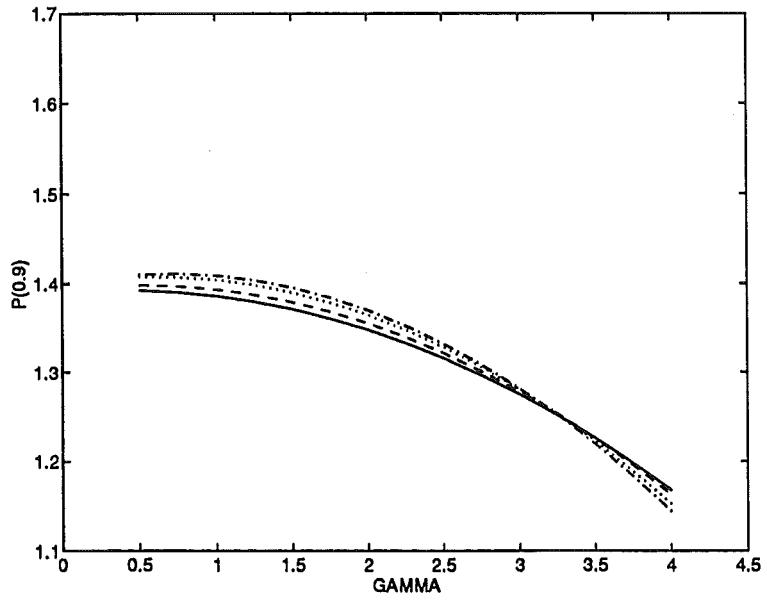

Figure 2.13: As for Fig. 2.12 for line depth 0.9.

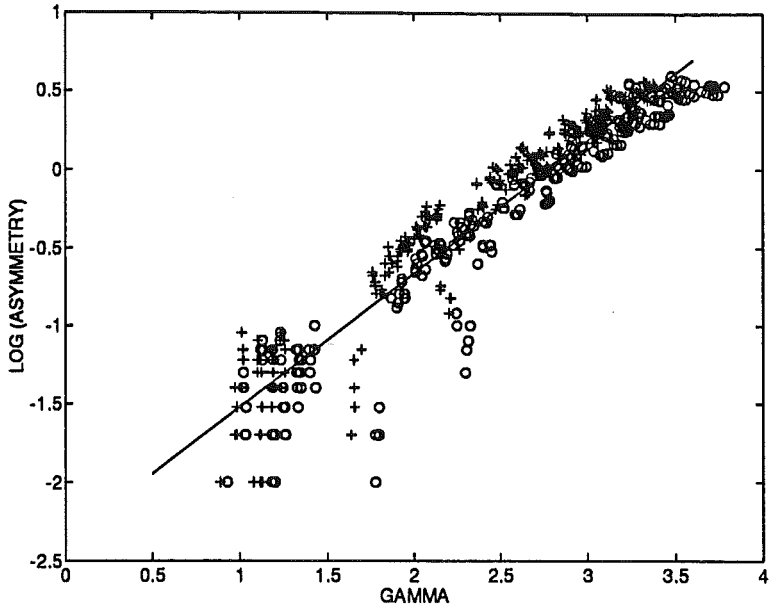

Figure 2.14: A versus γ on a logarithmic scale for radial-tangential macroturbulence . Symbols as in Fig. 2.2.

least squares fit provides the exponential relationship

$$A = (4.211 \times 10^{-3})\ 10^{0.8552\,\gamma} \tag{2.11}$$

between line asymmetry and γ. This equation provides a representation of the asymmetry for $\gamma < 4$ as shown in Fig. 2.15.

This relationship is not particularly sensitive to the model used for macroturbulent broadening. In Figs 2.16 and 2.17 we plot the asymmetry of each of the profiles calculated using isotropic macroturbulence and radial macroturbulence. Also shown is the relationship (2.11), derived for the radial-tangential model, which also provides a reasonable representation of these data.

An interesting effect occurs at low pulsational velocities when radial macroturbulence is present. Intensity profiles from the centre of the stellar disk are broadened sufficiently that the major contribution to the core of the integrated flux profile comes from a part of the stellar disc nearer the limb than is usual. This results in a line profile which is asymmetric in the direction opposite to that of the projection effect. Such negative asymmetries can be seen at low γ values in Fig. 2.17. The effect is primarily a shifting of the core of the line profile and the wings are relatively unaffected. The effect is greater in weaker lines and is

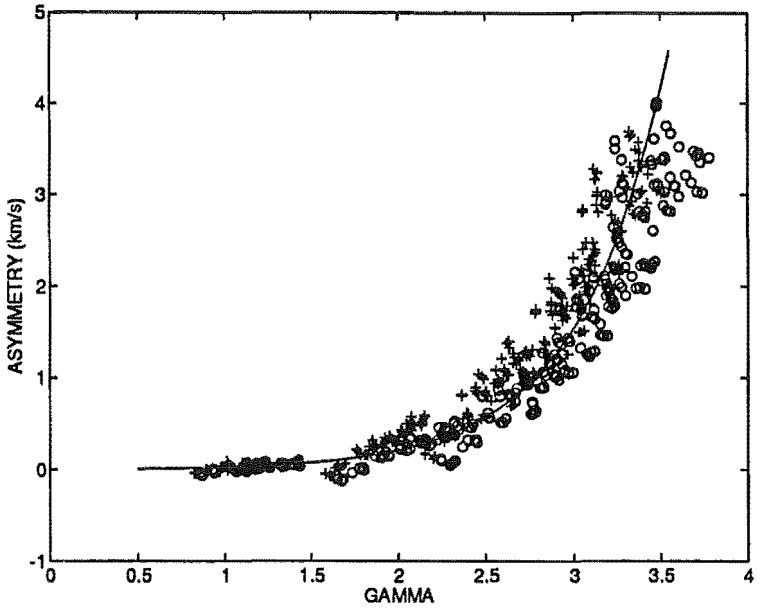

Figure 2.15: A versus γ (symbols as in Fig. 2.2) plotted with the curve (2.11).

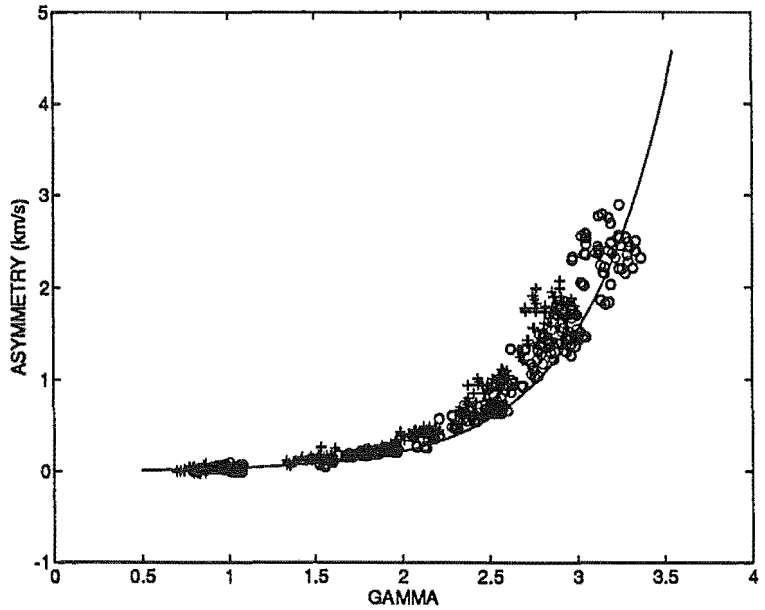

Figure 2.16: A versus γ for isotropic macroturbulence with the curve (2.11) derived from the radial-tangential model. Symbols as in Fig. 2.2.

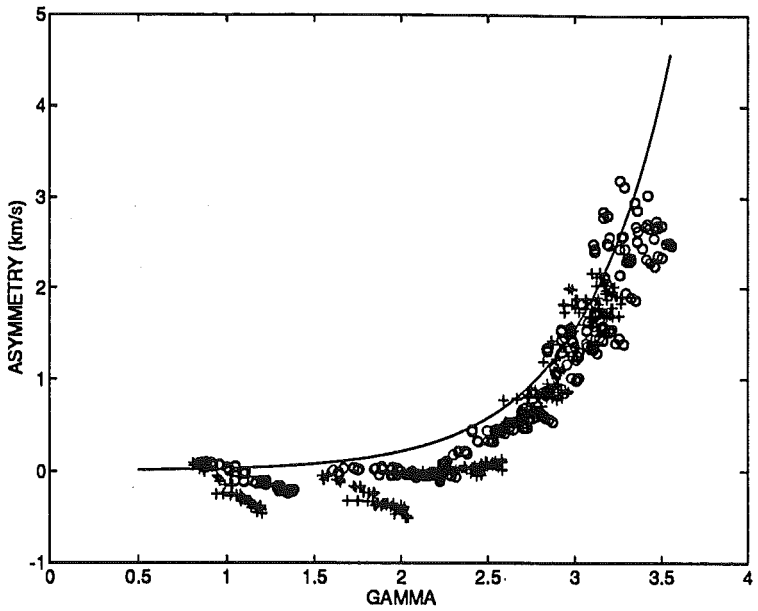

Figure 2.17: As for Fig. 2.16 for radial macroturbulence.

responsible for the large projection factors and large scatter at low γ values in Fig. 2.7. At higher pulsational velocities the line profile shapes are dominated by geometric projection.

That a relationship exists between A and γ is a consequence of any relationship between the projection factors and γ. This can be shown by writing the asymmetry in the form

$$A = V_P \frac{P(0.5) - P(0.9)}{P(0.5)P(0.9)}. \tag{2.12}$$

The existence of the relationship given by (2.11) is very important because we now have a mechanism which enables us to separate the asymmetry of a spectral line due to geometric projection of a radial pulsation from any other asymmetry present. We will return to this point in subsequent chapters.

Chapter 3

Observations of Cepheids

3.1 Observational programme

In 1987 an observational programme was set up at Mt John University Observatory (MJUO) to observe a group of seven southern Cepheids using the observatory's échelle spectrograph and Reticon linear diode array detector (LDA). The program was instigated initially by Drs George Wallerstein and Peter Cottrell during an Erskine Fellowship visit by the former to the University of Canterbury. Spectra obtained were mainly centered on Hα (6562.8 Å) and each spectrum spanned $\sim$ 70 Å. After the withdrawal for repairs of the LDA detector in mid-1991, further observations were made using the MJUO CCD detector. This detector gave coverage of around 30 Å of each of four échelle orders.

The Cepheids observed and their zero epochs and periods used for phasing are listed in Table 3.1. A number of additional Cepheids were added to this programme but they are not included here because they are still being observed to obtain full phase coverage. Observations for this programme were made by the author, Mike Clark, Karen Pollard, Drs Peter Cottrell Warrick Lawson and George Wallerstein.

3.2 Equipment configuration, observation and reduction techniques

3.2.1 Telescopes and spectrograph

Some initial spectra were taken using the 60 cm Boller and Chivens telescope at MJUO. All subsequent observations were taken using the 1 m telescope in its

Table 3.1: Summary of observations

Star	Period (days)	Zero epoch	Number of observations
W Sgr	7.594904	2443374.622	23
β Dor	9.842425	2440905.269	36
S Nor	9.754244	2444018.884	26
S Mus	9.659875	2440299.163	50
κ Pav	9.094230	2440140.167	30
Y Oph	17.126907	2439853.173	18
U Car	38.768002	2437320.055	25

f/13.5 configuration. The échelle spectrograph (Hearnshaw 1978) gave a resolving power of $\lambda/\Delta\lambda \sim 30000$ and a dispersion of 2 Å mm^{-1} at Hα.

3.2.2 LDA

The observing procedure used was to take a comparison spectrum using a Th-Ar lamp and a smooth-field using a tungsten lamp immediately after each stellar spectrum.

The spectra were smooth-field divided, deglitched (cosmic ray spikes removed) and Fourier-smoothed at the observatory site using software written by MacQueen (1986) for the GIMIX computer which controls the Reticon array. Files containing the divided and smoothed stellar spectra and divided comparison spectra were brought back to Christchurch on 5.25" floppy disks where they were transferred to the University's VAX/VMS or UNIX computers.

Remaining steps in the reduction procedure were made with the FIGARO software package. Arc lines in the comparison spectra were identified and third order polynomial wavelength fits generated to calibrate the stellar spectra. A continuum for each spectrum was generated by interactively marking points and was divided into the stellar spectrum. Finally, a heliocentric correction was applied.

3.2.3 CCD

Thorium-argon comparison lamp and tungsten lamp-smooth field images were taken immediately after each stellar spectral image. The image acquisition software is described in Tobin (1991). No processing was done at the observatory site and all images were brought back to the University on 1200' nine track magnetic tape. These images were read into the University's VAX/VMS computers and written to disk as 2880 byte per record FITS files using a program written by Tobin (1993).

The spectra were reduced using the Caltech FIGARO 2.4 software package on the UNIX computer systems at the University of Canterbury. A set of four UNIX shell files were written and used to perform the image reduction described below and listed in Appendix A. The images were initially cosmic ray subtracted and smooth-field divided. The four spectral orders on the object image were tracked and straightened and the same straightening applied to the arc images. The rows of the object image were added together for each spectrum after having been chosen interactively by examining the profile of a cut perpendicular to the direction of the orders. The image was then collapsed into four spectra. As the objects were reasonably bright and the spectra of reasonably high ($\gtrsim 50$) signal to noise, no subtraction of the scattered light background was made because Pollard (1991, private communication) determined that this had the net effect of adding noise. The level of scattered light in the échelle orders around Hα was found to be very small. The same rows were collapsed on the arc image to form the comparison spectra. Arc lines in the comparison spectra were identified and a third order polynomial dispersion solution calculated for each order and written to the object spectrum. The raw spectra were then Fourier-smoothed, continuum divided and a heliocentric correction applied.

3.3 Analysis of spectra

In the remainder of this chapter the results are shown of an analysis of the spectra obtained from our observational programme. For each star we first display the spectra obtained at Hα, stacked in phase order. These are best viewed from a shallow angle in order to see the radial velocity and line profile variation. Line bisector radial velocity curves are produced for Hα and a moderate-strength metallic line using the method described in Chapter 2 for synthetic lines. We have

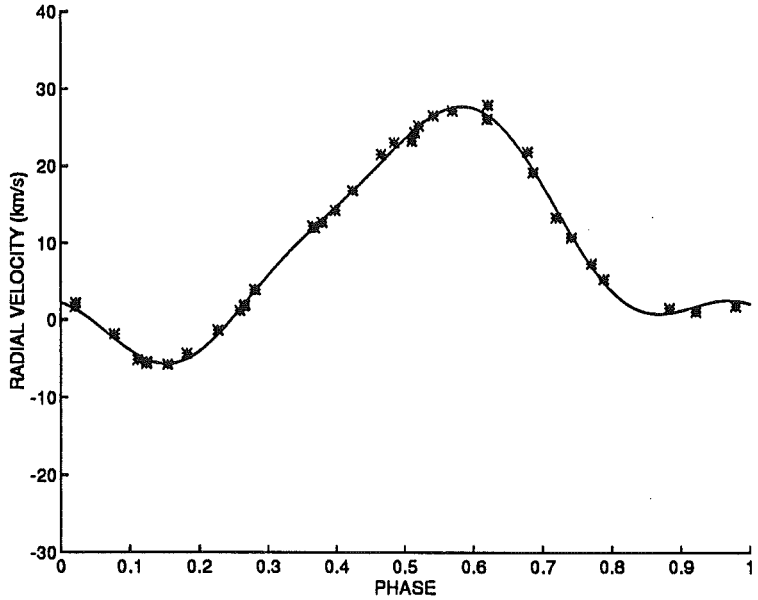

Figure 3.1: β Dor: Fourier series fit to radial velocities of 6546 Å Fe I line measured at line depth 0.9.

chosen the Fe I line at 6546 Å because of a number of factors. It is of sufficient strength at all phases to be observed in all of the programme stars. It is also free from photospheric or telluric blending. Its excitation potential, $\chi = 2.76$ eV, is representative of stars with the effective temperatures of Cepheids. (Details of the radial velocities, equivalent widths, half-widths and asymmetries measured from this line are tabulated in Appendix B. Tests have also shown that other weak to moderate strength metallic lines give similar results.) For this line we also plot asymmetry against γ, the ratio of pulsation velocity to line half-width at half-height, along with the synthetic relation (2.11) for geometric projection and limb darkening. For each star we have also calculated acceleration and change in radius (ΔR) curves by respectively differentiating and integrating Fourier series fits to the radial velocity curves which have been multiplied by the appropriate projection factor. We display the mean of these curves for line depths 0.5 and 0.9 for each star.

3.4 γ-velocities

To determine the pulsation velocity for each star we must first find its γ-velocity (systemic velocity). This was determined by finding the zero order term,

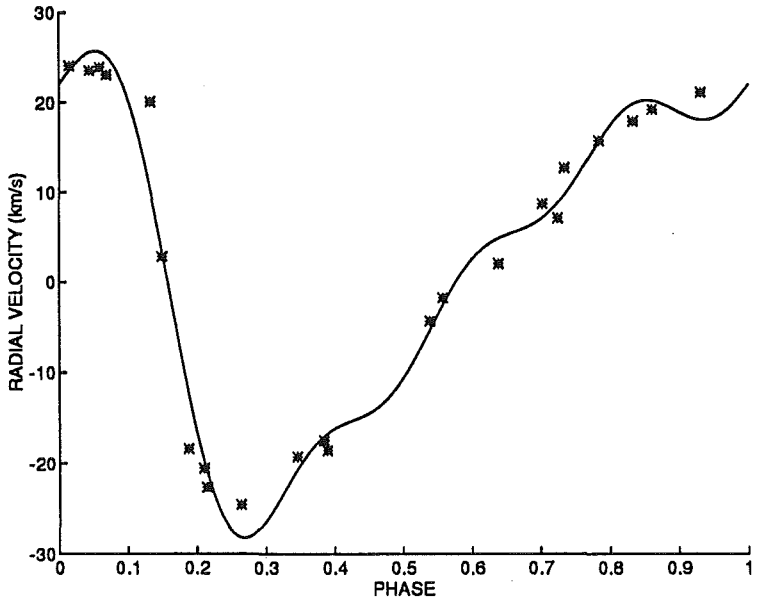

Figure 3.2: U Car: as for Fig. 3.1.

Table 3.2: γ velocities from the 6546 Å Fe I line at line depths 0.5 and 0.9 for the programme stars, $\gamma(0.5)$ and $\gamma(0.9)$, with their standard deviations, $\sigma_\gamma(0.5)$ and $\sigma_\gamma(0.9)$ and the standard deviations of the radial velocities from the fitted curves, $\sigma(0.5)$ and $\sigma(0.9)$, all in km s^{-1}. Also given is the order of the fit, M, where K = 2M + 1.

star	$\gamma(0.5)$	$\sigma_\gamma(0.5)$	$\sigma(0.5)$	$\gamma(0.9)$	$\sigma_\gamma(0.9)$	$\sigma(0.9)$	M
W Sgr	-28.08	0.18	0.68	-27.75	0.19	0.85	5
β Dor	8.61	0.12	0.68	8.89	0.12	0.70	4
S Nor	5.30	0.17	0.80	5.70	0.18	0.86	5
S Mus	-0.51	0.15	0.96	-0.09	0.14	0.91	5
κ Pav	37.65	0.23	1.19	37.95	0.20	1.04	5
Y Oph	-8.81	0.39	0.80	-8.21	0.43	0.87	3
U Car	1.89	0.88	3.84	1.87	0.89	3.87	4

A_1, of a Fourier series fitted to its radial velocity curve,

$$v'(t) = \sum_{k=1}^{K} A_k a_k(t), \tag{3.1}$$

where t is the phase and

$$a_k(t) = \begin{cases} \sin(2\pi\frac{k}{2}t), & \text{k even} \\ \cos(2\pi\frac{k-1}{2}t), & \text{k odd.} \end{cases} \tag{3.2}$$

The number of terms needed for each fit, K, was increased until a good fit was judged by eye to have been made. A typical fit and the worst fit are shown in Figs 3.1 and 3.2. The variance for the fit is calculated

$$\sigma^2 = \frac{1}{N-K}\sum_{i=1}^{N}(v_i - v_i')^2, \tag{3.3}$$

(Kovacs, Kisvarsanyi & Buchler 1990) where N is the number of observations, v_i are the observed radial velocities and v_i' are the fitted radial velocities. The variance for the γ-velocity,

$$\sigma_\gamma^2 = \alpha_{11}^{-1} \tag{3.4}$$

(Bevington 1969), where

$$\alpha_{jk} = \frac{1}{\sigma^2}\sum_{i=1}^{N} a_j(t_i)a_k(t_i). \tag{3.5}$$

γ velocities for each star were calculated using the radial velocity data from heights of 0.5 and 0.9 in the line profile and are given in Table 3.2 along with their standard deviations and the standard deviations of the fitted curves. The different γ-velocities found for the different heights are real and will be discussed in Section 3.13.

The pulsation velocity for each star was calculated by subtracting its γ-velocity (for the appropriate height) from the radial velocity measurements at heights 0.5 and 0.9 and multiplying by the projection factor appropriate for each height, (2.9) or (2.10). To determine these projection factors, it is strictly necessary to know the pulsation velocity. However, the dependence of the projection factors on γ is sufficiently weak that using the constant values, $P(0.5) = 1.41$ and $P(0.9) = 1.38$, to determine γ from the radial velocities introduces negligible errors. The pulsation velocities derived from the two heights were averaged to give the net pulsation velocity.

3.5 W Sgr

W Sgr has a 7.6 day period, a mean radius, R = 63.28 $R_\odot$ (Gieren, Barnes & Moffett 1989), and a Wesselink mass, M = 6.7 $M_\odot$ (Gieren 1989). It is possibly in an association with another bright Cepheid, X Sgr (Opolski 1988). It has long been thought to be a binary system (Jacobsen 1974) and an orbital solution with a period of 1780 days has recently been found by Babel et al. (1989) using CORAVEL radial velocities. We have not subtracted orbital velocities from our radial velocity data because our preliminary analysis suggests that this orbital solution may be incorrect. Evans (1991) has deduced that IUE spectra show the presence of an A0V companion and calculated absolute magnitudes, M_V = -3.98 for the Cepheid and M_V = 1.29 for the companion.

W Sgr has a radial velocity full-amplitude of $\sim$ 65 km s^{-1} for Hα and $\sim$ 40 km s^{-1} for the weak metallic lines. The Hα curve at line depth 0.9 (Fig. 3.4 open circles) lags the metallic line curve (Fig. 3.5) by $\sim$ 0.1 cycle, while the Hα curve from line depth 0.5 is almost in phase with the metals. In Figs 3.3 and 3.4 we can see that the Hα profile shows a small asymmetry in the outward pulsation velocity direction for most of its cycle and a large asymmetry between phases 0.9 and 0.95. The most extreme asymmetry of 35 km s^{-1} is seen at phase 0.93 (top spectrum in Fig. 3.3) where two components can be seen. The weaker of these components is very close in wavelength to the absorption core at phase 0 (bottom spectrum in Fig. 3.3), indicating that two absorption centres may be present in the stellar atmosphere at these phases and that the radial velocity reversal does not necessarily represent the motion of a single layer of material.

The asymmetry of the weak metallic lines (Figs 3.5 and 3.6) is almost zero during phases 0.9 to 0.6. This is consistent with geometric projection of a single radial velocity (see Chapter 2). The asymmetry seen during the remaining inward velocity part of the cycle is larger than can be explained by such a model. This indicates that spatial velocity gradients are still significant in the line forming area albeit to a much smaller extent than for Hα.

The acceleration curve (Fig. 3.7) shows a maximum outward acceleration of $\sim$ 0.7 m s^{-2} near phase 0.9. This is of a similar magnitude to the gravitational acceleration at the surface of a star of this mass and radius (0.5 m s^{-2}). Added together we derive an effective surface gravity, log g = 2.1. This compares favourably with the value, log g = 2.3, derived at the same phase by Luck &

Lambert (1981) as part of an abundance analysis. The maximum inward acceleration of 0.25 m s^{-2} is sufficient to lower the effective surface gravity to log $g \sim 1.2$ near phases 0.55 and 0.72. The radius curve (Fig. 3.8) has a full amplitude of ~ 7 $R_\odot$, or 11 per cent of the assumed mean stellar radius.

3.6 β Dor

β Dor has a period of 9.84 days and a Barnes-Evans radius of 82.6 $R_\odot$ (Hindsley & Bell 1989). McAlary & Welch (1986) have found it to have a small infrared excess which is likely due to a dust shell (Deasy 1988). It has radial velocity full amplitudes of $\sim$ 60 km s^{-1} and 35 km s^{-1} respectively for its Hα (at line depth 0.9) and metallic line radial velocity curves respectively (Figs 3.10 and 3.11). There is a phase lag of $\sim$ 0.1 cycle between Hα and the metals. Like W Sgr, the Hα radial velocities measured at line depth 0.5 seem to change from maximum to minimum in phase with the metallic lines. There is evidence for cycle to cycle variation in the Hα line profiles especially between phases 0.3 and 0.5 (Figs 3.9 and 3.10). The four spectra showing large asymmetries at these phases (Fig. 3.10) all come from the same cycle. Bell & Rodgers (1967) report that Hα was symmetrical in their spectra of β Dor obtained near phase 0.35. The Hα (line depth 0.9) and metallic line radial velocity curves have γ-velocities which differ by 6.6 km s^{-1}. It appears that, throughout the cycle, the observed Hα core is produced by material from different and changing atmospheric levels relative to those producing the metallic lines.

The metallic line profiles show little asymmetry during the negative radial velocity parts of the cycle (phases 0.75 - 0.30), but have a measurable asymmetry near radial velocity maximum (phases 0.45 - 0.70) (Figs 3.11 and 3.12). Like W Sgr, this asymmetry is too large to be explained by geometric projection alone.

The maximum outward acceleration is only about half that of W Sgr (Fig. 3.13), while its radius curve (Fig. 3.14) has a full amplitude of ~ 8 $R_\odot$ or 10 per cent.

3.7 S Nor

S Nor has a pulsation period of 9.75 days and is thought to be one of the brightest of the cluster Cepheids (Mermilliod, Mayor & Burki 1987). A hot companion star (B9.5V, $M_V = 1.06$) has been found using IUE spectra by Evans (1992b), who

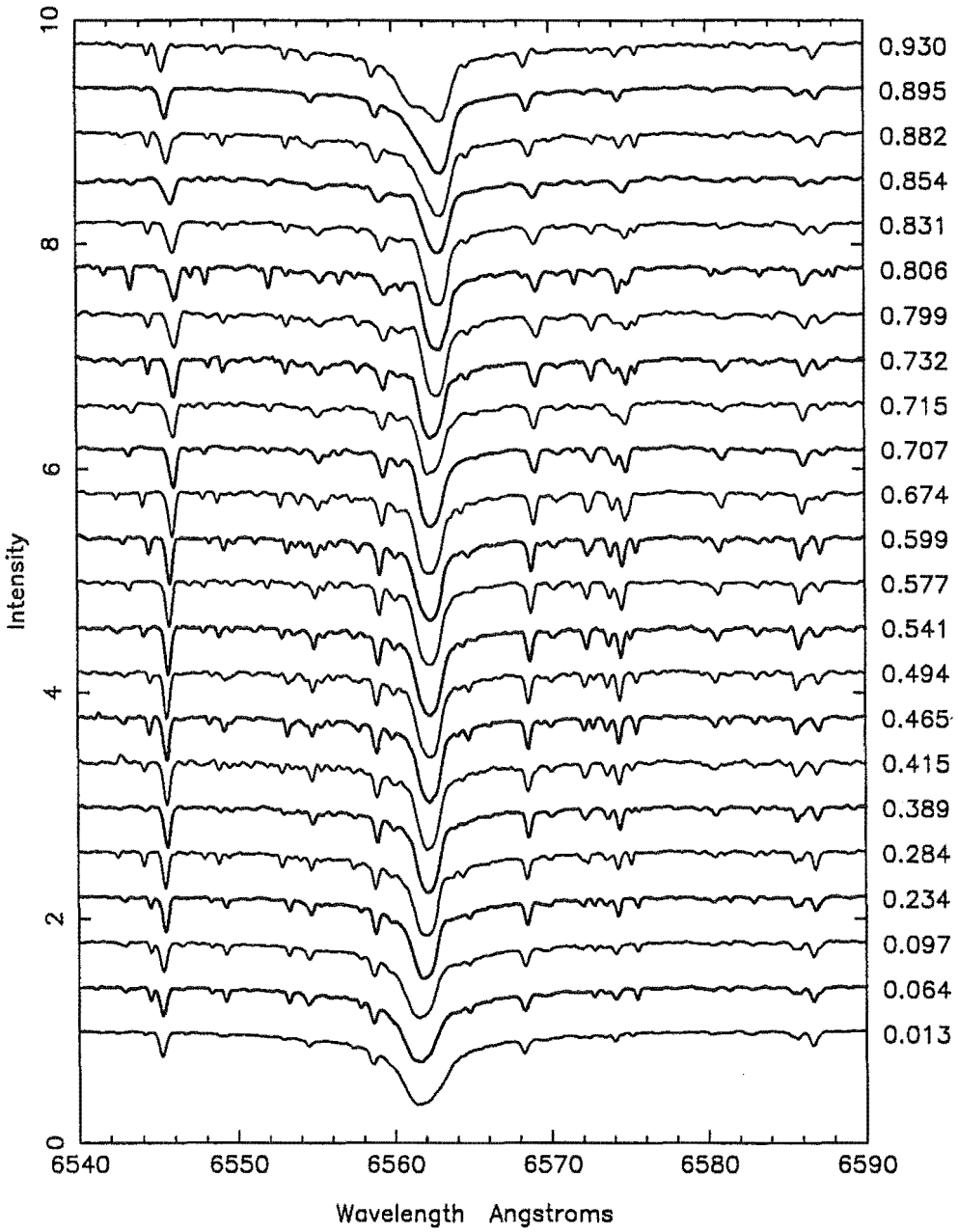

Figure 3.3: Stacked spectra of W Sgr. The pulsation phase for each spectrum is given at the right.

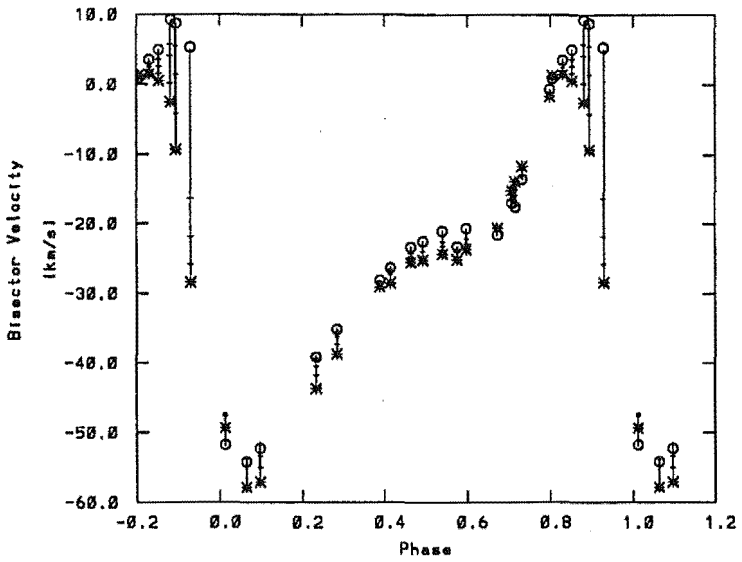

Figure 3.4: Radial velocity curve for the Hα line for W Sgr.

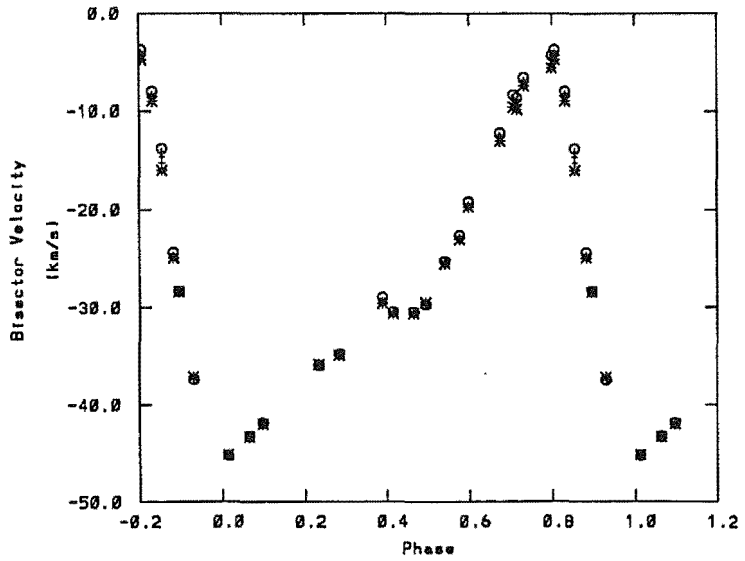

Figure 3.5: Radial velocity curve for the 6546 Å line for W Sgr.

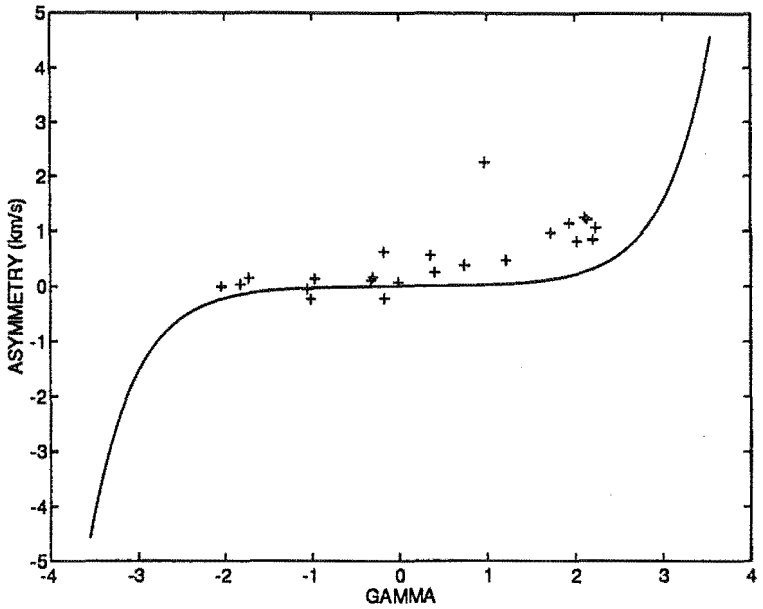

Figure 3.6: Asymmetry versus γ for W Sgr (+). Solid line $A = (9.535 \times 10^{-3}) \times 10^{0.7371\gamma}$.

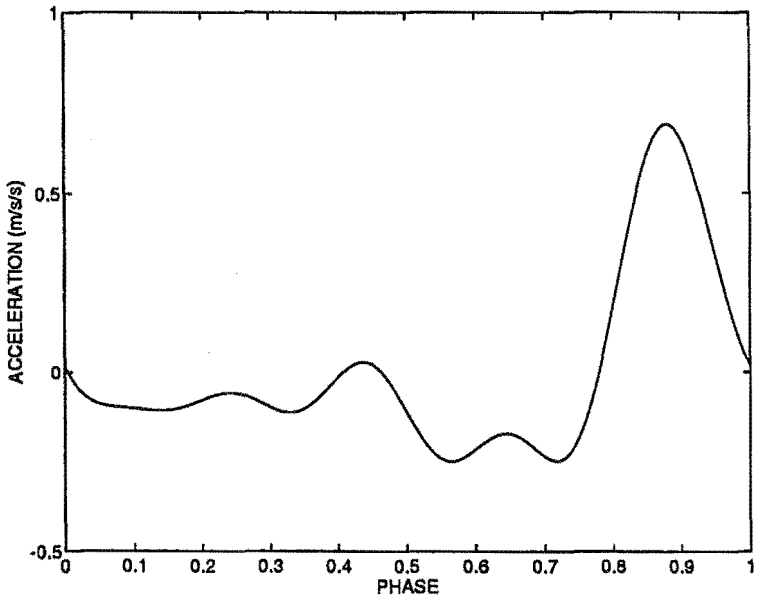

Figure 3.7: Acceleration curve for W Sgr.

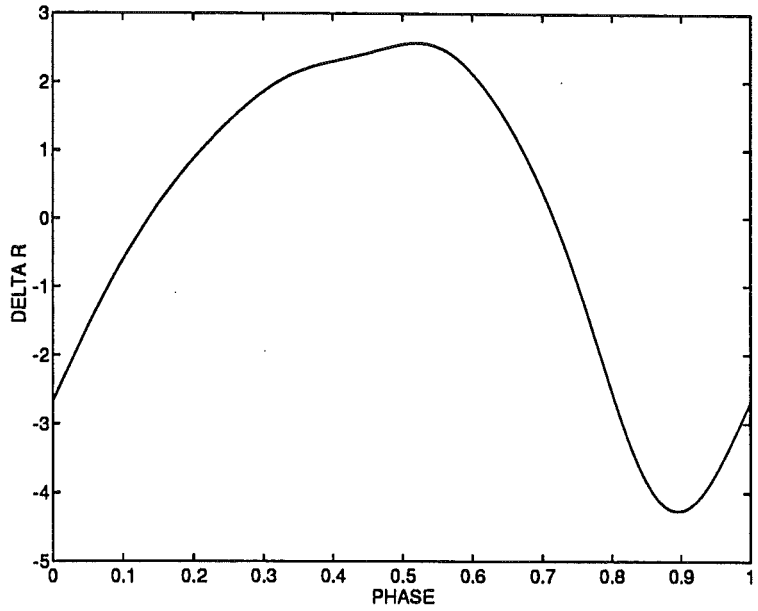

Figure 3.8: Radius curve for W Sgr in units of $R_\odot$.

also calculates an absolute magnitude for the Cepheid, M_V = -3.77. Orbital motion has not been detected. The Hα (measured at both line depths, 0.5 and 0.9) and metallic line radial velocity curves for S Nor have full amplitudes of $\sim$ 45 km s^{-1} and 35 km s^{-1} respectively and appear to be qualitatively similar to those of β Dor. The Hα curve lags that of the metals by $\sim$ 0.1 cycle and the Hα profiles are quite asymmetric during the change from inward to outward motion (phases 0.7 to 0.9 in Fig. 3.16). The metallic line curve again shows an enhanced asymmetry at phases near maximum radial velocity (Fig. 3.17), which is greater than can be explained by a simple radial motion (Fig. 3.18).

The acceleration curve (Fig. 3.19) is qualitatively similar to that of β Dor and has a maximum of $\sim$ 0.4 m s^{-2}. The radius curve is again very similar to β Dor.

3.8 S Mus

S Mus is another binary Cepheid with a pulsation period of 9.66 days and an orbital period of 506.06 days (Stappers 1993). A main sequence companion has been found by IUE and its effective temperature determined to be 17700 K (Böhm-Vitense et al. 1990). The mass of the Cepheid was determined to be in the range 4.6 $M_\odot \leqslant M \leqslant$ 6.1 $M_\odot$. An infrared excess was found for S Mus by

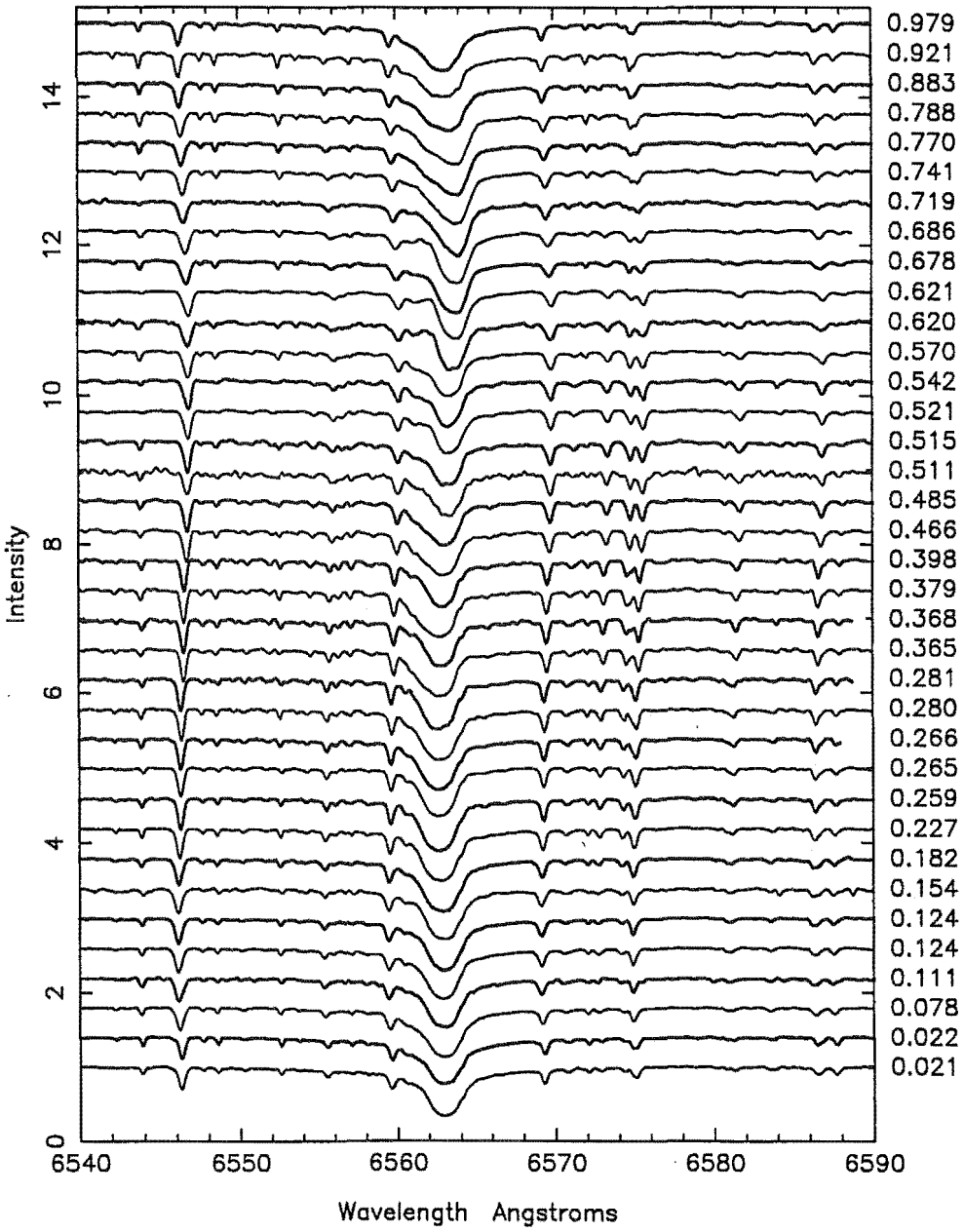

Figure 3.9: Stacked spectra of β Dor in phase order from bottom to top.

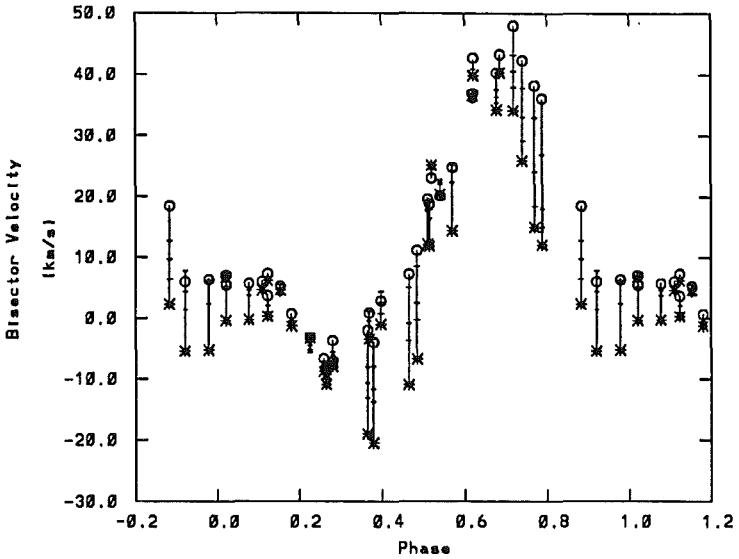

Figure 3.10: Radial velocity curve for the Hα line for β Dor.

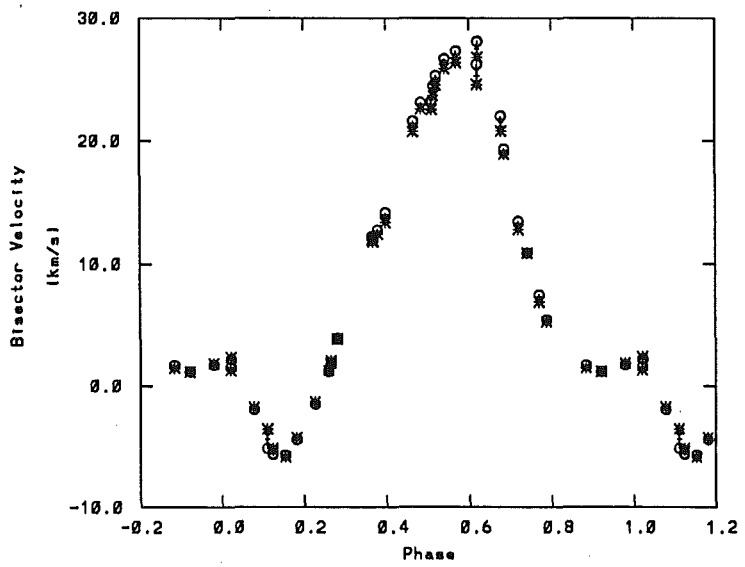

Figure 3.11: Radial velocity curve for the 6546 Å line for β Dor.

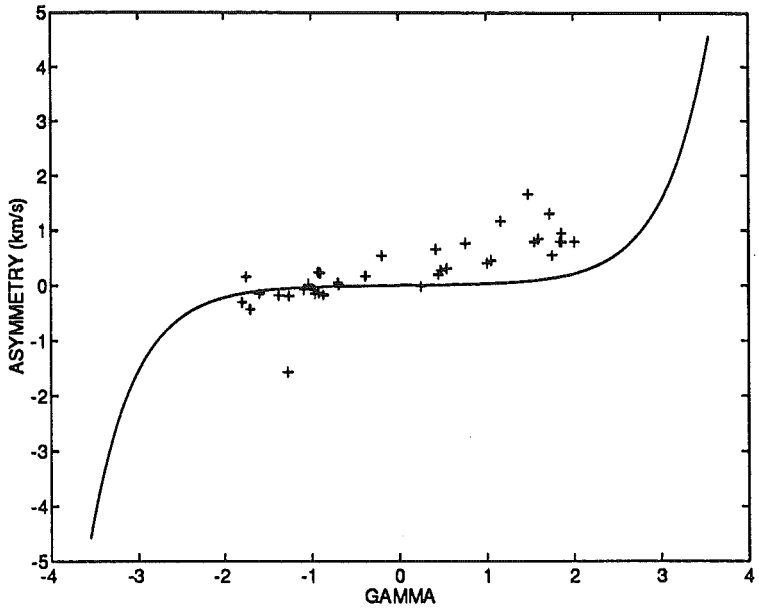

Figure 3.12: As for Fig. 3.6 for β Dor.

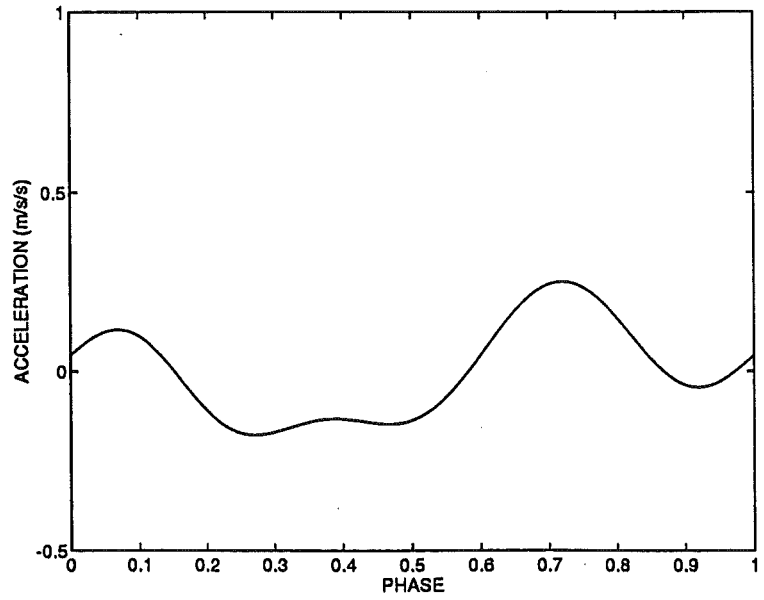

Figure 3.13: Acceleration curve for β Dor.

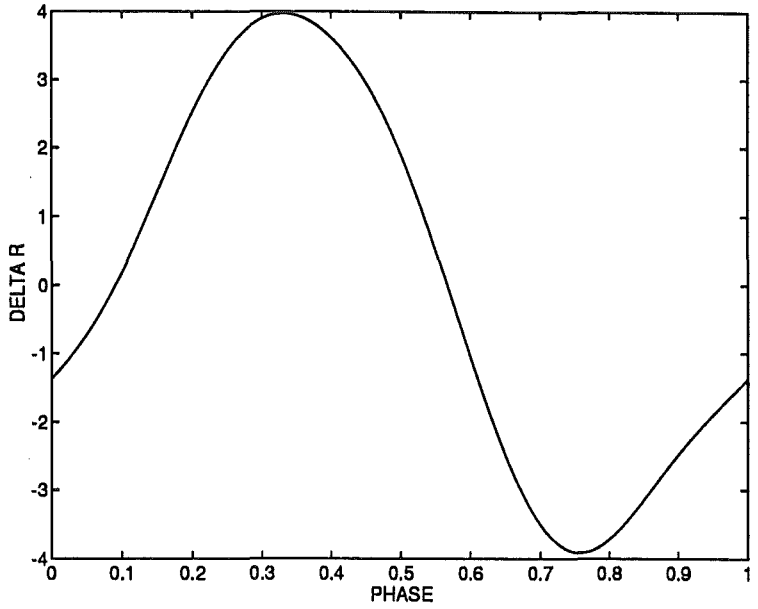

Figure 3.14: Radius curve for β Dor in units of $R_\odot$.

Deasy & Butler (1986) from IRAS point source observations and Oudmaijer et al. (1992) have found that the IRAS fluxes at 12, 25 and 60 μm can be fitted by a model of a dust shell with a characteristic temperature of 220 K.

The Hα (at line depth 0.9) radial velocity curve (Fig. 3.21) has a full amplitude of $\sim$ 45 km s^{-1} and lags the metallic line curve (Fig. 3.22, full amplitude $\sim$ 30 km s^{-1}) by $\sim$ 0.1 cycle. (The radial velocities in Figs 3.21 and 3.22 have had the orbital velocity solution of Stappers (1993) subtracted.) Significant asymmetry is present in the Hα line during the reversal from maximum positive to maximum negative radial velocity and for $\sim$ 0.2 cycle afterwards. Like the Cepheids discussed above, the metallic lines show a measurable asymmetry at positive radial velocity phases (positive γ), which is larger than that predicted for geometric projection of a simple radial motion. There is also a positive asymmtry observed at negative radial velocity phases (negative γ). We do not display the spectra with their phases because of the complication introduced by the orbital motion.

The acceleration curve (Fig. 3.24) has a maximum of $\sim$ 0.4 m s^{-2} and is more similar in shape to that of W Sgr than to those of β Dor and S Nor. S Mus has a radius full amplitude of $\sim$ 8 $R_\odot$.

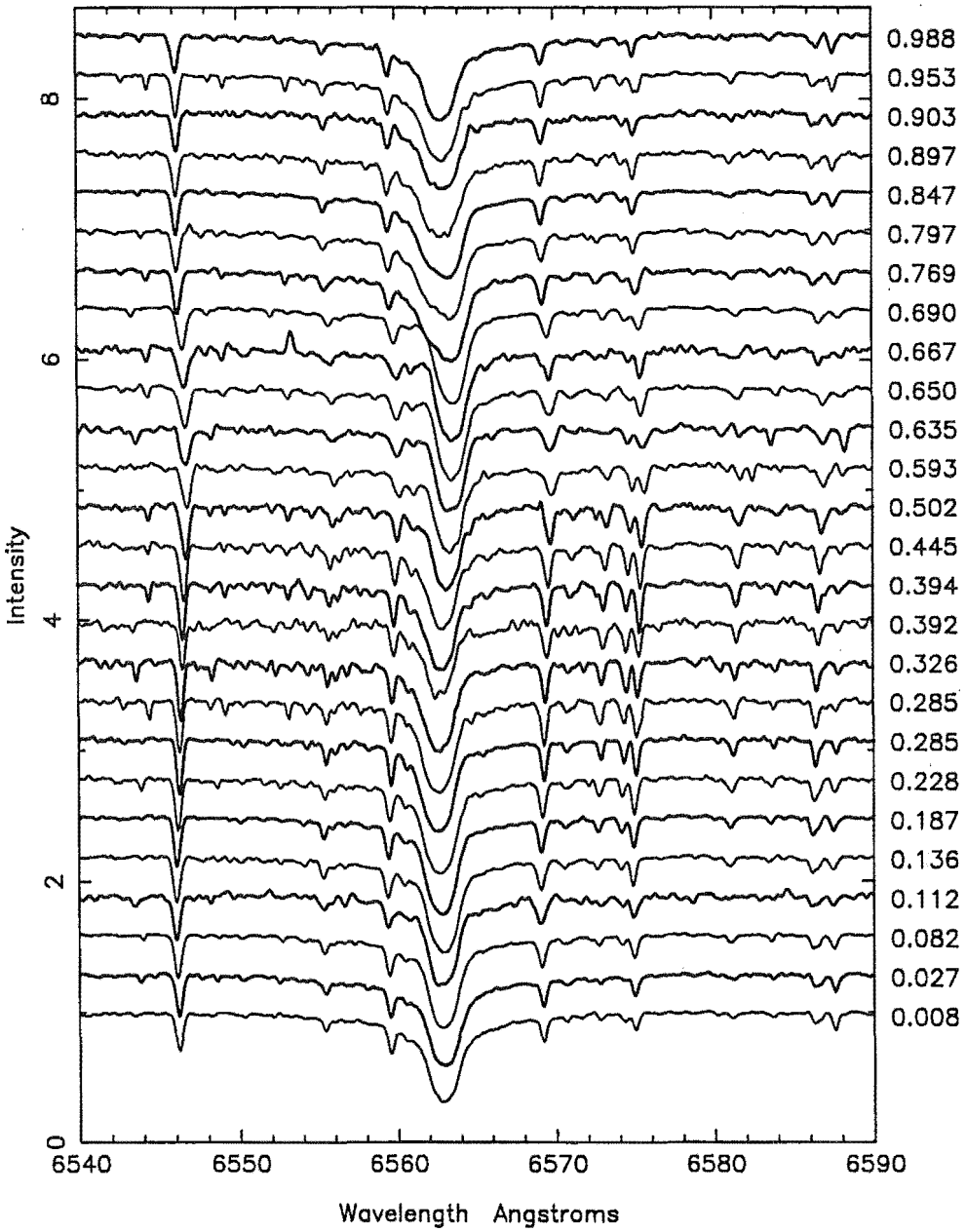

Figure 3.15: Stacked spectra of S Nor in phase order from bottom to top.

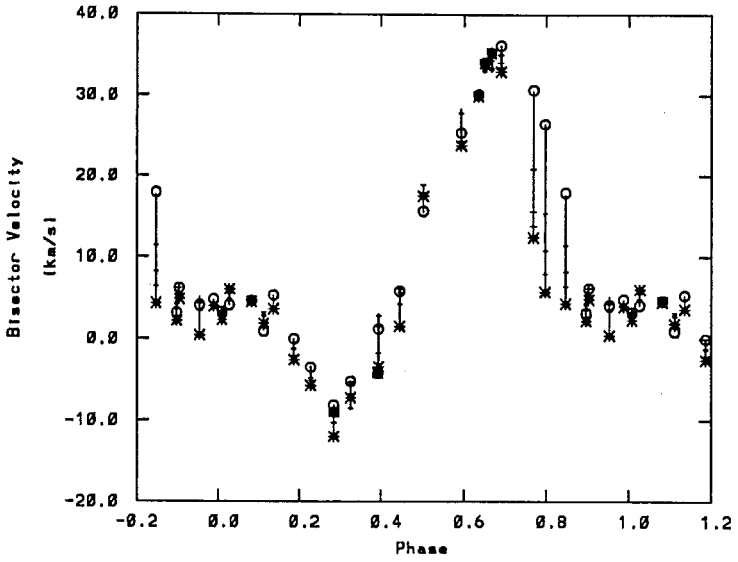

Figure 3.16: Radial velocity curve for the Hα line for S Nor.

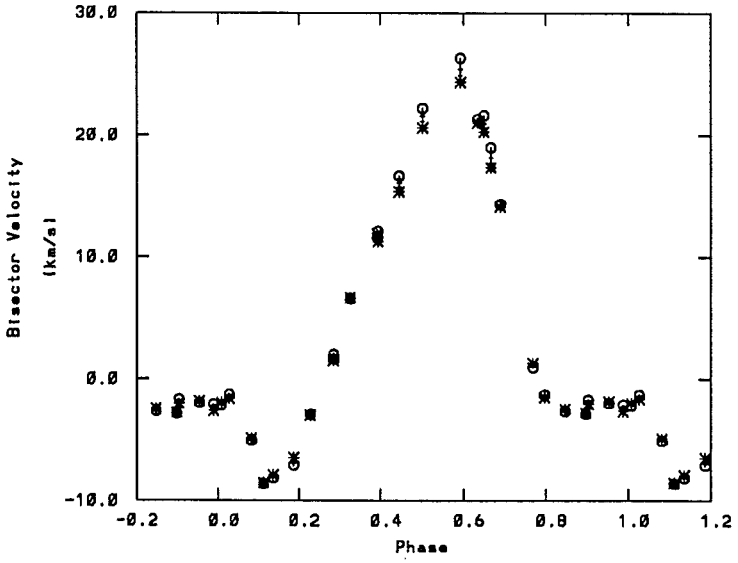

Figure 3.17: Radial velocity curve for the 6546 Å line for S Nor.

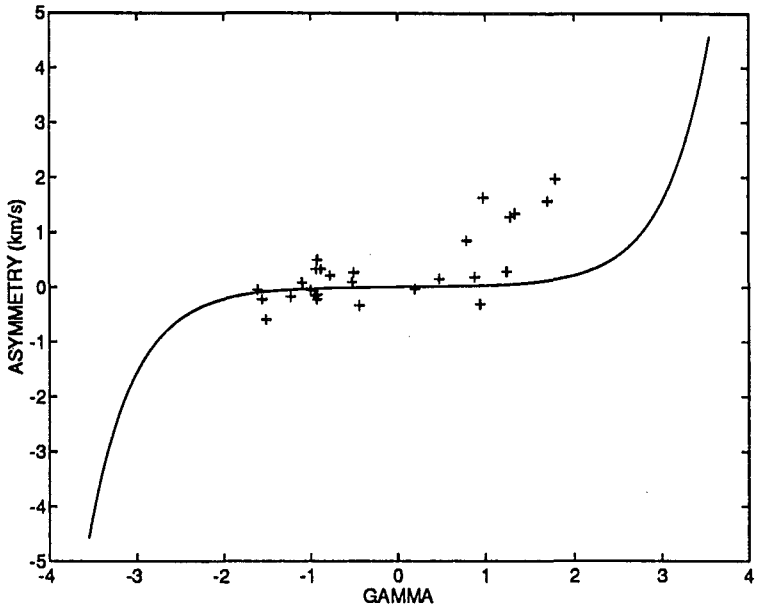

Figure 3.18: As for Fig. 3.6 for S Nor.

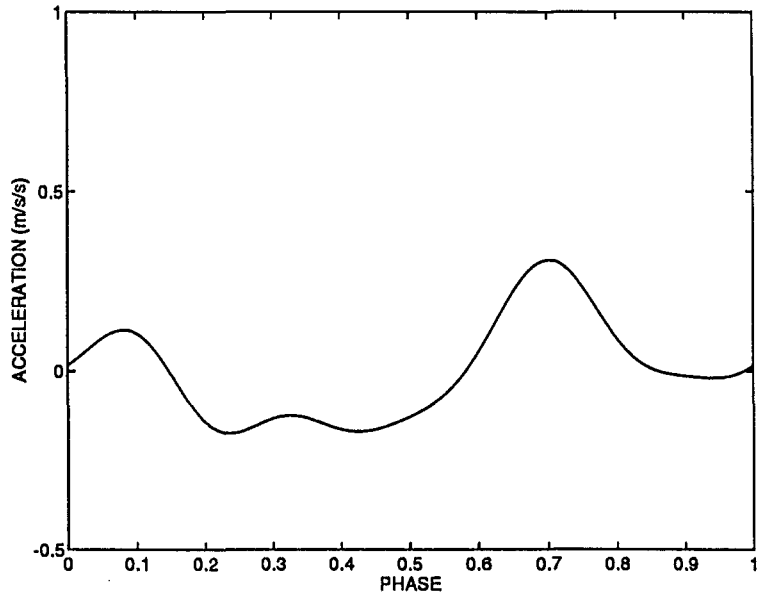

Figure 3.19: Acceleration curve for S Nor.

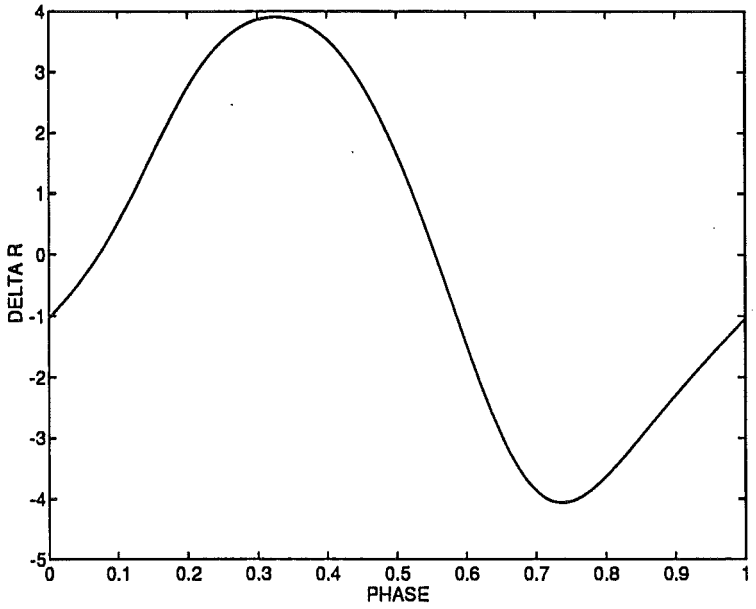

Figure 3.20: Radius curve for S Nor in units of $R_\odot$.

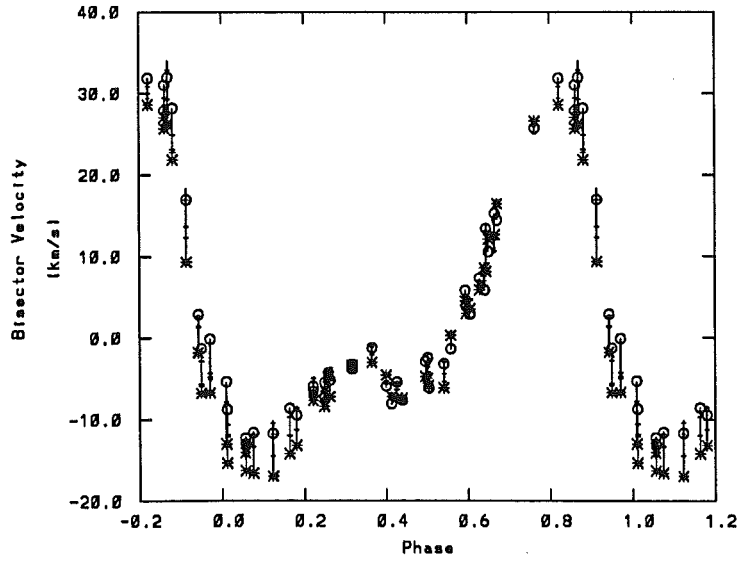

Figure 3.21: Radial velocity curve for the Hα line for S Mus.

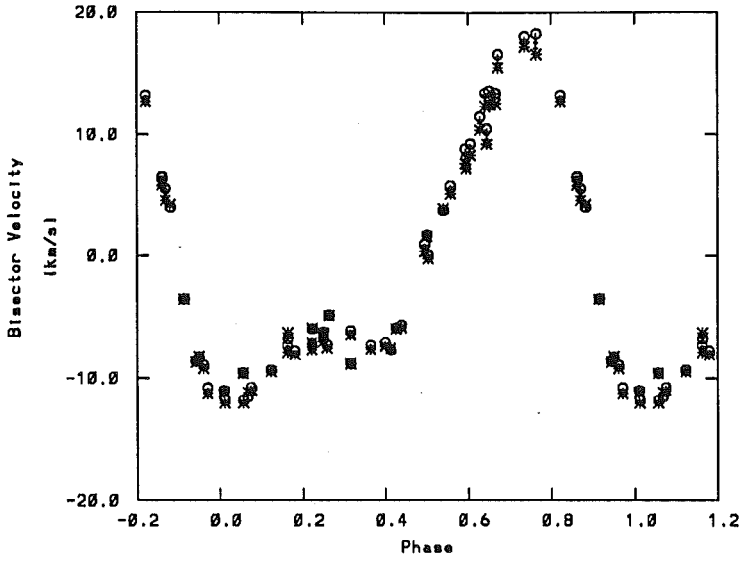

Figure 3.22: Radial velocity curve for the 6546 Å line for S Mus.

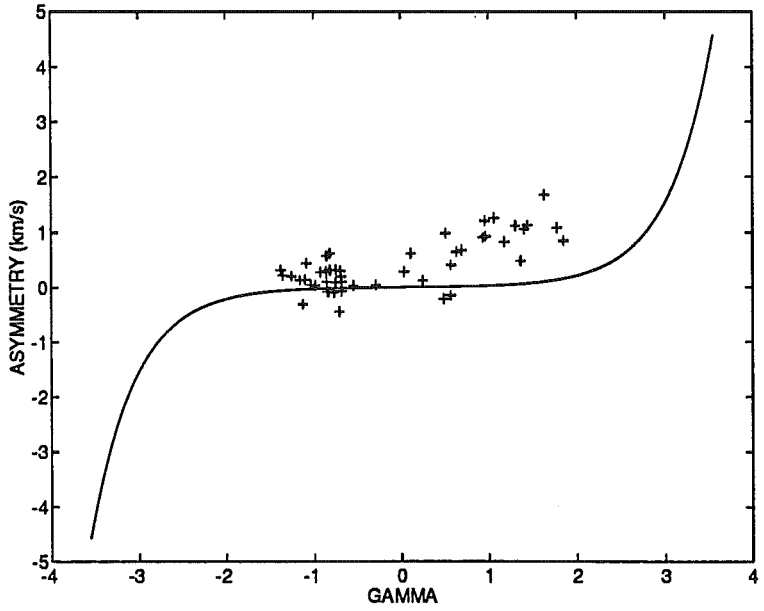

Figure 3.23: As for Fig. 3.6 for S Mus.

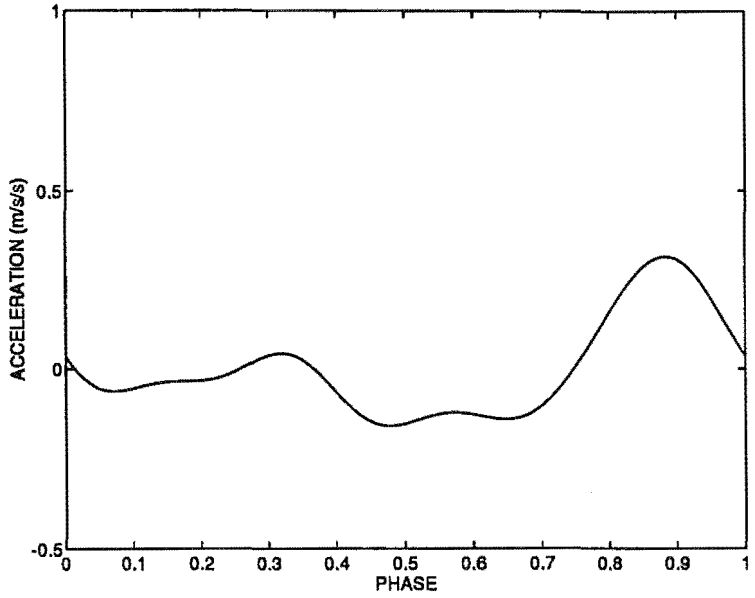

Figure 3.24: Acceleration curve for S Mus.

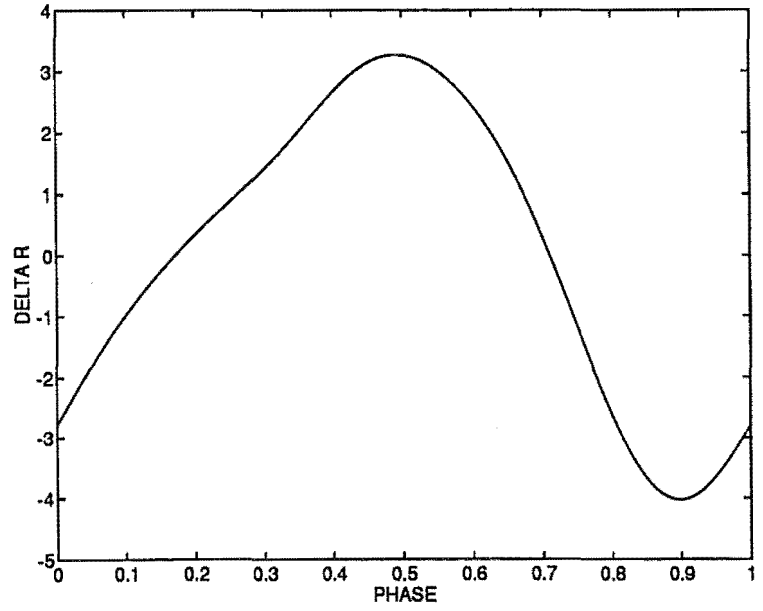

Figure 3.25: Radius curve for S Mus in units of $R_\odot$.

3.9 κ Pav

The type II Cepheid, κ Pav, is thought to be the brightest and nearest Cepheid of the disc population. It has been found to have a solar iron content, but possibly an underabundance of r and s-process elements (Luck & Bond 1989), while its systemic radial velocity and galactic latitude are around three times the dispersion for classical Cepheids. Using the maximum likelihood variation of the Baade-Wesselink method, Balona (1977) determined a radius for κ Pav of 26.2 $R_\odot$, compared with radii of between 55 and 75 $R_\odot$ for classical Cepheids of the same period. There is no evidence for κ Pav being a binary system, although Harris & Welch (1989) have proposed that mass transfer to a secondary companion star provides a plausible mechanism for the reduction in mass of the hydrogen envelope which is needed for a low-mass metal-rich star to become hot enough to occupy the instability strip. The pulsational period is $\sim$ 9.09 days and has been found to be somewhat unstable (Shobbrook 1992).

The radial velocity curves of κ Pav have full amplitudes of 50 km s^{-1} and 45 km s^{-1} for Hα measured at line depths 0.9 and 0.5 respectively, and 30 km s^{-1} for the metallic lines (Figs 3.27 and 3.28). The Hα line profiles (Fig. 3.26) are quite asymmetric at phases 0.6 - 0.8 where the pulsational velocity changes from inward to outward motion and for $\sim$ 0.2 cycle afterwards. Multiple components can be seen in some of the spectra. The shape of the Hα radial velocity curve is quite different than that of the type I (classical) Cepheids, in that this velocity reversal happens relatively slowly. In contrast, the metallic line curve has quite an abrupt reversal. The metallic line profiles show a positive asymmetry for the whole of the pulsation cycle (Fig. 3.29), which is quite incompatible with geometric projection of a single atmospheric velocity at a given phase. One spectrum, taken during the velocity reversal (phase 0.6), shows a large negative asymmetry which is likely due to large velocity gradients in the atmosphere at this time.

The acceleration curve of κ Pav has a maximum of $\sim$ 0.6 m s^{-2} (Fig. 3.30). The full amplitude of the radius curve is $\sim$ 7 $R_\odot$ which is $\sim$ 25 per cent of the assumed stellar radius.

3.10 Y Oph

The low amplitude Cepheid Y Oph has a pulsation period P = 17.12 days and is considered unusual in many respects. Fernie (1990) finds that the visual light

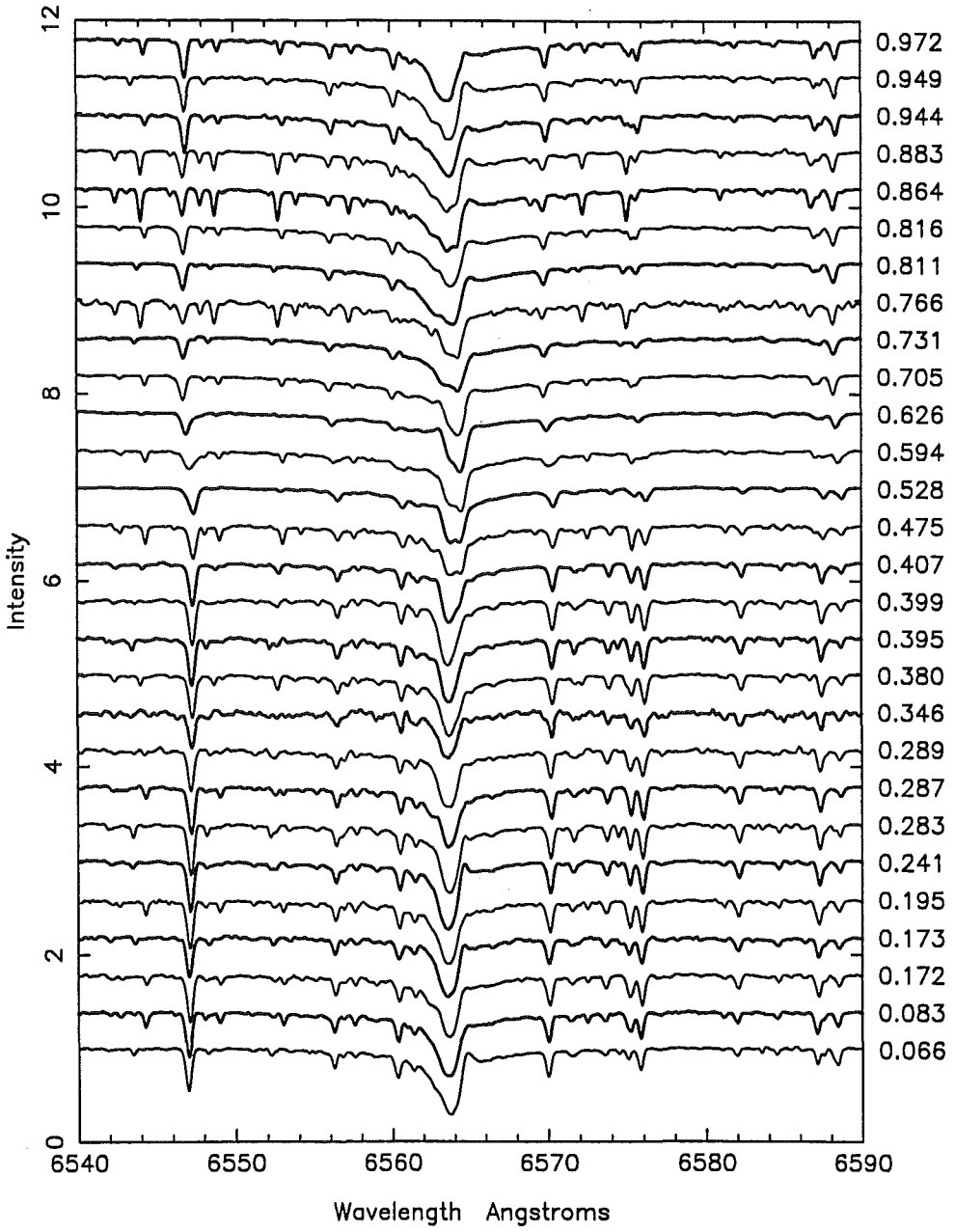

Figure 3.26: Stacked spectra of κ Pav in phase order from bottom to top.

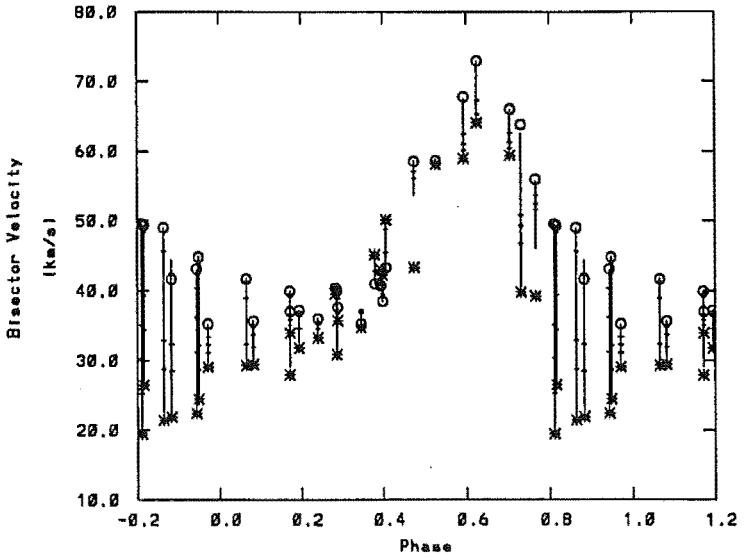

Figure 3.27: Radial velocity curve for the Hα line for κ Pav.

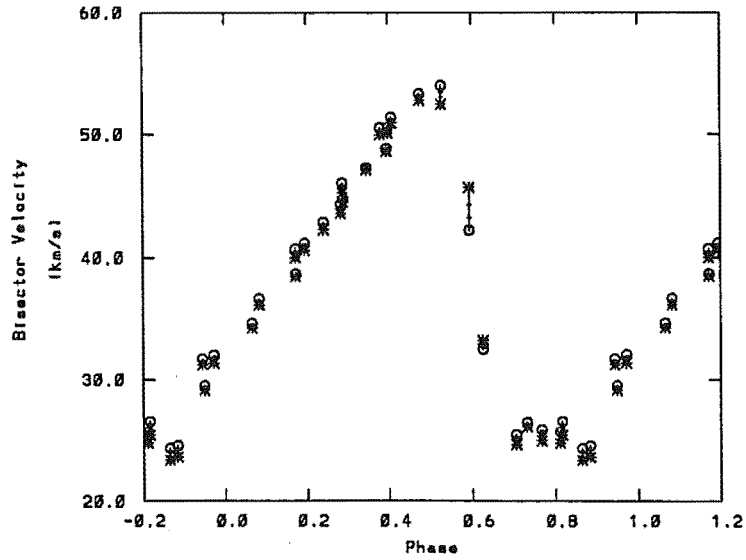

Figure 3.28: Radial velocity curve for the 6546 Å line for κ Pav.

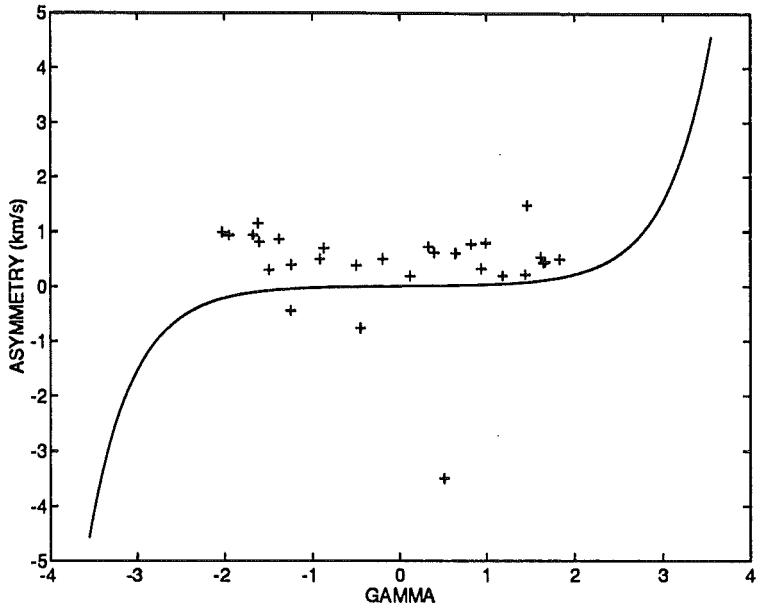

Figure 3.29: As for Fig. 3.6 for κ Pav.

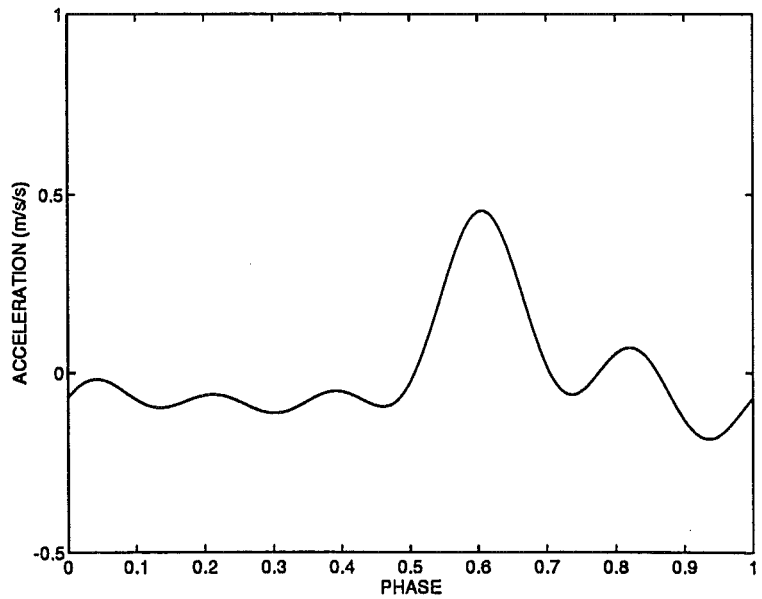

Figure 3.30: Acceleration curve for κ Pav.

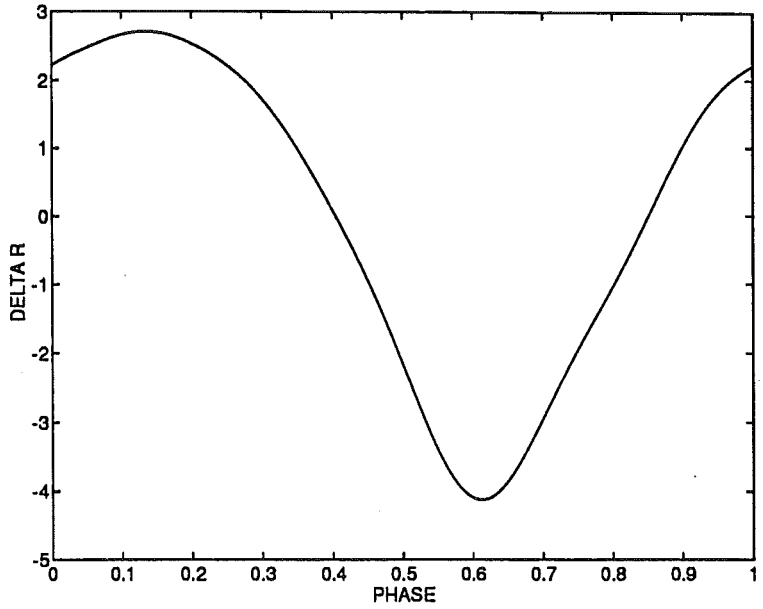

Figure 3.31: Radius curve for κ Pav in units of $R_\odot$.

amplitude of the star may have declined from 0.7 magnitudes to 0.5 magnitudes over the last century. He also calculates that the period is currently changing by $\sim 1.8\text{x}10^{-3}$ days/cycle.

Gieren, Barnes & Moffett (1989) report a mean surface brightness radius of 71.88 $R_\odot$, while Hindsley & Bell (1989) find a Barnes-Evans radius between 104 and 111 $R_\odot$. Coulson & Caldwell (1989) determine Baade-Wesselink radii in the range 86 to 92 $R_\odot$, depending on which colour indices were used. Y Oph is possibly a spectroscopic binary with an orbital period of $\sim$ 1200 days (Szabados 1989). Evans (1992a) has shown that it does not have a companion hotter than spectral type A0. Laney & Stobie (1993) find that Y Oph is redder than other Cepheids of a similar pulsation period which indicates the possible presence of a faint red companion. Gieren (1989) reports a Wesselink mass, $M_{WES} = 3.3\ M_\odot$ and pulsation mass, $M_{PUL} = 3.5\ M_\odot$ but an evolutionary mass, $M_{EV} = 7.1\ M_\odot$ for Y Oph.

The radial velocity full amplitude is $\sim$ 18 km s^{-1} for the metallic lines and $\sim$ 20 km s^{-1} for Hα (at line depths 0.5 and 0.9). The Hα and metallic line radial velocity curves (Figs 3.33 and 3.34) are very symmetrical, taking about the same time to change from radial velocity maxima to minima as from minima to maxima. There is little phase difference between the two curves. A relatively

small amount of Hα asymmetry is present at phases of negative radial velocity and the metallic lines show some asymmetry at positive radial velocity phases.

The acceleration curve (Fig. 3.36) is of low amplitude ($\sim$ 0.1 m s^{-2} in each direction) and the radius curve has a full amplitude of $\sim$ 9 R$_\odot$. This is again around 10 per cent of the mean radius. The atmosphere seems to be very gently rising and falling as the star pulsates. Wallerstein et al. (1992) comment that this gentle motion means that Baade-Wesselink radii may be more accurate for this star than for the majority of Cepheids. However, the presence of a positive asymmetry at negative radial velocity phases (Fig. 3.35) casts some doubt upon this supposition.

3.11 U Car

U Car is the longest period (38 days) and most luminous Cepheid in our survey. Shobbrook (1992) finds the period to be somewhat unstable. Gieren (1989) estimates a mass for U Car in the range 8.4 M$_\odot$ $\leqslant$ M $\leqslant$ 10.8 M$_\odot$. The radius has been estimated as between 151 and 163 R$_\odot$ by Coulson & Caldwell (1989) and 169 R$_\odot$ by Gieren, Barnes & Moffett (1989).

The line profiles of Hα (Fig. 3.38) are quite asymmetric and multiple components are visible at certain phases. The radial velocity amplitudes are $\sim$ 50 km s^{-1} for the metallic lines and $\sim$ 45 km s^{-1} for Hα measured at a line depth of 0.9 (Figs 3.39 and 3.40). The γ-velocity of the Hα curve measured at line depth 0.9 is displaced from that of the metallic line velocities by $\sim$ 20 km s^{-1} and the curves are of quite a different shape. The Hα radial velocity curve measured at line depth 0.5 has a full amplitude of $\sim$ 55 km s^{-1} but is displaced by $\sim$ 10 km s^{-1} from the metallic line curve to which it is qualitatively similar. The asymmetry of the 6546 Å Fe I line clearly reverses with phase in this star. At positive radial velocity phases the asymmetry is again greater than our single-velocity model would predict. At negative velocity phases there is a large scatter in the measured asymmetries. The spectrum taken at phase 0.210 (Fig. 3.38) shows a large asymmetry of $\sim$ 4 km s^{-1} in the 6546 Å line. This appears to be real because a similar asymmetry is clearly visible in the 6569 Å Fe I line in the same spectrum. This observation was not from the same cycle as the spectra on either side so it appears that there may be some cycle to cycle variation. Further observations are required to properly investigate this hypothesis.

The radius full amplitude of $\sim$ 50 R$_\odot$ (Fig. 3.43) is $\sim$ 30 per cent of the mean

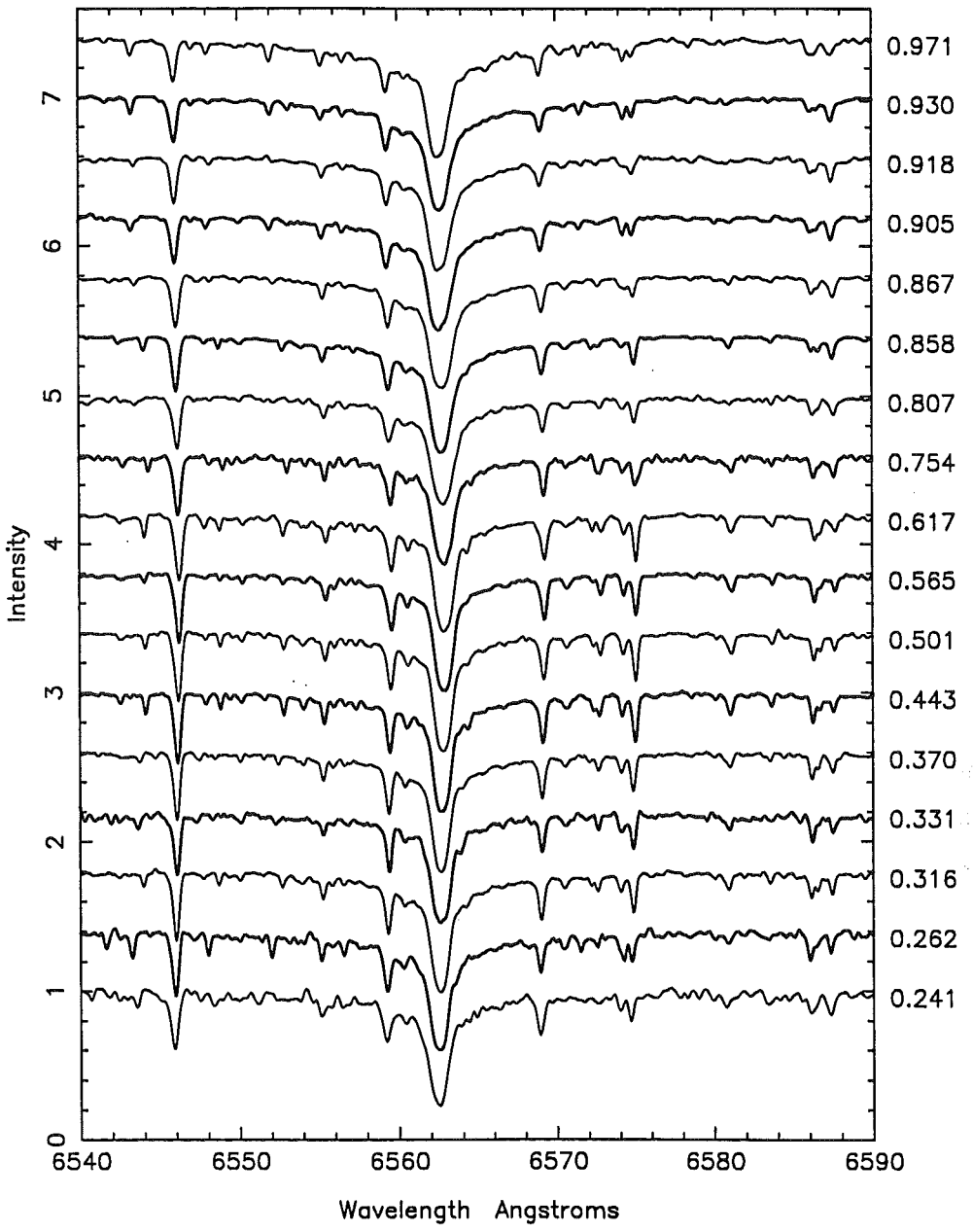

Figure 3.32: Stacked spectra of Y Oph in phase order from bottom to top.

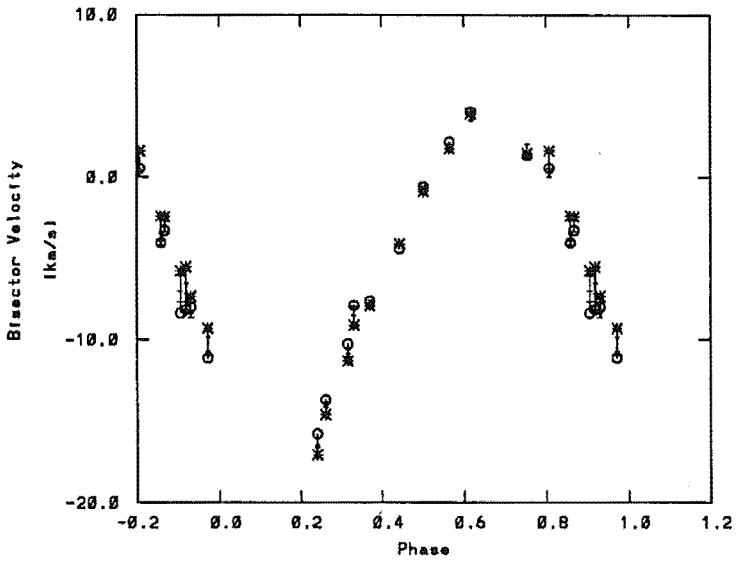

Figure 3.33: Radial velocity curve for the Hα line for Y Oph.

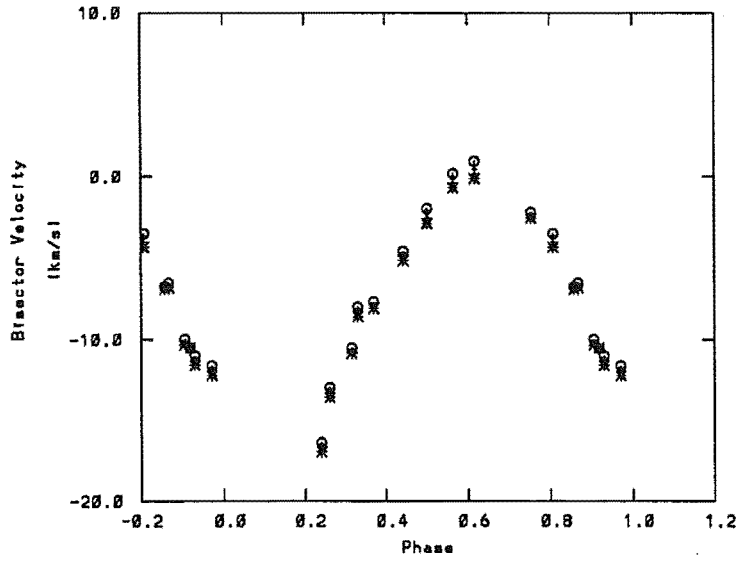

Figure 3.34: Radial velocity curve for the 6546 Å line for Y Oph.

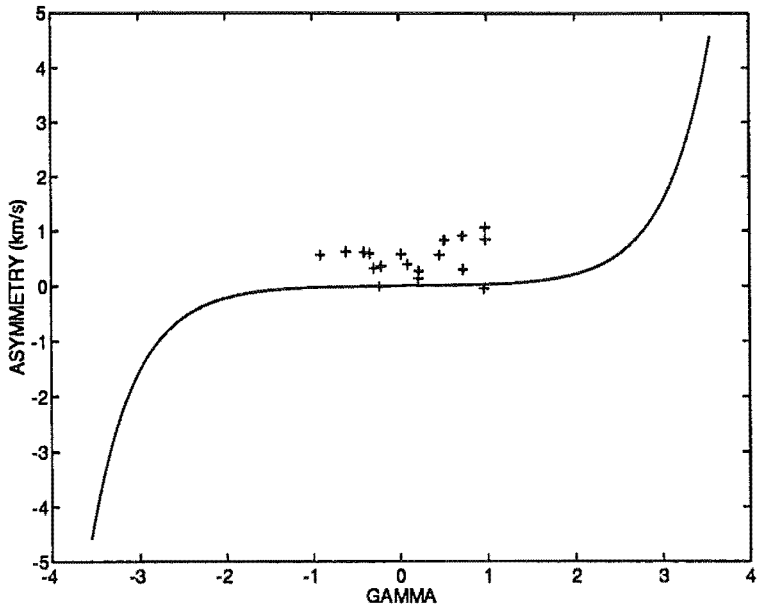

Figure 3.35: As for Fig. 3.6 for Y Oph.

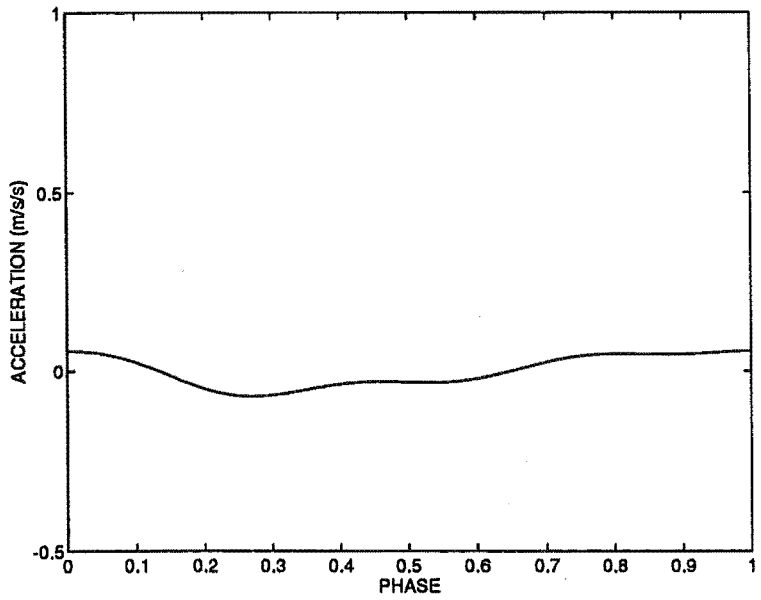

Figure 3.36: Acceleration curve for Y Oph.

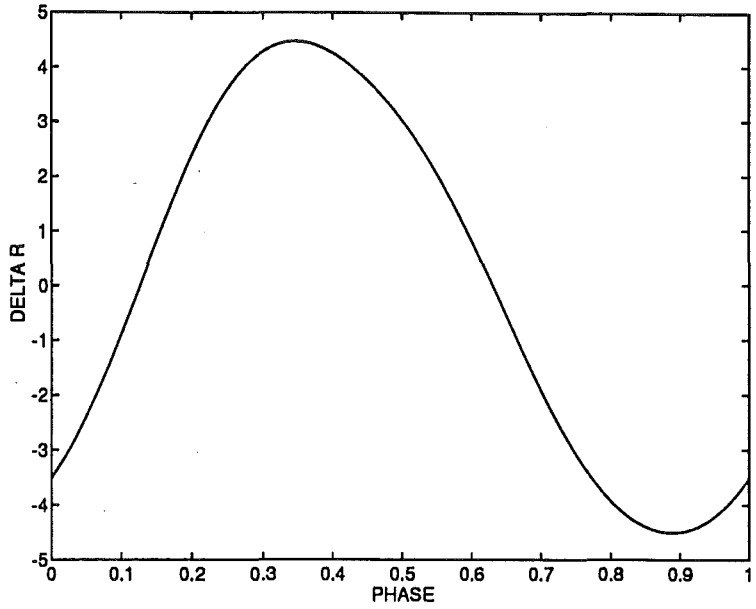

Figure 3.37: Radius curve for Y Oph in units of $R_\odot$.

radius of U Car.

3.12 Summary of dynamic parameters

Before discussing the line asymmetries, we conclude this observational section by summarising in Table 3.3 the information on the dynamics of each star that we have derived from the Fourier series fits to the radial velocities. We will use these parameters for comparison with the model we calculate in the following chapters.

3.13 Discussion

An implicit assumption of any Baade-Wesselink analysis is that the velocity field is constant throughout the line forming region of the stellar atmosphere. The projection factors calculated by various authors are only applicable in this case. All of the Cepheids discussed above have line profiles which are not consistent with a single radial pulsation velocity for at least part of their cycles. The errors resulting from this are not readily apparent. For each of the programme stars, we calculated pulsation velocity curves for line depths 0.5 and 0.9 by multiplying

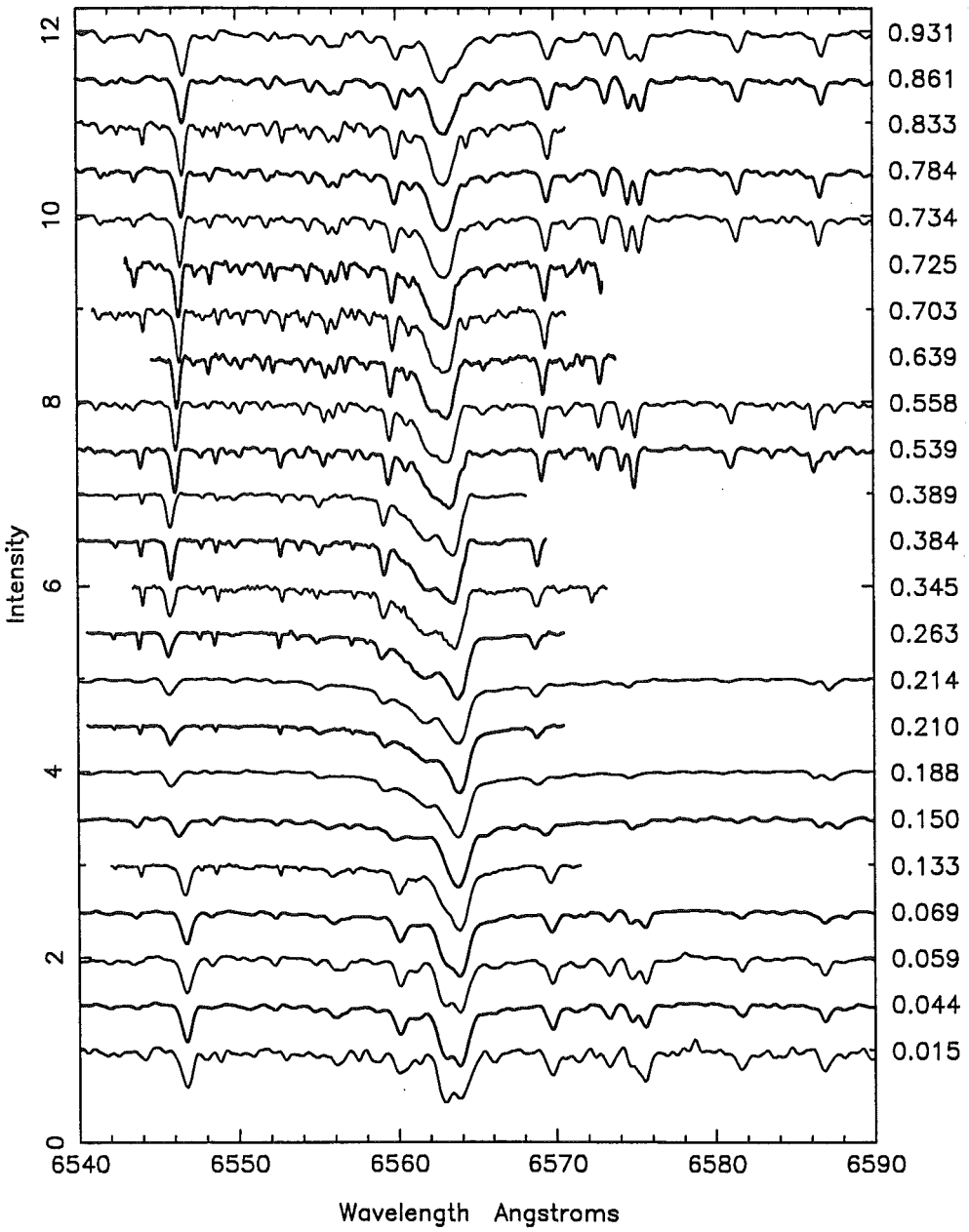

Figure 3.38: Stacked spectra of U Car in phase order from bottom to top.

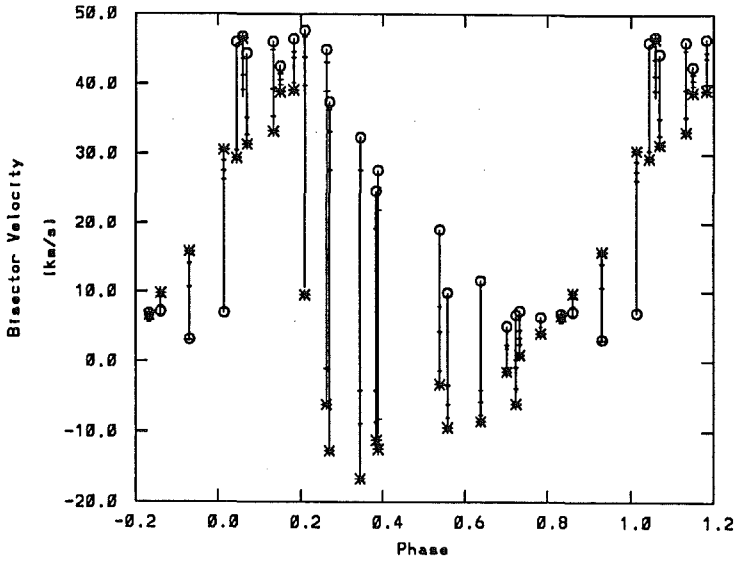

Figure 3.39: Radial velocity curve for the Hα line for U Car.

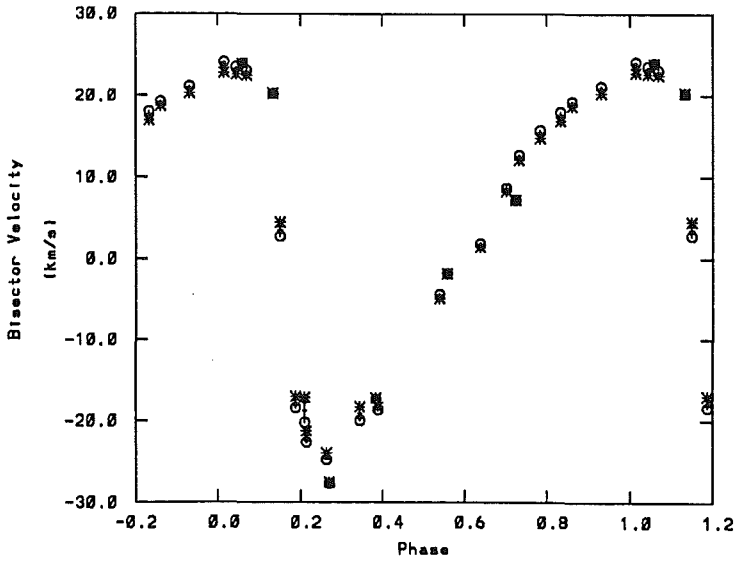

Figure 3.40: Radial velocity curve for the 6546 Å line for U Car.

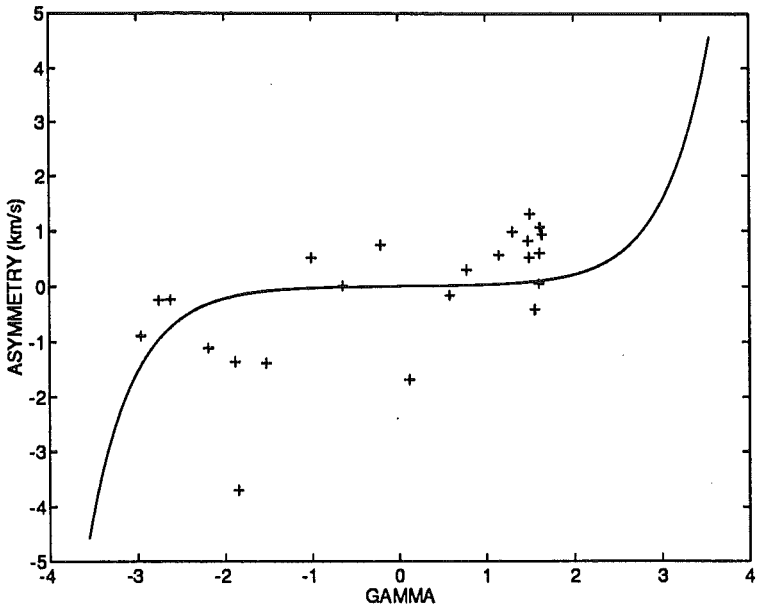

Figure 3.41: As for Fig. 3.6 for U Car.

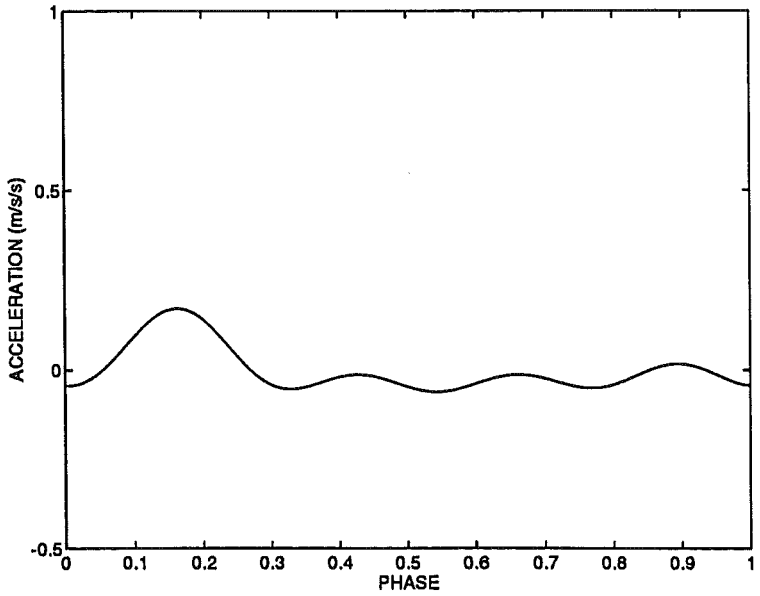

Figure 3.42: Acceleration curve for U Car.

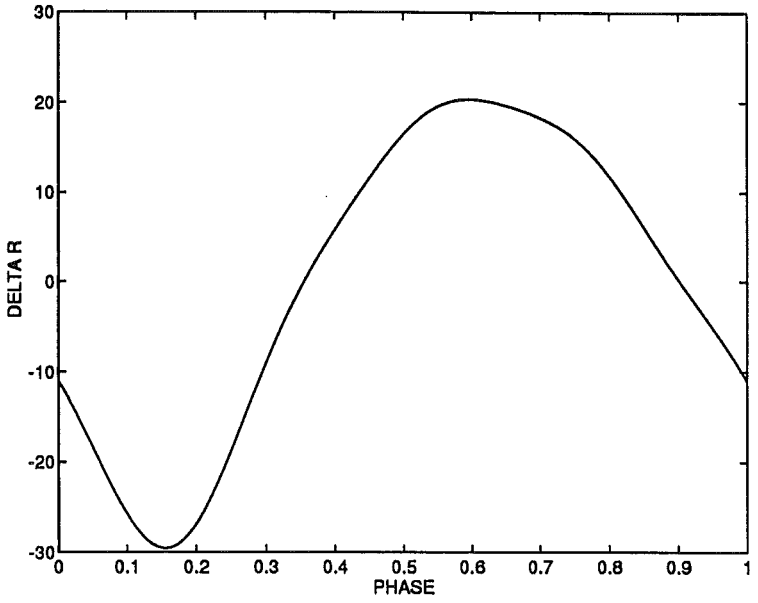

Figure 3.43: Radius curve for U Car in units of $R_\odot$.

Table 3.3: Summary of acceleration and radius amplitudes

Star	period (d)	pulsational velocity amplitude (km s^{-1})	maximum acceleration (m s^{-2})	radius amplitude ($R_\odot$)
W Sgr	7.59	58.2	0.69	6.8
β Dor	9.84	45.6	0.25	7.9
S Nor	9.75	46.5	0.31	8.0
S Mus	9.66	41.7	0.32	7.3
κ Pav	9.09	42.1	0.46	6.8
Y Oph	17.13	29.1	-0.07	9.0
U Car	38.77	73.8	0.17	49.8

the fitted radial velocity curves by the projection factor appropriate for that line depth. The differences between the pulsation velocity curves for each line depth for a given star were less than the sum of the standard deviations of the fits given in Table 3.2. This suggests that little error is introduced by amplitude differences between the radial velocity curves for the two line depths. We can see from Figs 3.5, 3.11, 3.17, 3.22, 3.28, 3.34 and 3.40 that different γ-velocities will be determined for each of these stars depending on what depth in the line profile radial velocity measurements are made. The difference is typically 0.4 km s^{-1} for the Cepheids on our programme between line depths 0.5 and 0.9. Obviously at most one of these γ-velocities can represent the true value. Using a simple analysis similar to that of Oke, Giver & Searle (1962), we estimate that errors of this magnitude in γ-velocity will lead to $\sim$ 4 per cent differences in derived radii. This, of course, still assumes that the radial velocity represents a continuous projection of the pulsation velocity at some part of the stellar atmosphere. This cannot be true for both line depths at all phases else the γ-velocities would be the same.

A likely cause of the discrepant asymmetries is velocity gradients throughout the line forming region of the stellar atmosphere. This mechanism is more likely in strong lines (Karp 1975), which are formed over comparatively larger geometrical distances and generally further out from the continuum than the weak lines. Modelling of spectral lines from model atmospheres with velocity gradients will be discussed in Chapters 5 and 6.

In their infrared study of the 7 d Cepheids X Sgr and η Aql, Sasselov, Lester & Fieldus (1989) speculate that an unexplained asymmetry may be due to the presence of an additional absorption core, originating in material spatially separated in the stellar atmosphere, but unresolved from the main line profile.

Another mechanism which causes asymmetry in the line profiles of non-pulsating stars is granulation. This can give rise to spectral lines which have a curved bisector. The effect is found to be largest in supergiant stars (Gray and Toner, 1986). We have measured the amount of asymmetry between line depths 0.5 and 0.9 as a function of spectral type for Ib supergiants from Fig. 2 of that paper. The asymmetry of these bisectors varies with spectral type and has a maximum magnitude of 0.4 km s^{-1}, which occurs for spectral types $\sim$ F7 - G0. This spectral type range is similar to that of the Cepheids and the asymmetry

seems to be in the correct direction. However, one cannot simply add asymmetries from different effects and the magnitude seems too small to account for the observed asymmetry.

In Chapter 2 (see Fig. 2.17) we showed how a negative asymmetry can be produced by the combination of radial macroturbulence and low pulsation velocities. The magnitude of this effect is almost large enough to mimic the negative asymmetries observed in κ Pav and Y Oph at phases of outward pulsation. However, this explanation is not compatible with the asymmetry observed during phases of inward motion. It seems appropriate to investigate this further before reaching any definite opinion as to the cause.

Chapter 4

A model Cepheid

4.1 Introduction

In order to try and explain our observations of line profile asymmetries, we need to create a model of a Cepheid atmosphere. The approach we have used is similar to that of Bessell et al (1989a, 1989b). The ATLAS code (Kurucz 1970, 1992) is used to converge model atmospheres based on snapshots of the outer layers of a previously generated hydrodynamic model.

4.2 Hydrodynamic model

The hydrodynamic model was generated using a code written by Dr Peter Wood and described in Wood (1974) and Fox & Wood (1982). Essentially, the code solves a set of four coupled nonlinear differential equations:

$$\frac{\partial r}{\partial m} = \frac{1}{4\pi r^2 \rho}, \tag{4.1}$$

$$\frac{\partial P}{\partial m} = -\frac{1}{4\pi r^2}\left(g + \frac{\partial^2 r}{\partial t^2}\right), \tag{4.2}$$

$$\frac{\partial L}{\partial m} = \frac{P}{\rho^2}\frac{\partial \rho}{\partial t} - \frac{\partial U}{\partial t}, \tag{4.3}$$

$$L = -\frac{256\pi^2 \sigma r^4 T^3}{3\kappa}\frac{\partial T}{\partial m}. \tag{4.4}$$

These are, respectively, the equations of conservation of mass, momentum and energy and the energy transport equation in the diffusion approximation. The star is divided into mass zones and the differential equations written as spatial and temporal difference equations (Fraley 1968).

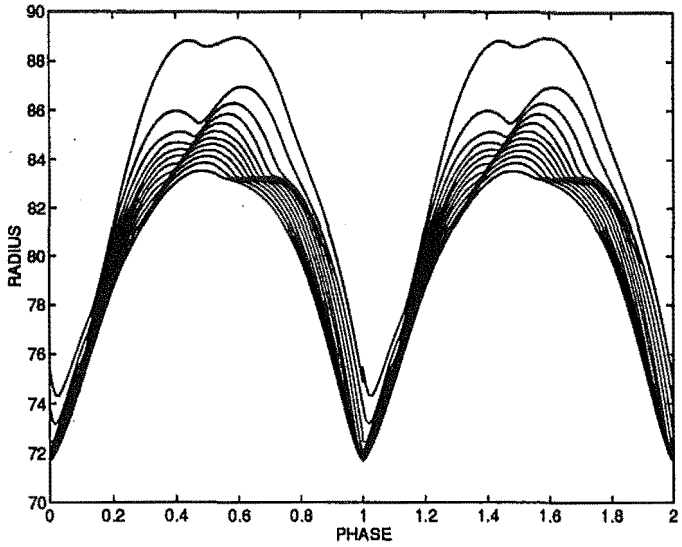

Figure 4.1: Radius of the hydrodynamic model as a function of phase. Shown are zones 1,2,4,7,11,16,22,29,37,46,56,67.

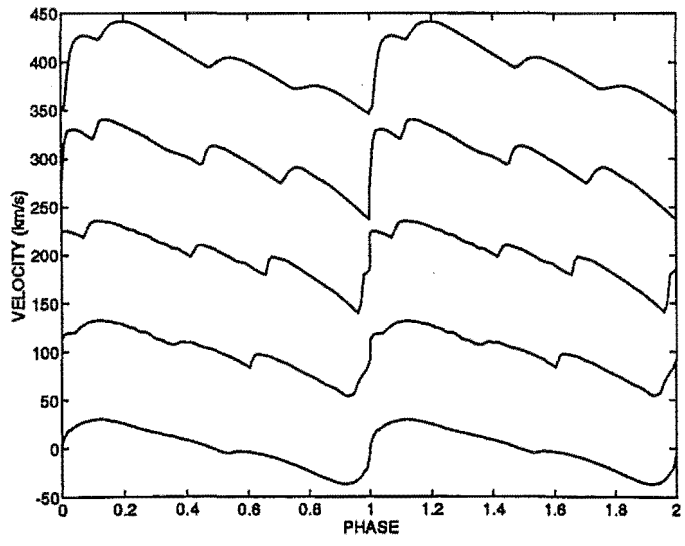

Figure 4.2: Velocity of the hydrodynamic model as a function of phase. Shown are zones 1,4,16,37,67. Successive zones are offset by 100 km s^{-1}.

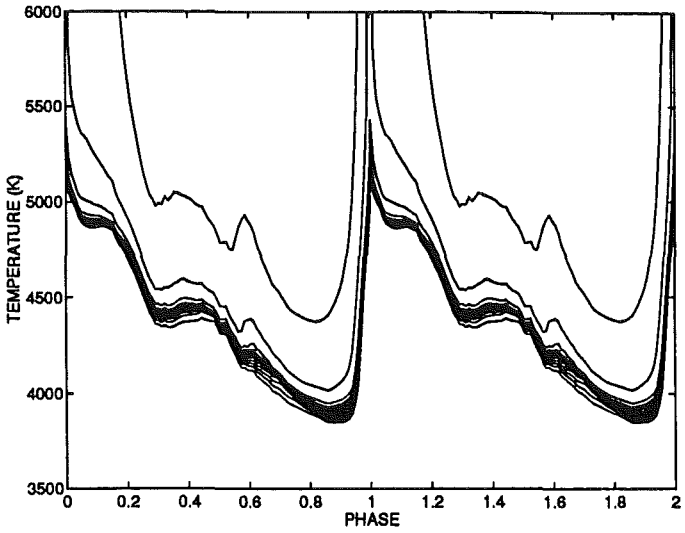

Figure 4.3: Temperature of the hydrodynamic model as a function of phase. Shown are zones 1,2,4,7,11,16,22,29,37,46,56,67.

A solar abundance mix was used for the calculations, with Y = 0.28 and Z = 0.016. Opacities were taken from the Los Alamos Opacity Library (Huebner *et al* 1977) with the heavy element ratios of Ross & Aller (1976). Some approximation to molecular opacities were added at low temperatures, as described in Bessell *et al* (1989b). Recently, new opacities have been calculated by Iglesias & Rogers (1991a, 1991b) and Rogers & Iglesias (1992). These opacities are not expected to make large differences to Cepheid models (Chiosi, Wood & Capitanio 1993), but nevertheless should be used for any future calculations.

Convection was included using standard mixing length theory (Böhm-Vitense 1958), but with the convective velocity constrained to vary only on a convective timescale. A value of 1.5 was used for the ratio of mixing length to pressure scale height.

The model has a mass of 7 $M_\odot$, mean luminosity 5000 $L_\odot$, period 10.8 d and mean effective temperature 5550 K. This choice of mass and luminosity corresponds to an evolutionary model with mild convective overshoot (Chiosi, Wood & Capitanio 1993) which is 0.13 greater in $\log(L/L_\odot)$ than the second crossing evolutionary models of Becker, Iben & Tuggle (1977) which do not have convective overshoot. The effective temperature is close to the centre of the fundamental mode instability strip at this luminosity. The zoning was fine enough

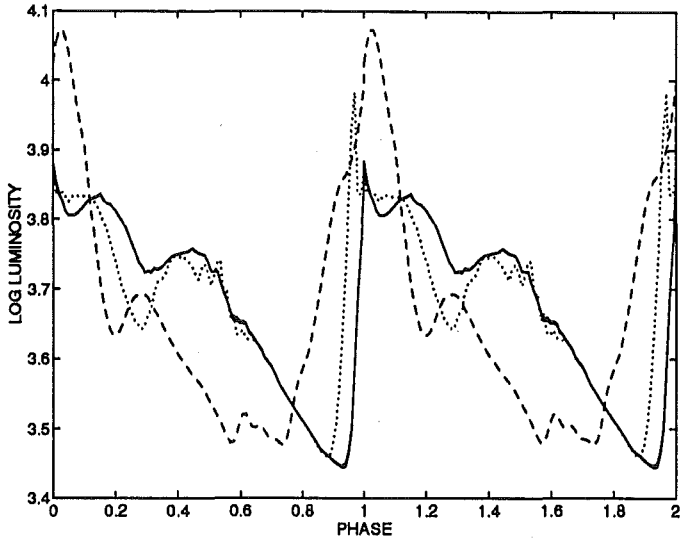

Figure 4.4: Luminosity of the hydrodynamic model as a function of phase. Shown are zones 1,2,4,7,11,16,22,29,37,46,56 ———,79 ·····, 106 - - - -.

that $\sim$ 35 zones were contained within one optical depth of the surface.

The model reached a stable fundamental mode pulsation with a maximum pulsational velocity of $\sim$ 50 km s^{-1} in the outermost layers. This velocity amplitude is high, but not unknown, for a Cepheid of this period (Carson and Stothers 1988). There is a continuing problem in stellar pulsation theory as to what determines the pulsation amplitude of Cepheids (Fernie, Kamper & Seager 1993).

The behaviour of the atmospheric velocity field with phase is shown in Figs 4.1 and 4.2. The effective temperature of the model varied from 4800K to 6200K over a cycle. Figs 4.3 - 4.6 show the luminosity, temperature, density and pressure curves for some of the outermost zones in the model. Outward moving waves take approximately 0.1 cycles to propagate through the stellar atmosphere. This is a time period similar to the observed phase delay between radial velocity maxima of Hα and metallic lines (see Chapter 3). Considerable velocity stratification exists at certain phases and the impact of this on spectral line profiles will be investigated in Chapters 5 and 6.

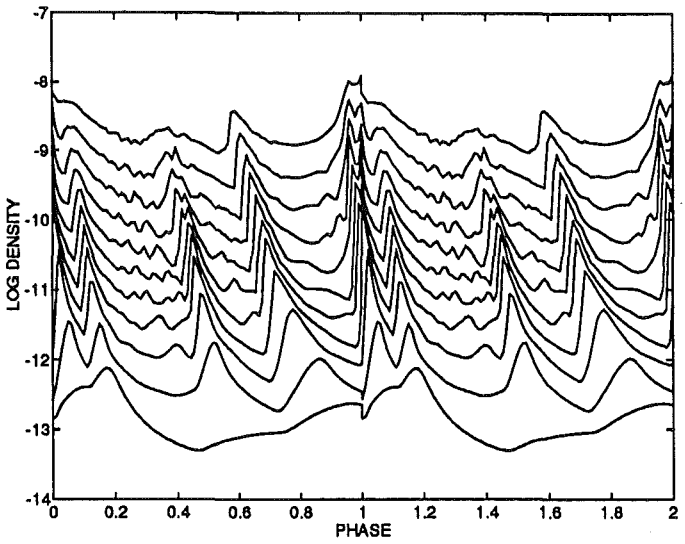

Figure 4.5: Density of the hydrodynamic model as a function of phase. Shown are zones 1,2,4,7,11,16,22,29,37,46,56.

4.3 Model atmospheres

The radius, density, pressure and temperature of each zone in the outer layers of the model were extracted at 22 equally spaced phase intervals spanning one cycle. Zones included were all those up to a depth where the temperature reached four times the effective temperature. The ATLAS9 code was used to converge flux-constant model atmospheres using the temperature as a function of $rhox$ ($= \int \rho dx$) from the hydrodynamic model as the initial model.

The equations of statistical equilibrium and radiative transfer were treated as if the atmosphere was in LTE and static. Some justification for this approach has been given by Keller & Mutschlecner (1970), who found that their hydrodynamic calculations were not strongly influenced by the mode of treatment of the radiation field. Line blanketing is treated through the opacity distribution functions from the 'new' calculations of Kurucz (1991). We have used the low resolution version which contains 328 wavelength intervals.

Each model was converged so that its effective temperature was the same as that given by the diffusion approximation hydrodynamic code. This is a reasonable assumption because effective temperatures derived from hydrodynamic models accurately predict the blue edge of the observed Cepheid instability strip (Chiosi and Wood 1993). In general, flux constancy at any time is not an ab initio

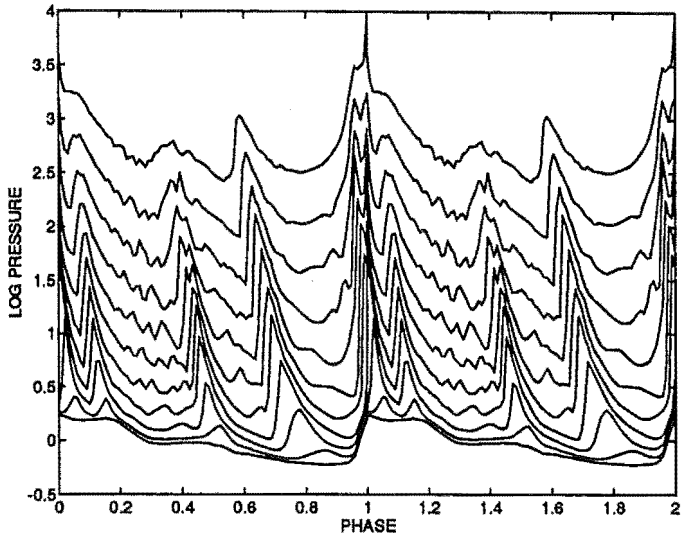

Figure 4.6: Pressure of the hydrodynamic model as a function of phase. Shown are zones 1,2,4,7,11,16,22,29,37,46,56.

requirement of a hydrodynamic atmosphere. Rather, the flux integrated over a pulsation cycle should be the same for any zone. However, it can be shown from thermodynamic considerations that luminosity variations are effectively frozen in the outer non-adiabatic layers of the stellar envelope (Cox 1974). This effect can be seen in Fig. 4.4.

To keep the structure of the hydrodynamic model, we retained the pressure as a function of *rhox* and made only temperature corrections until the flux was constant throughout the atmosphere. In practice, flux constancy of 4 per cent or (usually) better was achieved for all of the models up to at least a Rosselind mean optical depth of 5.

The temperature correction algorithms are fully explained in Kurucz (1970). Briefly, the code uses a correction based on flux errors derived by Avrett and Krook (1963) in the inner layers. Nearer the surface, where the temperature is insensitive to the flux, a correction based on the flux derivative (Λ correction), similar to that of Böhm-Vitense (1964), is used. Both of these corrections are modified to include the effects of convection. Finally, a correction is made to smooth out the region near optical depth unity where the first two corrections overlap.

The equation of hydrostatic equilibrium in ATLAS was not solved and the

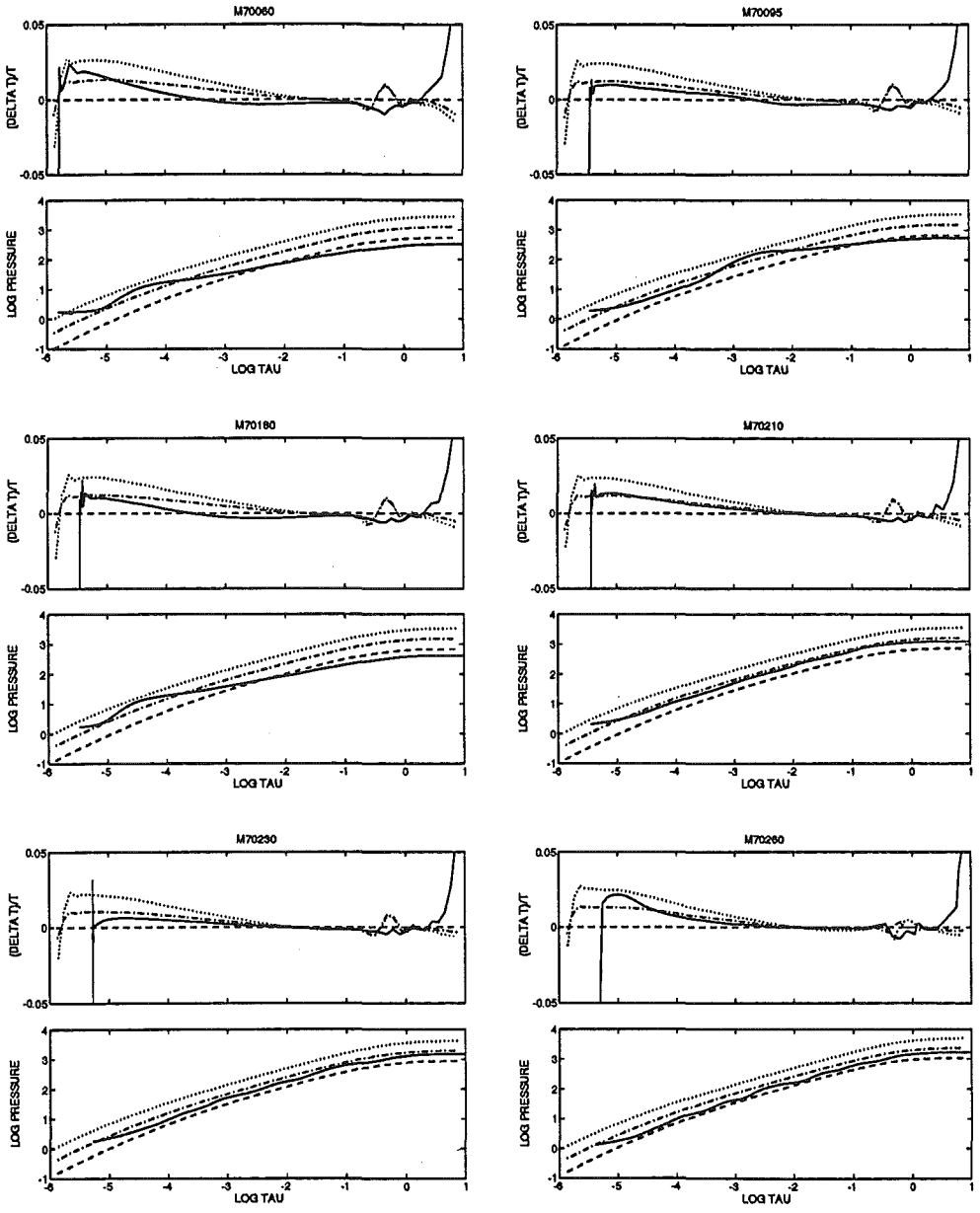

Figure 4.7: Pressure and temperature structures of the converged model atmospheres ———, along with that for static model atmospheres of the same $T_{\rm eff}$ with values of $\log g = 1.0$ - - - -, 1.5 - · - · -, 2.0 ·····. Temperatures are given as relative offsets from the static models with $\log g = 1.0$.

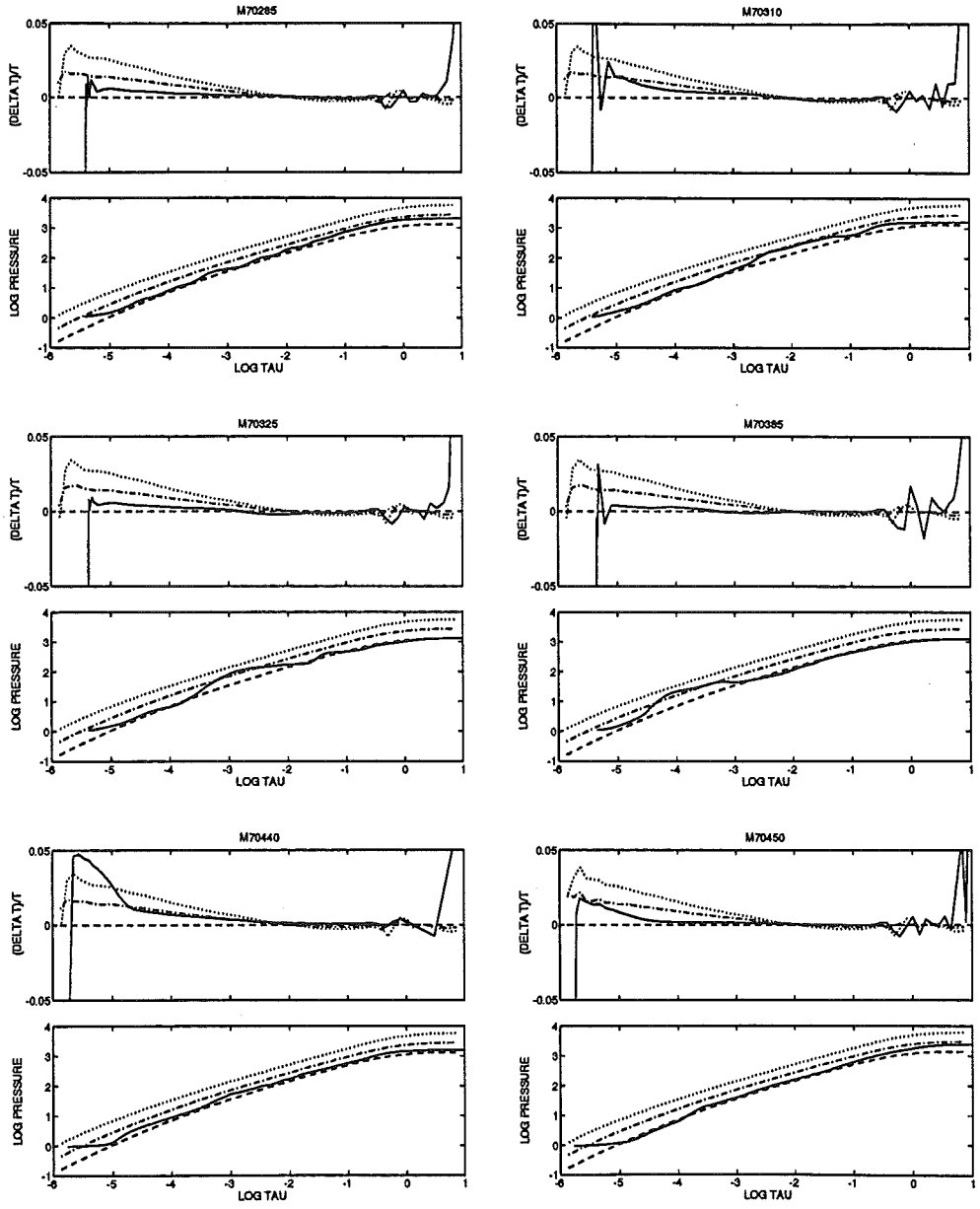

Figure 4.8: Pressure and temperature structures of the converged model atmospheres.

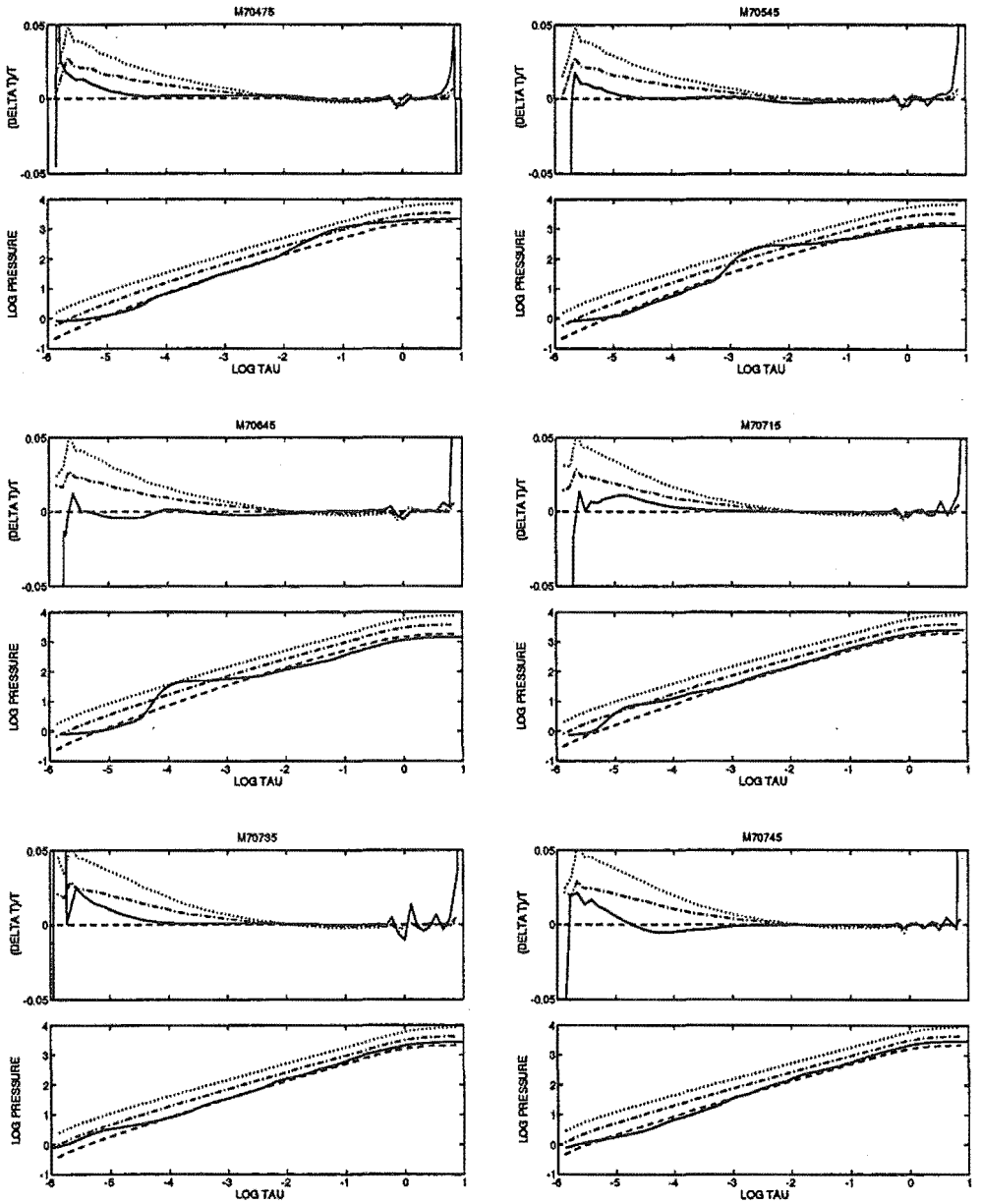

Figure 4.9: Pressure and temperature structures of the converged model atmospheres.

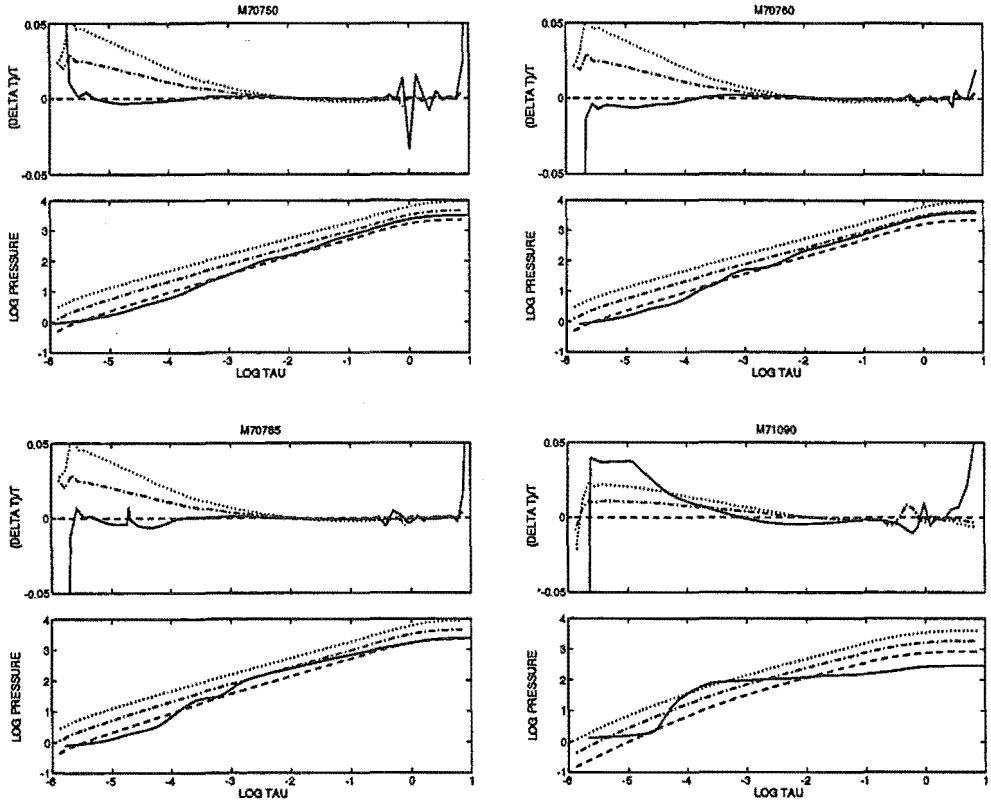

Figure 4.10: Pressure and temperature structures of the converged model atmospheres.

Table 4.1: Phases and effective temperatures of each of the snapshot models.

model	phase	$T_{\rm eff}$	model	phase	$T_{\rm eff}$
70060	0.01770	6220	70450	0.52381	5425
70095	0.06353	6048	70475	0.57382	5208
70180	0.10759	6048	70545	0.61699	5207
70210	0.16368	5994	70645	0.66207	5124
70230	0.20466	5859	70715	0.71112	5029
70260	0.24823	5673	70735	0.75508	4953
70285	0.29225	5492	70745	0.81993	4884
70310	0.35263	5485	70750	0.85945	4850
70325	0.38533	5514	70760	0.90198	4857
70385	0.43320	5518	70785	0.93818	4888
70440	0.48885	5488	71090	0.98490	5875

pressure balance equation,

$$\frac{dP_{total}}{dx} = -g\rho, \tag{4.5}$$

was used only to maintain a *rhox* scale with approximately constant steps in $\tau_{\rm Ross}$, the Rosseland mean optical depth. To allow for hydrodynamical effects, the gravity of the model is replaced in this part of the code by a depth dependent effective gravity, $g_{\rm eff}$, where

$$g_{\rm eff}(x) = g(x) + \frac{\partial^2 x}{\partial t^2}. \tag{4.6}$$

The acceleration in (4.6) was obtained by extracting the velocity of each zone in the hydrodynamic model as a function of time. These velocities were then smoothed and fitted with cubic splines before being differentiated numerically.

In Figs 4.7–4.10 we plot the pressure and temperature structure for each of the converged models as a function of log $\tau_{\rm Ross}$ and compare this with the same curves for static model atmospheres of the same effective temperature, which have been taken from the grid of models described in Kurucz (1992). The temperature structures are given as differences from the corresponding static model with $\log gf = 1.0$. Curves are given for three different values of log g. For many of the models, there is a variation of greater than 1 in log g through the atmosphere.

This result contrasts with that of Keller & Mutschlecner (1970) who found variations in log g of ~ 0.1. They, however, did not use a depth dependent effective gravity for their calculations because the variation in acceleration through the atmosphere of their model at a given phase was apparently much smaller than in our model.

In the following chapter we will use these model atmospheres for calculations of synthetic spectral lines. Parameters derived from these line profiles will then be compared with the observations from Chapter 3 and with static models from Chapter 2.

Chapter 5

Synthetic spectra from a moving atmosphere

5.1 Introduction

In order to calculate synthetic spectra based on dynamic model atmospheres, it is not sufficient to simply apply Doppler shifts to the opacities at each zone of the model corresponding to the velocity of that zone. Indeed, there is an assumption inherent in the matrix method for calculating the mean intensity (Kurucz 1969) that the source function has no angular dependence, which is the case in a static atmosphere. In an atmosphere with a velocity stratification this condition no longer holds.

A generalisation of Kurucz' integral operator method, where the assumption of non-angular dependence of the source function is not required, is derived below. We follow Kurucz (1970) closely for much of this and make reference to equations in that text when appropriate. We will be dealing with fairly moderate velocities, so the formulation of the equations in the observers frame is not too inefficient from a computing point of view.

5.2 Mean intensity

First consider the general moment integral

$$\begin{aligned} M_n(\tau) &= -\frac{1}{2}\int_{-1}^{0}\int_{0}^{\tau} S(t,\mu)e^{-(t-\tau)/\mu}\mu^{n-2}dtd\mu \\ &\quad +\frac{1}{2}\int_{0}^{1}\int_{\tau}^{\infty} S(t,\mu)e^{-(t-\tau)/\mu}\mu^{n-2}dtd\mu, \end{aligned} \tag{5.1}$$

where $S(t,\mu)$ is the source function at optical depth t and angle $\mu = cos(\theta)$, so that $J(\tau) = M_1(\tau), H(\tau) = M_2(\tau), K(\tau) = M_3(\tau)$. Dividing the τ range into N subintervals from 0 to ∞, we have (compare Kurucz 1970, equation 2.50)

$$M_{nl} \equiv M_n(\tau_l) \tag{5.2}$$

$$\begin{aligned} &= -\frac{1}{2}\int_{-1}^{0}\mu^{n-2}\sum_{j=1}^{l-1}\int_{\tau_j}^{\tau_{j+1}} S(t,\mu)e^{-(t-\tau_l)/\mu}dtd\mu \\ &\quad +\frac{1}{2}\int_{0}^{1}\mu^{n-2}\sum_{j=l}^{N}\int_{\tau_j}^{\tau_{j+1}} S(t,\mu)e^{-(t-\tau_l)/\mu}dtd\mu. \end{aligned} \tag{5.3}$$

If we assume that S(t,μ) can be represented by a parabola in the interval (τ_j, τ_{j+1}),

$$S(\mu,t) = \sum_{f=1}^{3} t^{f-1}\sum_{i=1}^{N} C_{jfi}S_i(\mu) \tag{5.4}$$

(where the C_{jfi} are Kurucz' parabolic interpolation coefficients), the jth term in the sum becomes

$$M_{nlj} = \begin{cases} -\frac{1}{2}\int_{-1}^{0}\mu^{n-2}\int_{\tau_j}^{\tau_{j+1}} e^{-(t-\tau_l)/\mu}\sum_{f=1}^{3} t^{f-1}\sum_{i=1}^{N} C_{jfi}S_i(\mu)\,dt\,d\mu & ,j < l \\ \frac{1}{2}\int_{0}^{1}\mu^{n-2}\int_{\tau_j}^{\tau_{j+1}} e^{-(t-\tau_l)/\mu}\sum_{f=1}^{3} t^{f-1}\sum_{i=1}^{N} C_{jfi}S_i(\mu)\,dt\,d\mu & ,j \geq l. \end{cases} \tag{5.5}$$

If we divide μ into W subintervals from (-1,1),where $\mu_{W_0} = 0$, this becomes

$$M_{nlj} = \begin{cases} -\frac{1}{2}\sum_{p=1}^{W_0-1}\int_{\mu_p}^{\mu_{p+1}}\mu^{n-2}\int_{\tau_j}^{\tau_{j+1}} e^{-(t-\tau_l)/\mu}\sum_{f=1}^{3} t^{f-1} \\ \times\sum_{i=1}^{N} C_{jfi}S_i(\mu)\,dt\,d\mu & ,j < l \\ \frac{1}{2}\sum_{p=W_0}^{W}\int_{\mu_p}^{\mu_{p+1}}\mu^{n-2}\int_{\tau_j}^{\tau_{j+1}} e^{-(t-\tau_l)/\mu}\sum_{f=1}^{3} t^{f-1} \\ \times\sum_{i=1}^{N} C_{jfi}S_i(\mu)\,dt\,d\mu & ,j \geq l. \end{cases} \tag{5.6}$$

We assume that $S_i(\mu)$ can be represented by a parabola in the interval (μ_p, μ_{p+1}),

$$S_i(\mu) = \sum_{g=1}^{3}\mu^{g-1}\sum_{q=1}^{W} A_{pgq}S_{iq}, \tag{5.7}$$

where the A_{pgq} are parabolic interpolation coefficients for μ.Thus

$$M_{nlj} = \sum_{p=1}^{W} M_{nljp}, \tag{5.8}$$

where

$$M_{nljp} = \sum_{g=1}^{3}\sum_{f=1}^{3} \gamma_{nljpgf} \sum_{i=1}^{N}\sum_{q=1}^{W} A_{pgq} C_{jfi} S_{iq} \tag{5.9}$$

(the analogue of Kurucz 1970 equation 2.53), and

$$\gamma_{nljpgf} \equiv \begin{cases} \frac{1}{2} sign(\tau_j - \tau_l) \int_{\mu_p}^{\mu_{p+1}} \mu^{n+g-3} \int_{\tau_j}^{\tau_{j+1}} t^{f-1} e^{-(t-\tau_l)/\mu}\, dt\, d\mu \\ \qquad\qquad , sign(\tau_j - \tau_l) = sign(\mu_p) \\ 0 \qquad\qquad , sign(\tau_j - \tau_l) \neq sign(\mu_p). \end{cases} \tag{5.10}$$

We can perform the integrations over t and μ so that

$$\gamma_{nljpgf} = \begin{cases} -\frac{1}{2} sign(\tau_j - \tau_l)\{\beta_{l(j+1)p}(g) - \beta_{ljp}(g)\} & , f = 1 \\ -\frac{1}{2} sign(\tau_j - \tau_l)\{\beta_{l(j+1)p}(g+1) - \beta_{ljp}(g+1) & \\ +\tau_{j+1}\beta_{l(j+1)p}(g) - \tau_j \beta_{ljp}(g)\} & , f = 2 \\ -\frac{1}{2} sign(\tau_j - \tau_l)\{2\beta_{l(j+1)p}(g+2) - 2\beta_{ljp}(g+2) & \\ +2\tau_{j+1}\beta_{l(j+1)p}(g+1) - 2\tau_j \beta_{ljp}(g+1) & \\ +\tau_{j+1}^2\beta_{l(j+1)p}(g) - \tau_j^2 \beta_{ljp}(g)\} & , f = 3, \end{cases} \tag{5.11}$$

where we define

$$\beta_{ljp}(b) \equiv \begin{cases} \frac{1}{b+1}(\mu_{p+1}^b - \mu_p^b) & , \tau_j = \tau_l \\ -\sum_{a=1}^{b} \frac{(\tau_l - \tau_j)^{a-1}}{b(b-1)\ldots(b+1-a)} (\mu_p^{b+1-a} e^{-\frac{\tau_j - \tau_l}{\mu_p}} - \mu_{p+1}^{b+1-a} e^{-\frac{\tau_j - \tau_l}{\mu_{p+1}}}) & \\ +\frac{1}{b!}(\tau_l - \tau_j)^b (E_1(\frac{\tau_j - \tau_l}{\mu_{p+1}}) - E_1(\frac{\tau_j - \tau_l}{\mu_p})) & , \tau_j \neq \tau_l \end{cases} \tag{5.12}$$

and where E_1 is the exponential integral. Collecting terms,

$$M_{nlj} = \sum_{p=1}^{W}\sum_{g=1}^{3}\sum_{f=1}^{3} \gamma_{nljpgf} \sum_{i=1}^{N}\sum_{q=1}^{W} A_{pgq} C_{jfi} S_{iq}, \tag{5.13}$$

so that, interchanging p with q and i with j,

$$M_{nl} = \sum_{j=1}^{N}\sum_{p=1}^{W}\sum_{i=1}^{N}\sum_{g=1}^{3}\sum_{f=1}^{3}\sum_{q=1}^{W}\gamma_{nliqgf}A_{qgp}C_{ifj}S_{jp}. \tag{5.14}$$

This is now a matrix equation for M_{nl},

$$M_{nl} = \sum_{j=1}^{N}\sum_{p=1}^{W}\Psi_{nljp}S_{jp}, \tag{5.15}$$

where (compare with Kurucz (1970) equation 2.60)

$$\Psi_{nljp} = \sum_{i=1}^{N}\sum_{g=1}^{3}\sum_{f=1}^{3}\sum_{q=1}^{W}\gamma_{nliqgf}A_{qgp}C_{ifj}. \tag{5.16}$$

For example

$$J_l = \sum_{j=1}^{N}\sum_{p=1}^{W}\Omega_{ljp}S_{jp}, \tag{5.17}$$

where

$$\Omega_{ljp} \equiv \Psi_{1ljp}. \tag{5.18}$$

For computational efficiency, this can be written in the form

$$J_l = \sum_{r=1}^{NP}\Omega_{lr}S_r. \tag{5.19}$$

5.3 Source function

The source function can be defined by the integral equation

$$S_{lq} = (1-\alpha_{lq})\overline{S}_{lq} + \alpha_{lq}J_l, \tag{5.20}$$

where α is defined as the ratio of scattering to total opacity. $\overline{S}$ is the absorption coefficient multiplied by the scattering coefficient for each opacity source, which are then summed and divided by the total opacity. An iterative procedure (similar to Kurucz 1970, Section 2.7),

$$S^{new} = S^{old} + \Delta S \tag{5.21}$$

can be used for determining the source function, where

$$\Delta S_{ip} \approx -\frac{\sum_{l=1}^{N}\sum_{q=1}^{W}(\delta_{il}\delta_{pq} - \alpha_{ip}\Omega_{ilq})S_{lq} - (1-\alpha_{ip})\overline{S}_{ip}}{1-\alpha_{ip}\Omega_{iip}} \tag{5.22}$$

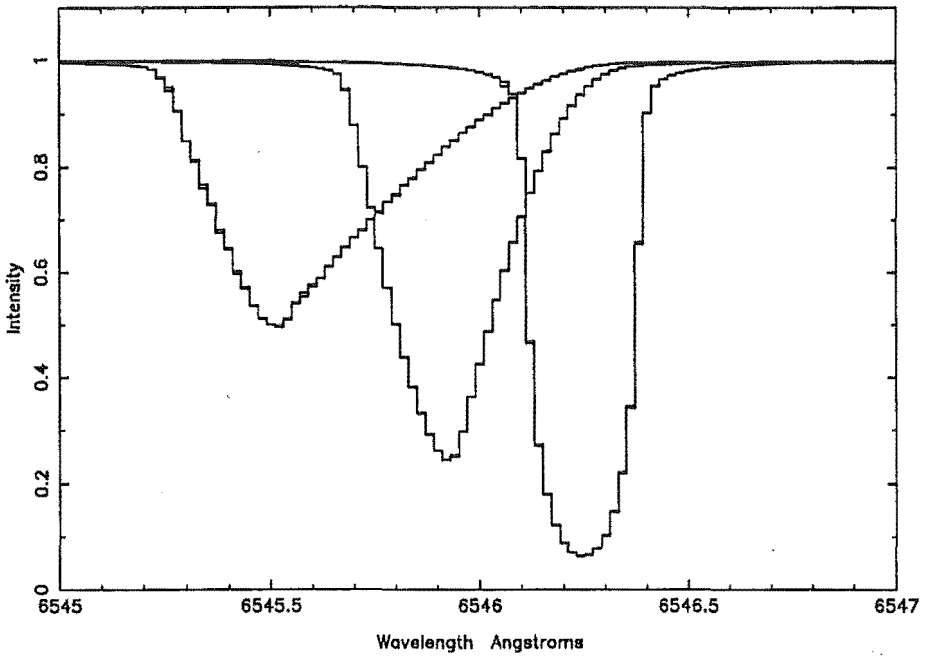

Figure 5.1: Comparison of flux profiles calculated using a static model and Doppler shift with those from a dynamic model for constant pulsational velocities of 0, 20 and 40 km s^{-1}.

if $(1 - \alpha\Omega)$ is almost diagonal. In practice this condition is true only when linear rather than parabolic coefficients are used for the optical depth interpolation. The use of such coefficients does not seem to introduce any inaccuracies for the lines we have calculated. We have used a grid with 43 depth points and 41 angular points. An angular resolution $\Delta\mu$ imposes a spectral resolution

$$\Delta\lambda = \frac{\Delta\mu V_{\max}\lambda_0}{c}, \tag{5.23}$$

where $V_{\max}$ is the maximum pulsational velocity. Thus, for a maximum velocity of say 50 km s^{-1}, we have a maximum resolution $\Delta\lambda = 0.05$ Å for this number of angular points. Due to the size of the coefficient matrix, Ω, we do not tabulate the coefficients here. The code used to generate the coefficients is given in appendix C.

5.4 Tests of the algorithm

As a check on the accuracy of the method, synthetic spectra generated as described above and for a constant velocity atmosphere were compared with those which had been calculated by the static atmosphere method and then Doppler

shifted. The results were in excellent agreement. In Fig. 5.1 we show sample unbroadened synthetic flux profiles calculated for the Fe I 6546 Å line for a standard solar abundance Kurucz model atmosphere with $T_{\rm eff}$ = 5000 K, log g = 1.0 and ξ = 2 km s^{-1}. Profiles calculated by each of the two methods with pulsation velocities of 0, 20 and 40 km s^{-1}are shown. Differences between the two sets of profiles are barely discernible.

5.5 Synthetic spectra from the dynamic models

A series of synthetic spectra based on the converged model atmospheres from Chapter 4 were calculated using the algorithm described above. We have used the 6546 Å Fe I line so that we can draw direct comparisons with both the observations described in Chapter 3 and the Doppler-shifted, static atmosphere calculations of Chapter 2. Three artificial gf values were used to simulate lines of different strength. As in the calculations in Chapter 2, the specific intensities over the surface of each model were convolved with the macroturbulent broadening function (2.3) with $\zeta_R = \zeta_T$ = 10 km s^{-1}. After disc integration, the resultant profiles were convolved with a Gaussian of half-width 0.1 Å to simulate instrumental broadening. The final flux profiles are shown in Figs 5.2, 5.3 and 5.4.

5.6 Radial velocities and asymmetries

The bisectors of each of these synthetic spectral lines were calculated and the radial velocity curves are shown in Figs 5.5, 5.6 and 5.7.

The asymmetry of each of the lines is plotted in Figs 5.8, 5.9 and 5.10 against γ, the ratio of pulsation velocity to half-width at half-height of the line, along with the theoretical relation (2.11). The 'pulsational' velocity was determined, as it would be empirically, by multiplying the radial velocity measured from the bisector by the projection factors P(0.5) = 1.41 (2.9) or P(0.9) = 1.38 (2.10). It should be noted that the resulting diagrams are insensitive to which particular bisector height is used for this.

The asymmetry of the synthetic line profiles agrees well with the curve we obtained from constant velocity calculations in Chapter 2 for phases of negative γ (negative radial velocity). There is some significant negative asymmetry present at small positive γ, which corresponds to the bump phases on the radial velocity

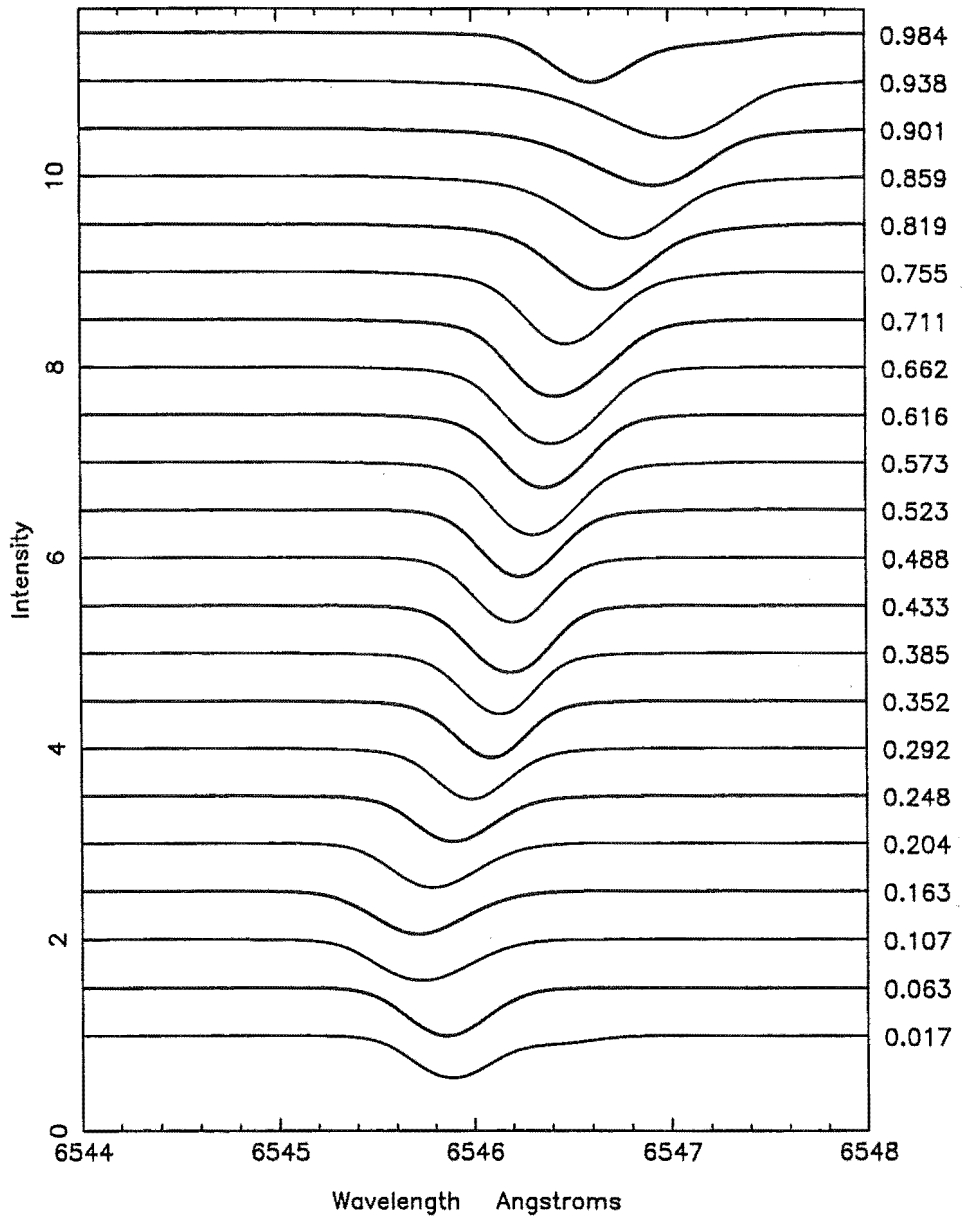

Figure 5.2: Synthetic line profiles calculated with $\log gf = 0$ for each of the 22 model atmospheres in phase order from bottom to top.

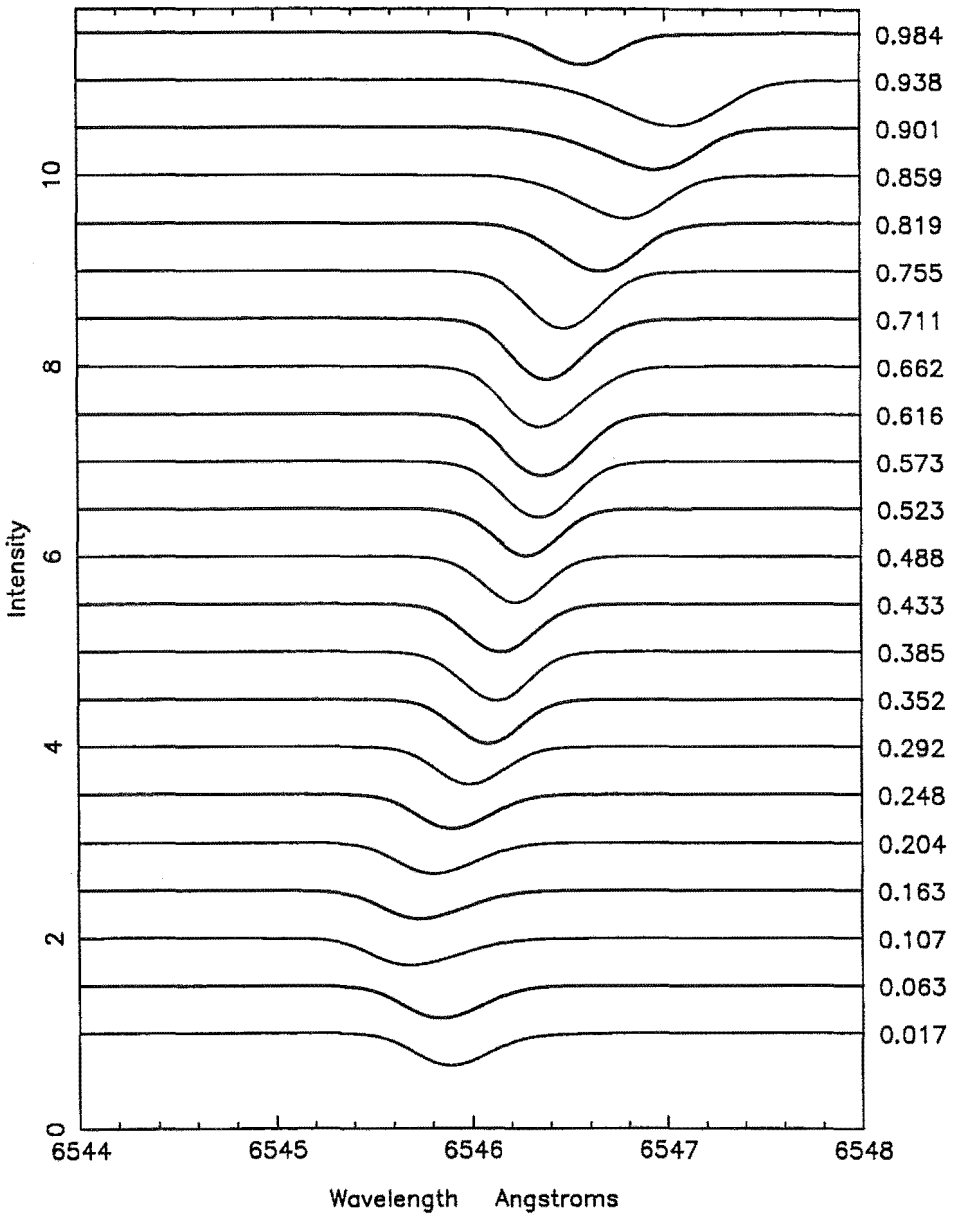

Figure 5.3: As for Fig. 5.2 with log gf = -1.

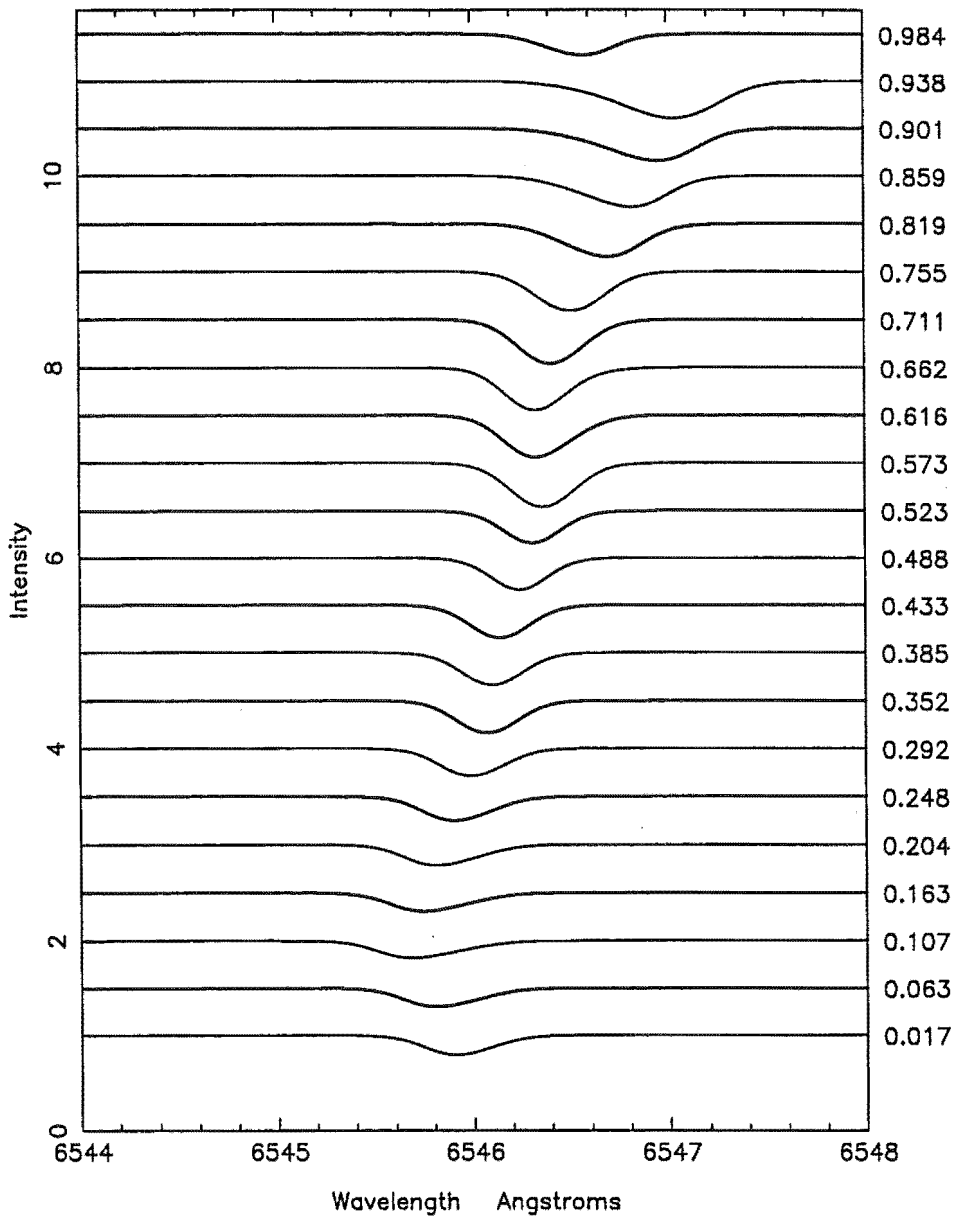

Figure 5.4: As for Fig. 5.2 with log gf = -2.

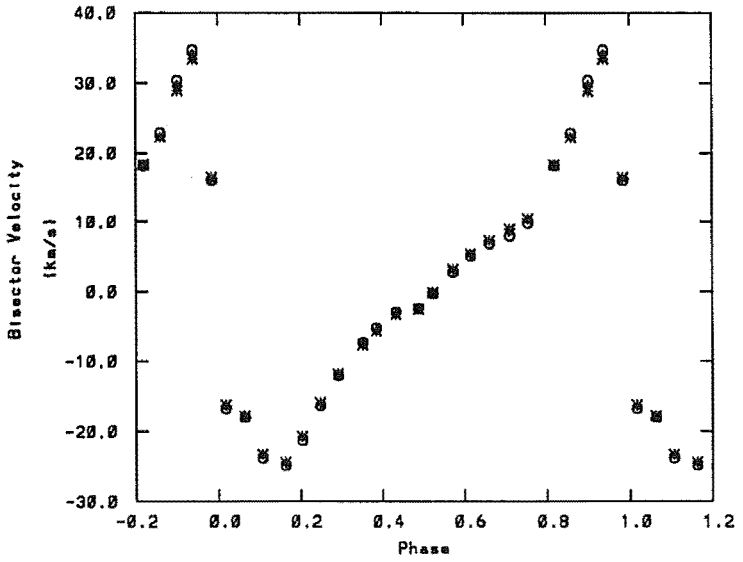

Figure 5.5: Radial velocity of the synthetic 6546 Å line with log $gf = 0$.

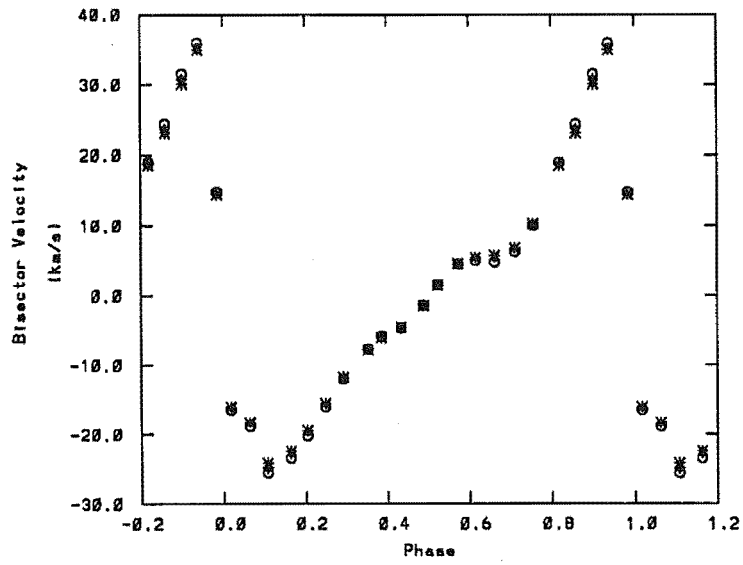

Figure 5.6: As in Fig. 5.5 for log $gf = -1$.

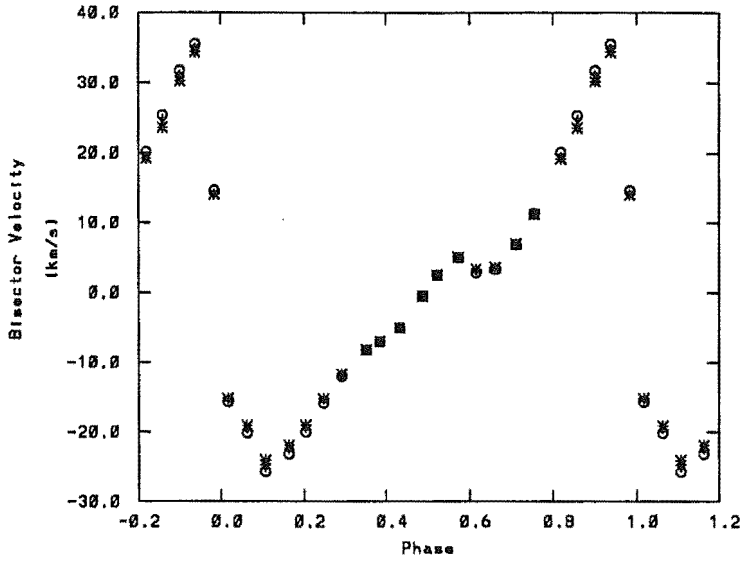

Figure 5.7: As in Fig. 5.5 for gf = -2.

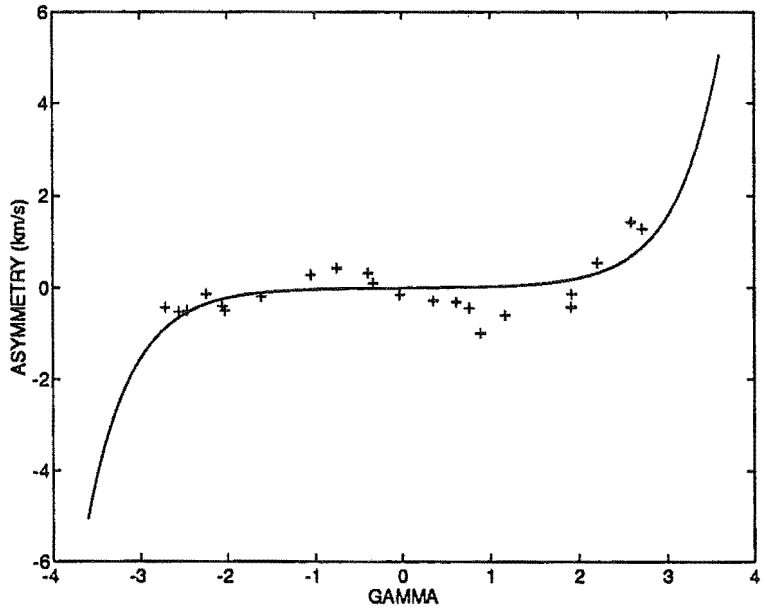

Figure 5.8: Asymmetry versus γ of the synthetic 6546 Å line with log $gf = 0$.

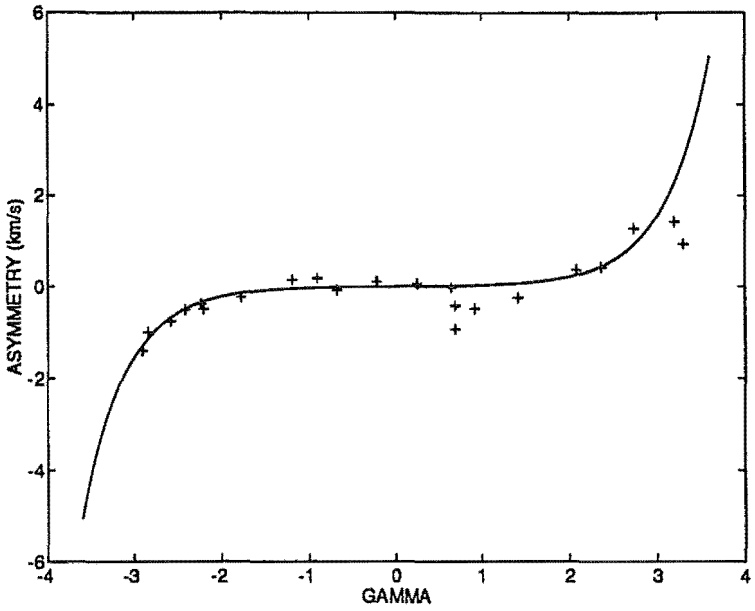

Figure 5.9: As in Fig. 5.8 for log gf = -1.

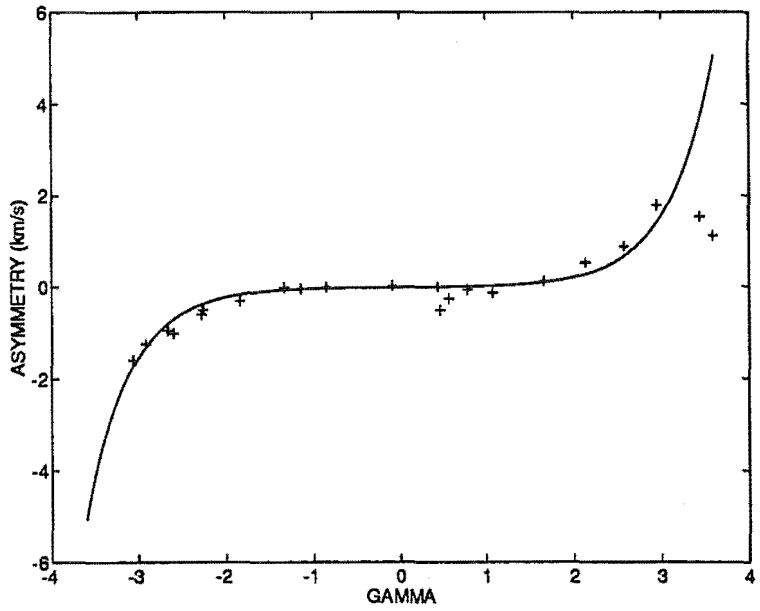

Figure 5.10: As in Fig. 5.8 for log gf = -2.

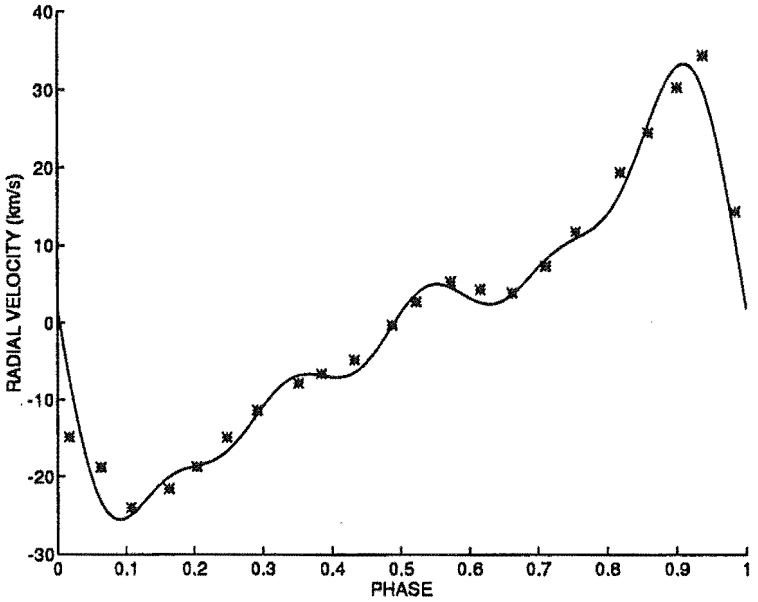

Figure 5.11: Fifth order Fourier series fit to the radial velocities at line depth 0.5 from the profiles calculated with $\log gf = -2$.

curves. This is observed to some extent in the Cepheids W Sgr, β Dor, S Nor and S Mus, although the asymmetry in these cases is in the opposite direction because the bumps occur at negative radial velocity (after subtraction of the γ-velocity) phases. At phases of maximum radial velocity, corresponding to the largest positive values of γ, the asymmetry is smaller than the static model curve except for the strongest set of lines we have calculated.

This shows that the velocity gradients present in the model atmospheres are having a measurable effect on line formation. We will discuss the formation of asymmetric spectral lines in more detail in Chapter 6.

5.7 Acceleration and radius curves

Following the method of analysis used for the observations in Chapter 3, we are now in a position to derive acceleration and radius curves from the radial velocities. Using the methods discussed in Chapter 3 we have made a Fourier series fit to the radial velocity curve at line depth 0.5 for the weakest set of line profiles (Fig. 5.11). It is this weakest set of lines with equivalent widths in the range 90-250 mÅ which most closely matches the strength of the observed lines (see Appendix B). Due to the abruptness of the change from positive to negative

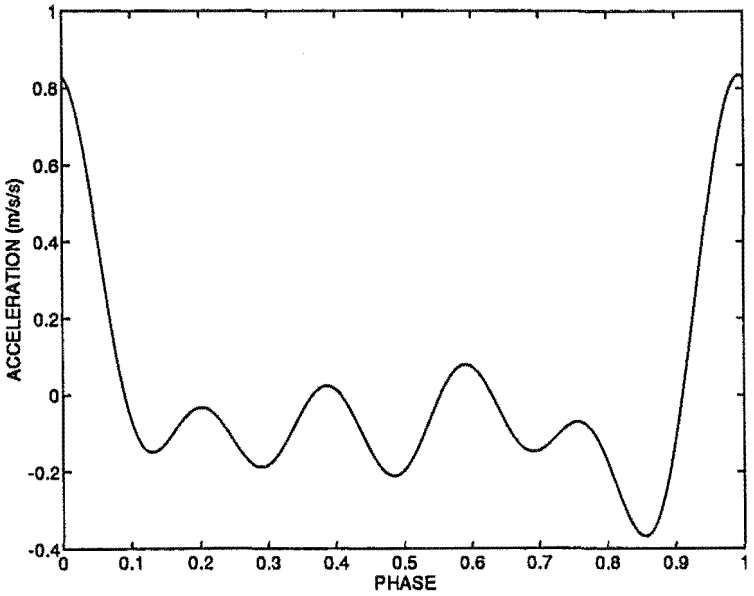

Figure 5.12: Acceleration curve for log gf = -2.

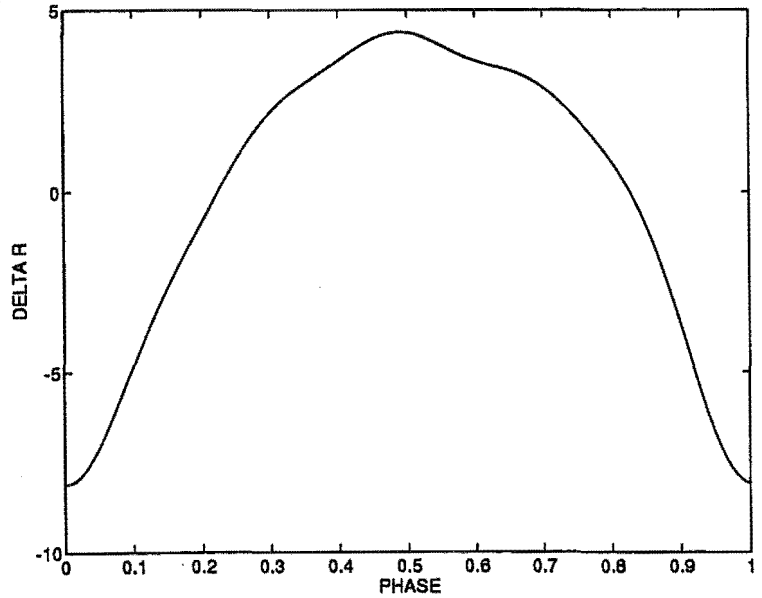

Figure 5.13: Radius curve for log gf = -2 in units of $R_\odot$.

radial velocity (see Fig. 5.7), the fit had rather large residuals, $\sigma \sim 3.6$ km s^{-1}. This is similar to the difficulties encountered when applying this procedure to U Car (see Chapter 3, Section 3.4). The γ-velocity obtained using this method is (-0.13±0.78) km s^{-1}.

The acceleration and radius curves obtained from differentiation and integration of the fit for $\log gf = -2$ are shown in Figs 5.12 and 5.13. The acceleration curve is of more or less similar shape to those of all the observed Cepheids (Chapter 3) with the exception of Y Oph. Only W Sgr has an acceleration amplitude almost as high as 0.8 m s^{-2}. The radius curve of the model is qualitatively similar to those of W Sgr and U Car with an amplitude some way between them. The radius curves of these stars and the model are different from those of the other Cepheids in that they are not centred on zero, i.e. the mean radius is much closer to the radius maximum than the radius minimum. In summary, the model has features similar to many of the observations rather than being a close match to any particular object.

In the following chapter we will compare the radial velocities from the synthetic spectral lines we have calculated with the actual velocities in the model stellar atmospheres.

Chapter 6

Analysis

In Chapter 5 we have calculated spectral lines from the dynamic model atmospheres and derived radius and acceleration curves from them. We now move on to a more in-depth analysis of the relationship between the velocity fields in the model stellar atmospheres and their effect on spectral line profiles.

6.1 Contribution functions

To investigate how the velocity of each zone in a model atmosphere affects the line profile, we need to consider the contribution of each zone to the spectral line. Magain (1986) derives the contribution function

$$C_R(x) = \frac{ln10}{\mu}\tau_0\frac{\kappa_l}{\kappa_0}\left(1-\frac{S_l}{I_c}\right)e^{-\tau_R/\mu}, \tag{6.1}$$

to the *relative* depression in the surface intensity in the $x = \log_{10}\tau_0$ scale at a given wavelength and angle, $\mu = \cos\theta$. τ_0 and κ_0 are the optical depth and absorption coefficient at some reference wavelength and κ_l is the line absorption coefficient. S_l is the line source function defined in terms of the continuous absorption coefficient, κ_c, the continuum source function, S_c, the line absorption coefficient and the total source function, S_t, by

$$S_t = \frac{\kappa_c S_c + \kappa_l S_l}{\kappa_c + \kappa_l}. \tag{6.2}$$

I_c is the continuous intensity and τ_R is the effective optical depth, defined by the effective absorption coefficient

$$\kappa_R = \kappa_l + \kappa_c\frac{S_c}{I_c}. \tag{6.3}$$

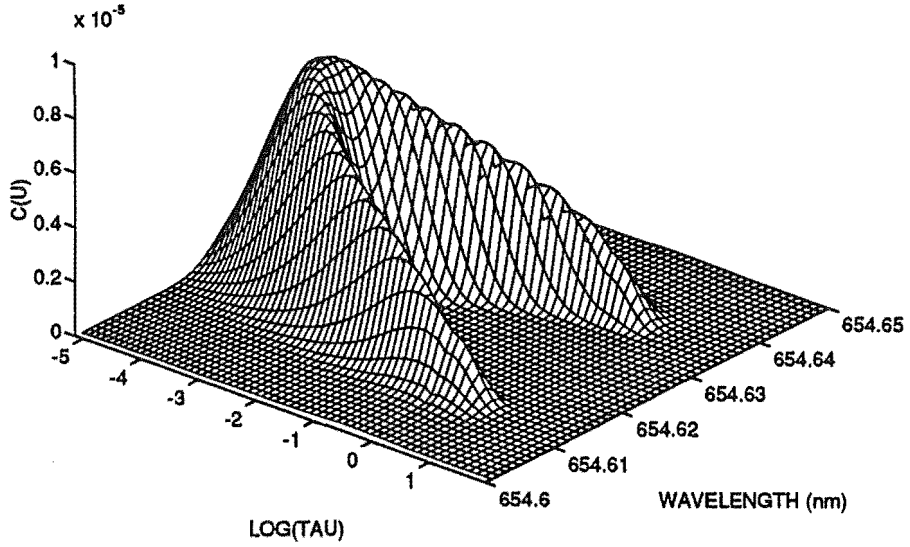

Figure 6.1: Flux contribution function for the Fe I 6546 Å line, with log gf = -1 and for a standard static solar abundance Kurucz model atmosphere with $T_{\rm eff}$ = 5000 K, log g = 1.0 and ξ = 2 km s^{-1}.

The difficulties in deriving a contribution function to the *relative* depression in the *flux* have been pointed out by Achmad, de Jager & Nieuwenhuijzen (1991). To consider the contribution of each zone to the depression in the flux, we follow Magain's method, but derive an expression for the *absolute* depression in the surface intensity, Q(0), where

$$Q = I_c - I_l. \tag{6.4}$$

By expressing the intensity depression in these absolute terms, we can add together contributions from different parts of the stellar disc to obtain the contribution function to the absolute flux. We begin by combining the transfer equations for I_c and I_l,

$$\frac{\mu}{\rho}\frac{dI_c}{dz} = -\kappa_c(I_c - S_c) \tag{6.5}$$

$$\frac{\mu}{\rho}\frac{dI_l}{dz} = -(\kappa_c + \kappa_l)(I_l - S_t), \tag{6.6}$$

and carefully separate the known and unknown variables to obtain the transfer equation for Q,

$$\frac{\mu}{\rho}\frac{dQ}{dz} = -(\kappa_c + \kappa_l)(Q - S_Q), \tag{6.7}$$

where

$$S_Q = \frac{\kappa_l}{\kappa_c + \kappa_l}(I_c - S_l). \tag{6.8}$$

The formal solution for the absolute depression in the surface intensity can be written

$$Q(0) = \int_0^\infty S_Q e^{-\tau/\mu} d\tau/\mu, \tag{6.9}$$

and the absolute depression in the flux

$$U = \int_0^1 \mu Q(0) d\mu \tag{6.10}$$

$$= \int_0^\infty \int_0^1 S_Q e^{-\tau/\mu} d\mu d\tau. \tag{6.11}$$

We can identify the contribution function to the flux depression

$$C_U(\tau_0) = \int_0^1 S_Q e^{-\tau/\mu} d\mu \tag{6.12}$$

$$= \int_0^1 \frac{\kappa_l}{\kappa_c + \kappa_l}(I_c - S_l) e^{-\tau/\mu} d\mu, \tag{6.13}$$

or in the log τ_0 scale,

$$C_U(x) = \frac{(ln10)\tau_0}{\kappa_0} \int_0^1 \kappa_l (I_c - S_l) e^{-\tau/\mu} d\mu. \tag{6.14}$$

If a net contribution function for the whole spectral line is required, this function can be integrated with respect to wavelength. However, we are more interested in how this function behaves with changes in wavelength. There are several different ways in which the information contained in the flux contribution function can be displayed. In Fig. 6.1 we use a three dimensional mesh to show the flux contribution as a function of optical depth and wavelength for the zero velocity line used as a test in Fig. 5.1.

For the non-static models, we wish to compare the flux contribution functions with the actual velocity field present in the model atmosphere. We are not particularly interested in the actual value of the contribution function but rather the location of the peak in optical depth and wavelength space. The most informative way to do this comparison is to display the flux contribution as a series of contours in what we call the 'flux contribution contour' diagram. The contours represent loci of constant height (constant values of the contribution function, C) in Fig. 6.1.

As an example (Fig. 6.2), we use the three constant velocity test profiles described in Section 5.4, Fig. 5.1. To aid comparison with an atmospheric velocity field, the wavelength scale has been converted to velocity units. The atmospheric velocity is shown as a dashed line and has been divided by a projection factor of 1.2, which is roughly appropriate for an unbroadened spectral line. We can see that a static atmosphere gives characteristic V-shaped contours, the wings of the spectral line being formed at deeper atmospheric layers than the core. A constant velocity field shifts and distorts the contours. The centre of each successively higher contour is shifted in velocity relative to the previous contour, tending to push the contours up against the maximum velocity edge. In other words, the contours are not concentric. It is this stacking of the contours against one edge, with larger lobes on the other edge, which is the signature of spectral line asymmetry in these diagrams. The fringing apparent in the diagram for V = 40 km s^{-1} is a numerical artifact and should be ignored.

An interesting point to note is that in the presence of a constant velocity field, the trailing (least shifted) wing of the spectral line is now no longer formed at deep atmospheric layers. This is because the absorption at these wavelengths is now predominantly coming from the stellar limb where the line of sight velocity is close to zero. The line of sight optical depth of a given spherical shell is much greater at the limb than at the centre of disc, so the spectral line forms closer to

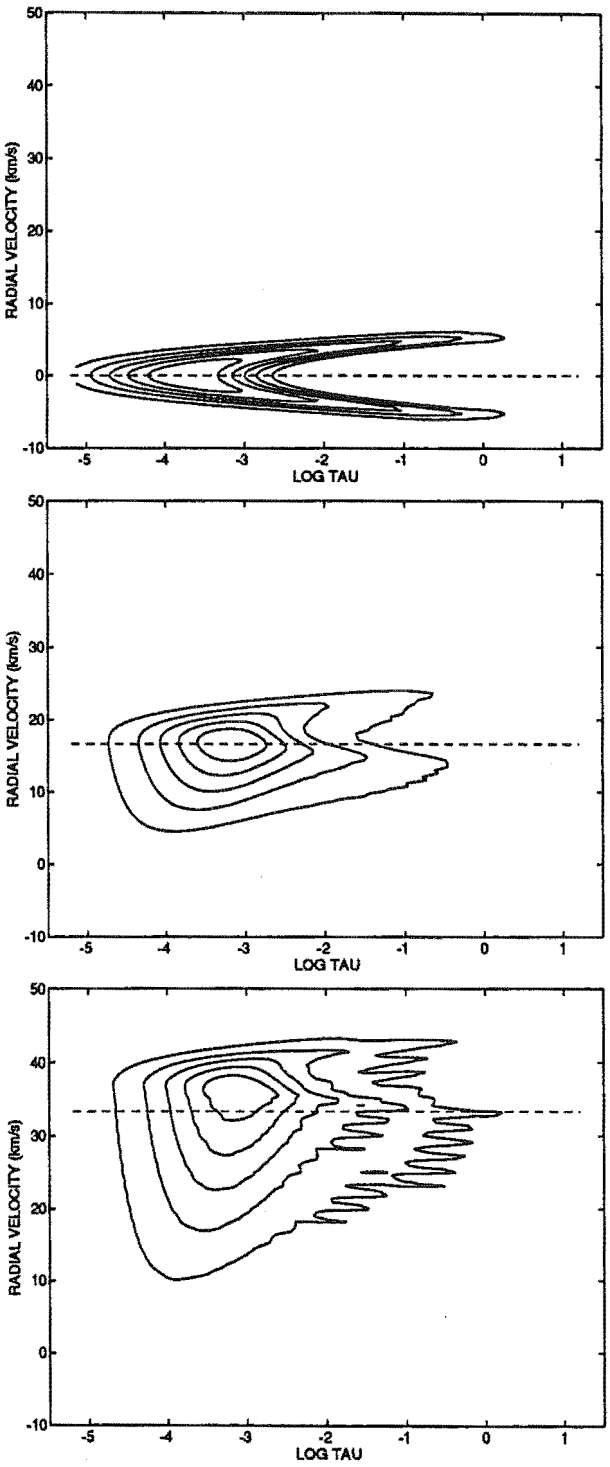

Figure 6.2: Flux contribution contour diagrams for the Fe I 6546 Å line with log gf = -1 for a standard solar abundance Kurucz model atmosphere with $T_{\rm eff}$ = 5000 K, log g = 1.0 and ξ = 2 km s^{-1}. Atmospheric velocities, V, divided by a projection factor of 1.2 (appropriate for unbroadened profiles) are shown as dashed lines. From top to bottom, V = 0, 20, 40 km s^{-1}. The fringing apparent in the bottom diagram is a numerical artifact and should be ignored.

the stellar surface.

In Figs 6.3 - 6.24 we show the flux contribution functions for each of the three spectral lines previously calculated for each of the snapshot model atmospheres. The velocity divided by 1.2 is again shown as a dashed line. In most cases the correlation between the atmospheric velocity and the centre of absorption is good, with the contours tending to follow the velocity line. The relationship tends to worsen as line strength is increased.

An interesting phenomenon which is revealed by these diagrams is the presence of spatially separated absorption centres. These are more prevalent in the stronger lines but still present at certain phases in the weak lines. For the weak lines, multiple absorption features are readily apparent in the models M70325 (Fig. 6.11) and M70475 (Fig. 6.15) which corresponds to phases 0.39 and 0.57 respectively. Only the outermost of each pair of absorption centres corresponds to the projected atmospheric velocity at that depth. Comparing these diagrams with those at adjacent phases, we can confirm that it is the innermost absorption centre which is additional to that expected. The presence of multiple absorption centres is due to the velocity field in the atmosphere, in particular the presence of a velocity gradient throughout the line forming region. The models we have calculated do not continue to show this behaviour when their velocity fields are set to constant values. To understand the mechanism which results in multiple centres, we need first to realise that if a constant, non-zero velocity field is present in a stellar atmosphere, the amount by which the absorption is Doppler-shifted away from the rest wavelength of the line varies across the stellar disc. This is because of geometric projection. The peak magnitude of the contribution function can then be substantially less than if no velocity was present.

In the model M70475 (Fig. 6.15) for example, the velocity near $\log\tau \sim -2.5$ (the formation depth of the core of an unshifted line) is sufficient to move what would be the line core by ~ 10 km s^{-1} in wavelength space. The projection effect means that this shift is not the same across the stellar disc and the peak magnitude of the contribution function in the shifted 'core' is much reduced. Interior to this, near $\log\tau \sim -1$, the projected velocity is close to zero (~ 3 km s^{-1}) and there is little differential Doppler shift over the stellar disc. The blue (negative radial velocity) wing of the spectral line will be formed as in the zero velocity case and, because of the lack of a differential Doppler shift across the stellar disc, the flux contribution is actually greater here than at the 'core' depth. The red

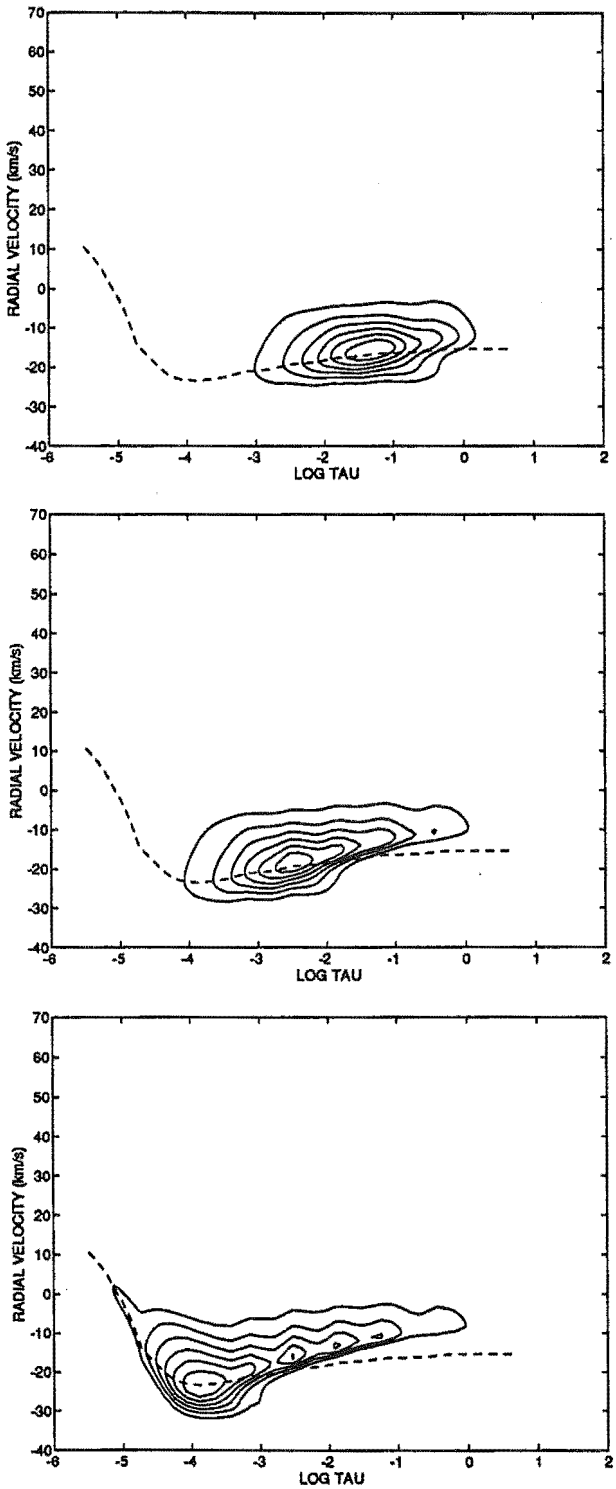

Figure 6.3: Flux contribution functions plotted as contours against log continuum optical depth and $\Delta V = c\Delta\lambda/\lambda$ for model M70060 and, from top to bottom, log gf = -2, -1, 0. Also shown as a dashed line is the atmospheric velocity field divided by 1.2, a projection factor appropriate for unbroadened lines.

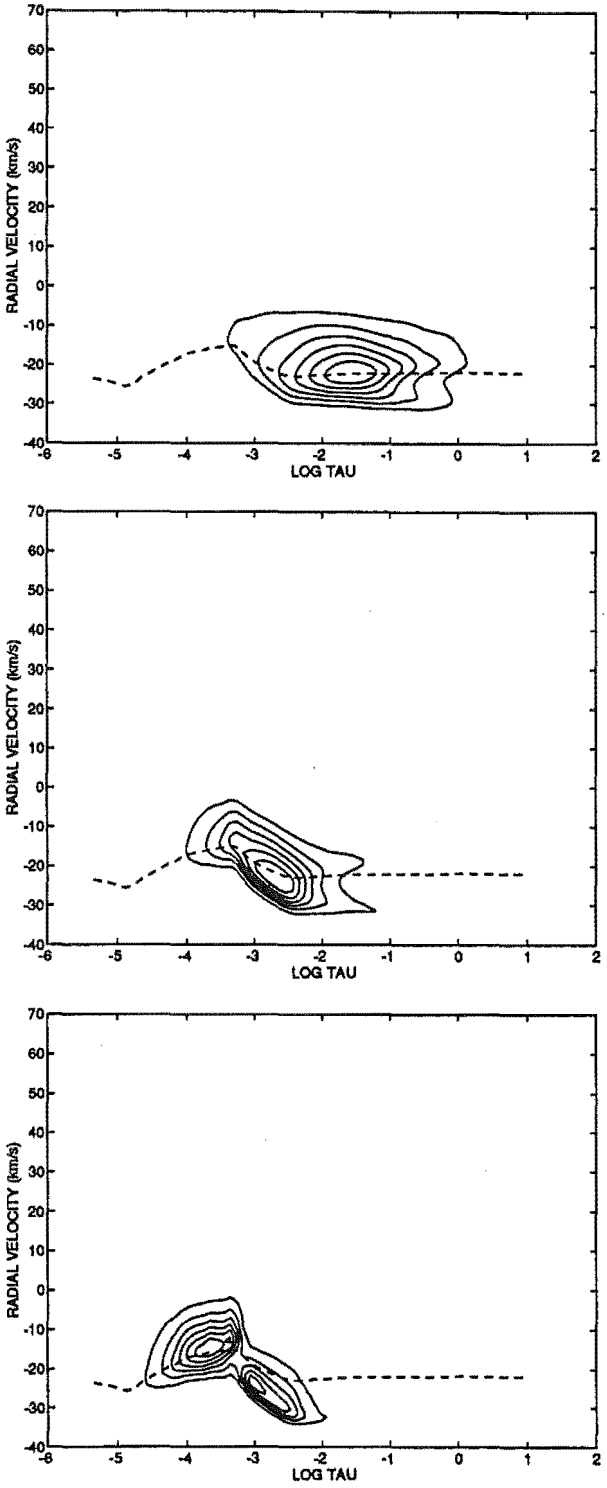

Figure 6.4: As in Fig. 6.3 for model M70095.

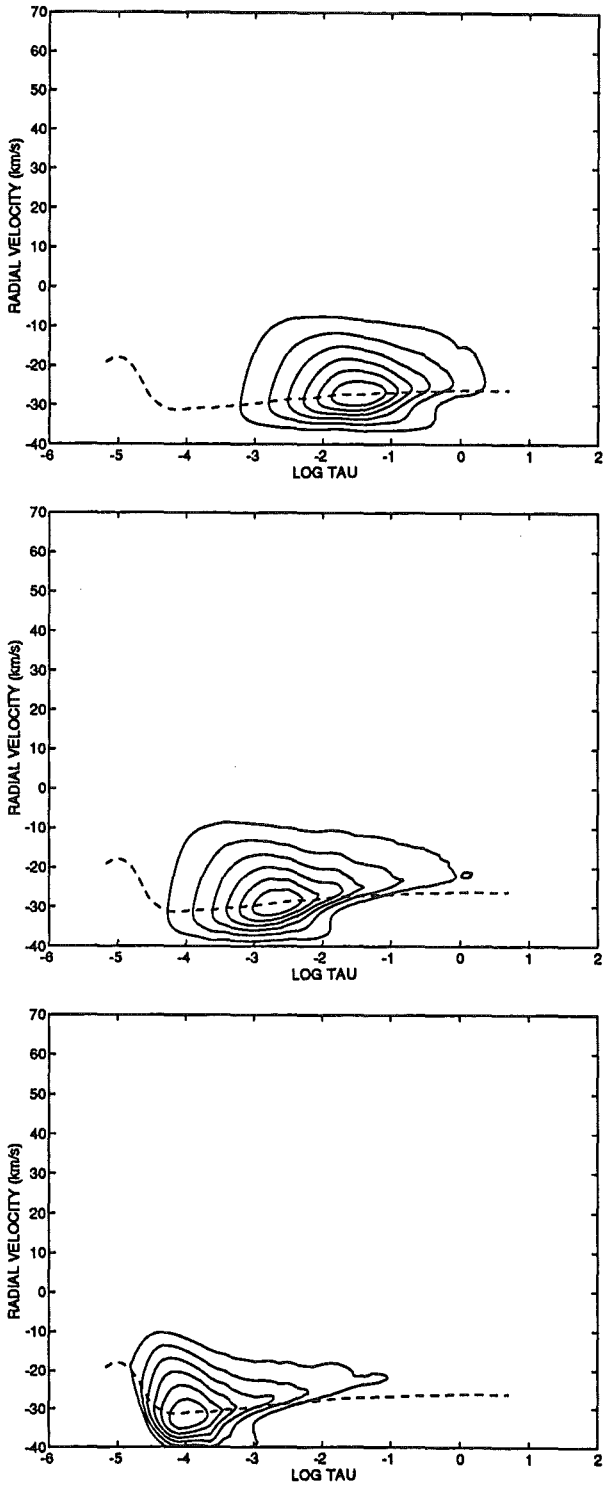

Figure 6.5: As in Fig. 6.3 for model M70180.

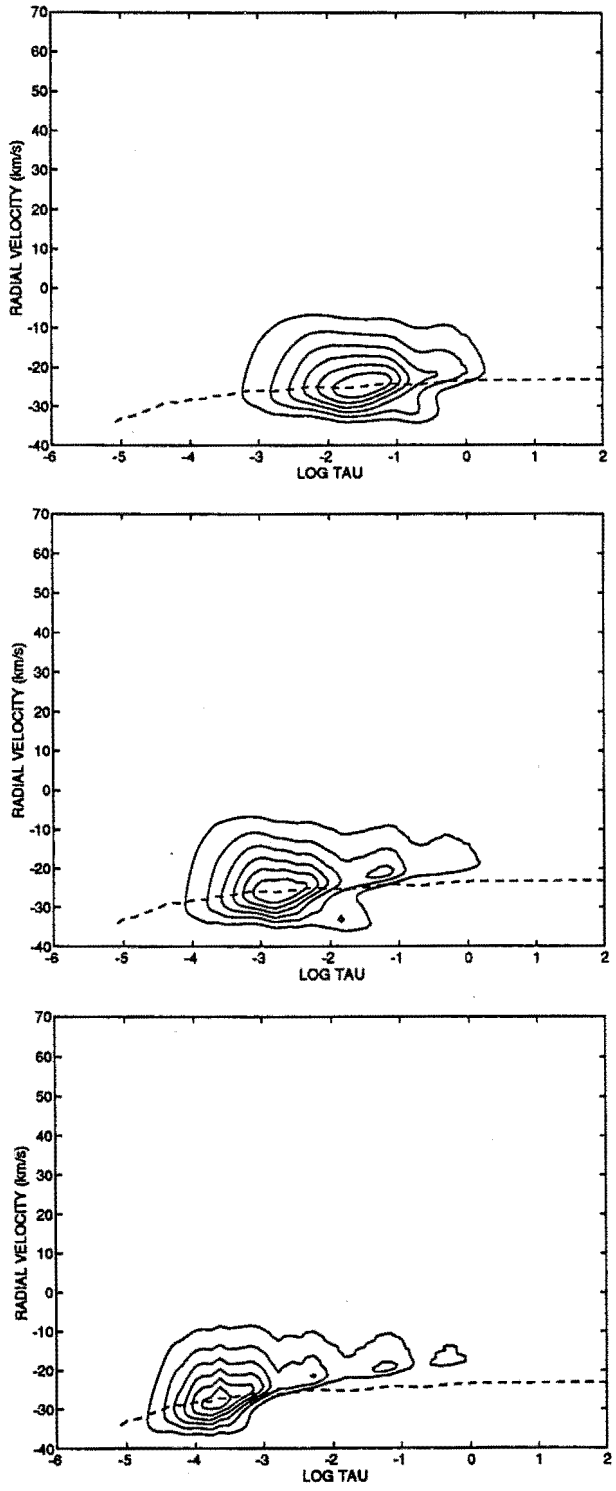

Figure 6.6: As in Fig. 6.3 for model M70210.

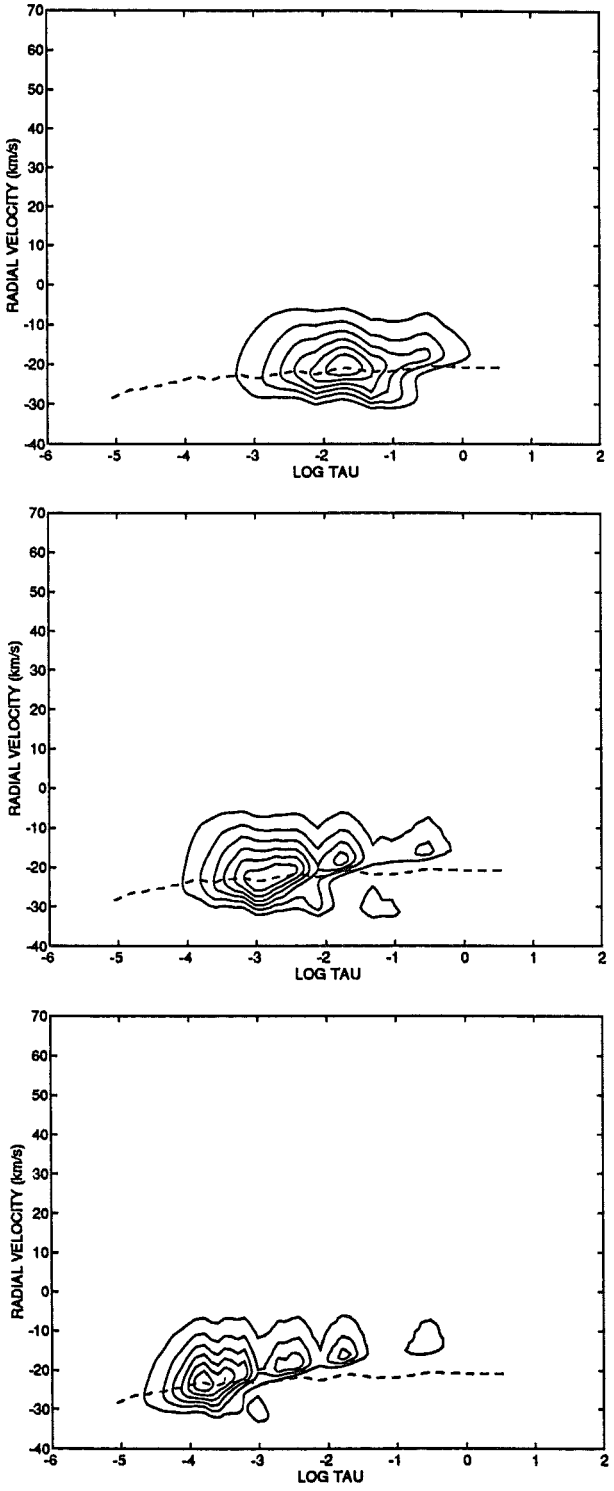

Figure 6.7: As in Fig. 6.3 for model M70230.

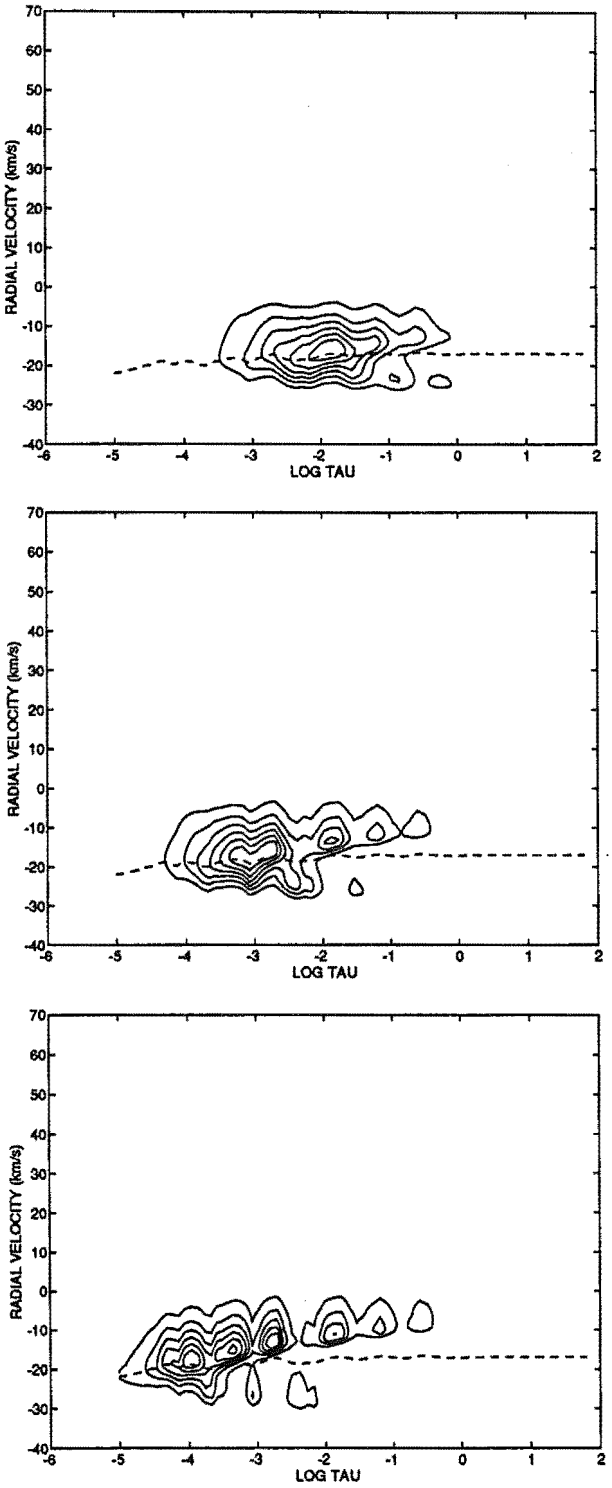

Figure 6.8: As in Fig. 6.3 for model M70260.

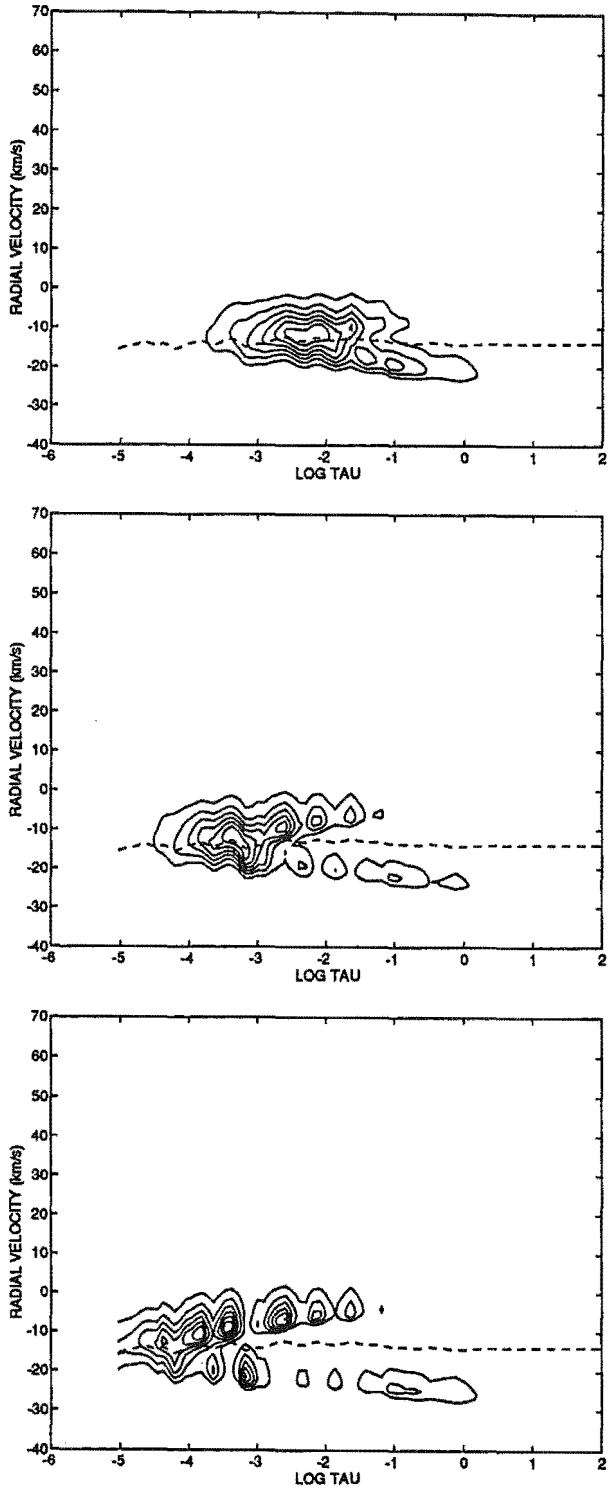

Figure 6.9: As in Fig. 6.3 for model M70285.

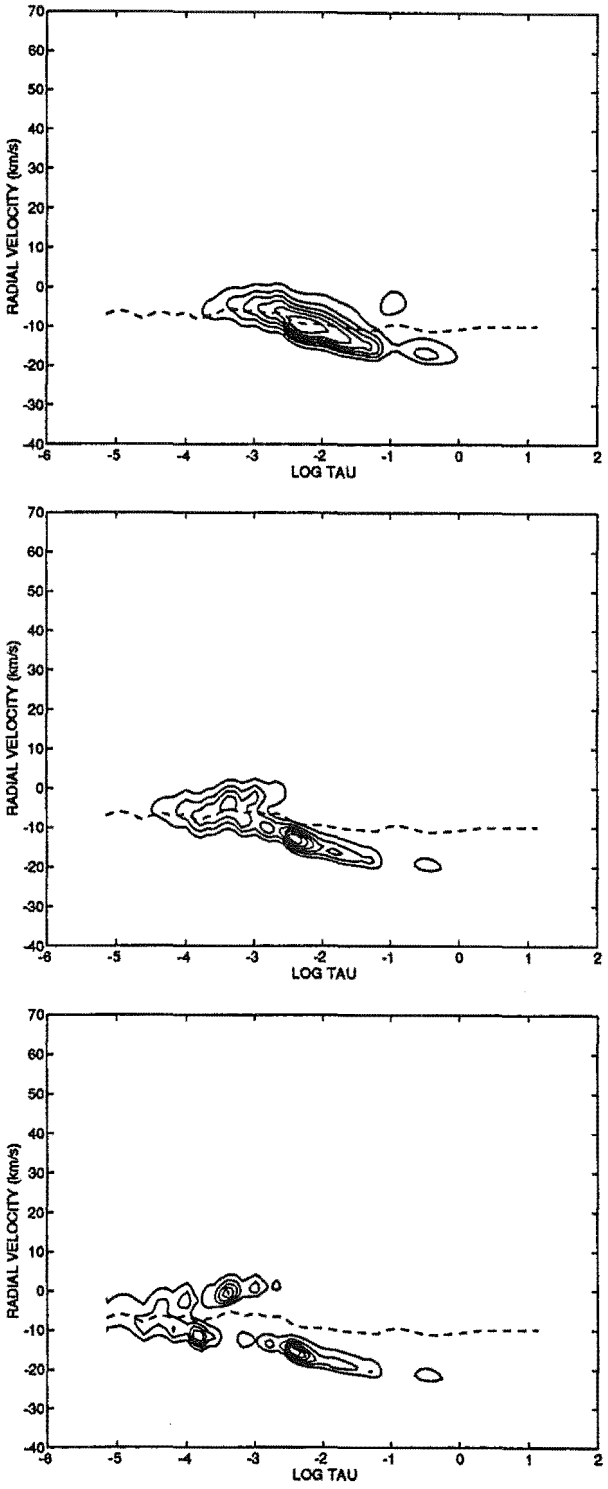

Figure 6.10: As in Fig. 6.3 for model M70310.

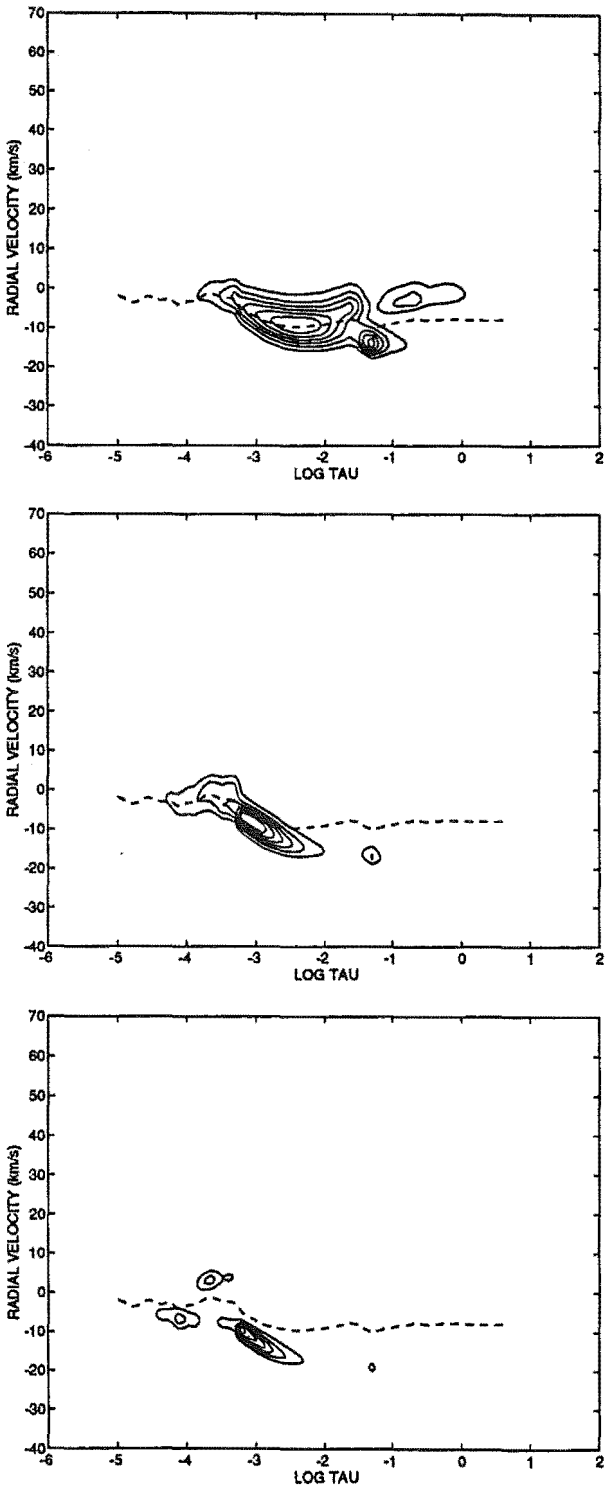

Figure 6.11: As in Fig. 6.3 for model M70325.

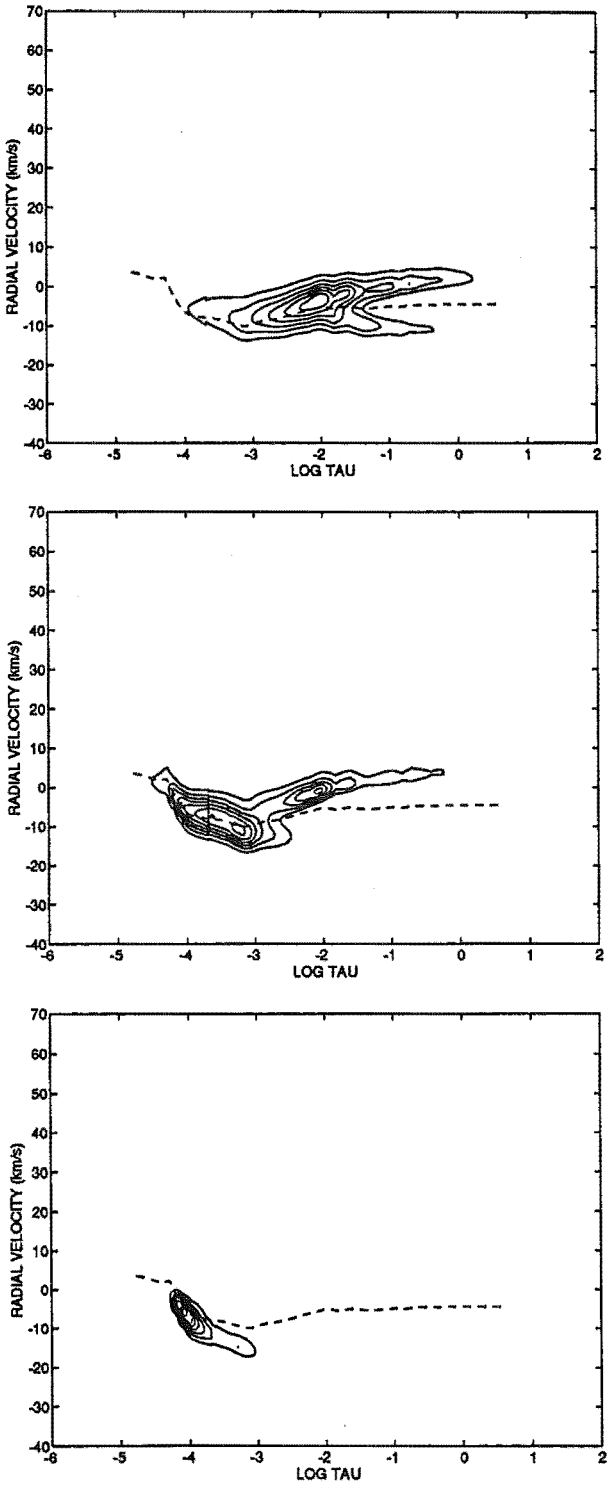

Figure 6.12: As in Fig. 6.3 for model M70385.

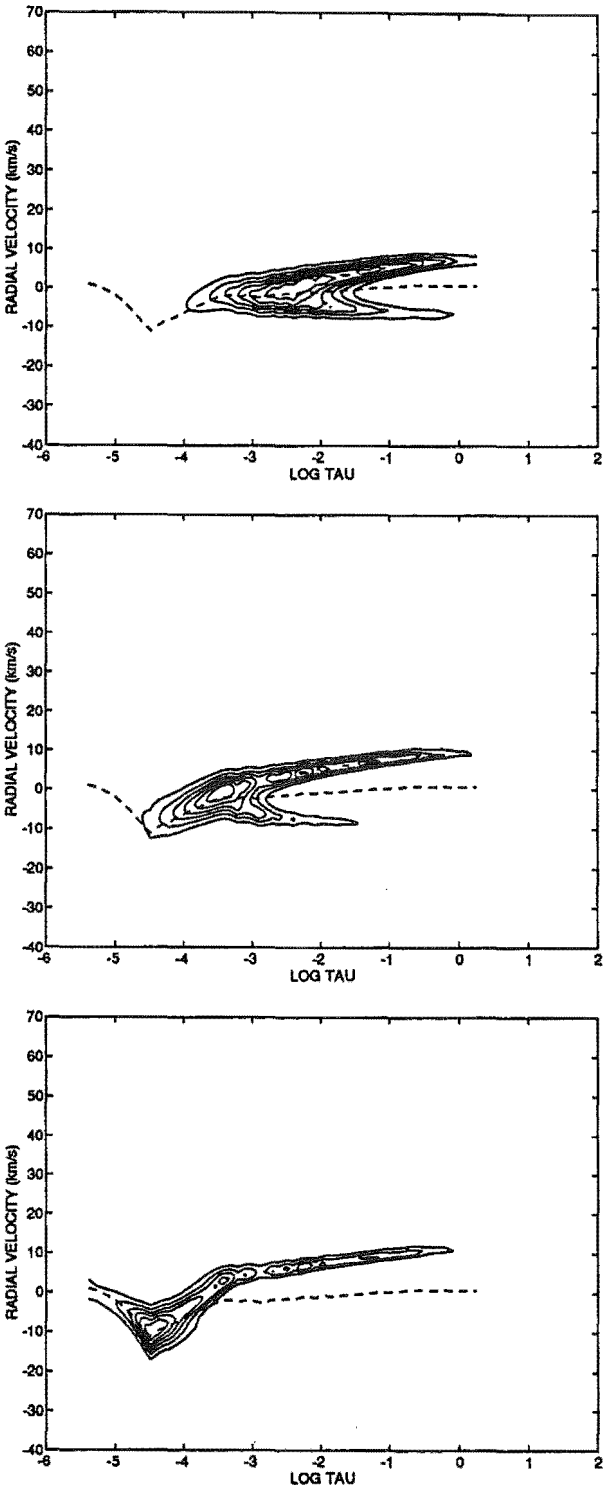

Figure 6.13: As in Fig. 6.3 for model M70440.

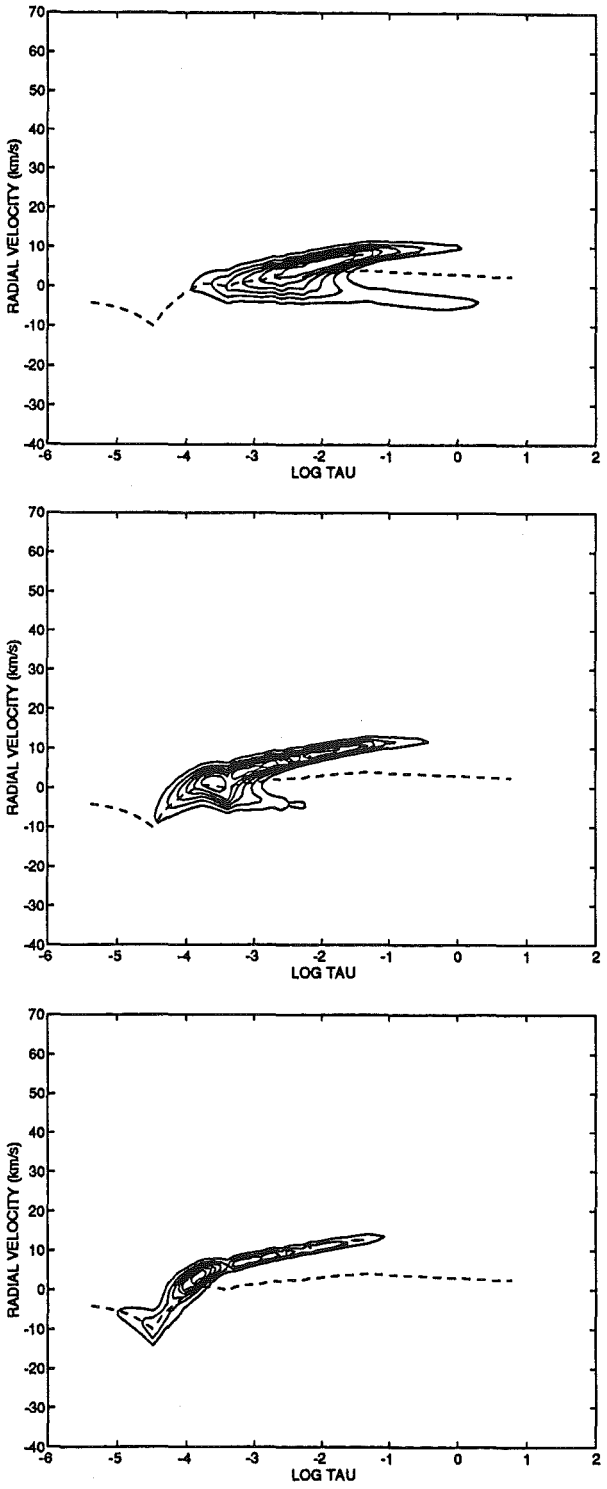

Figure 6.14: As in Fig. 6.3 for model M70450.

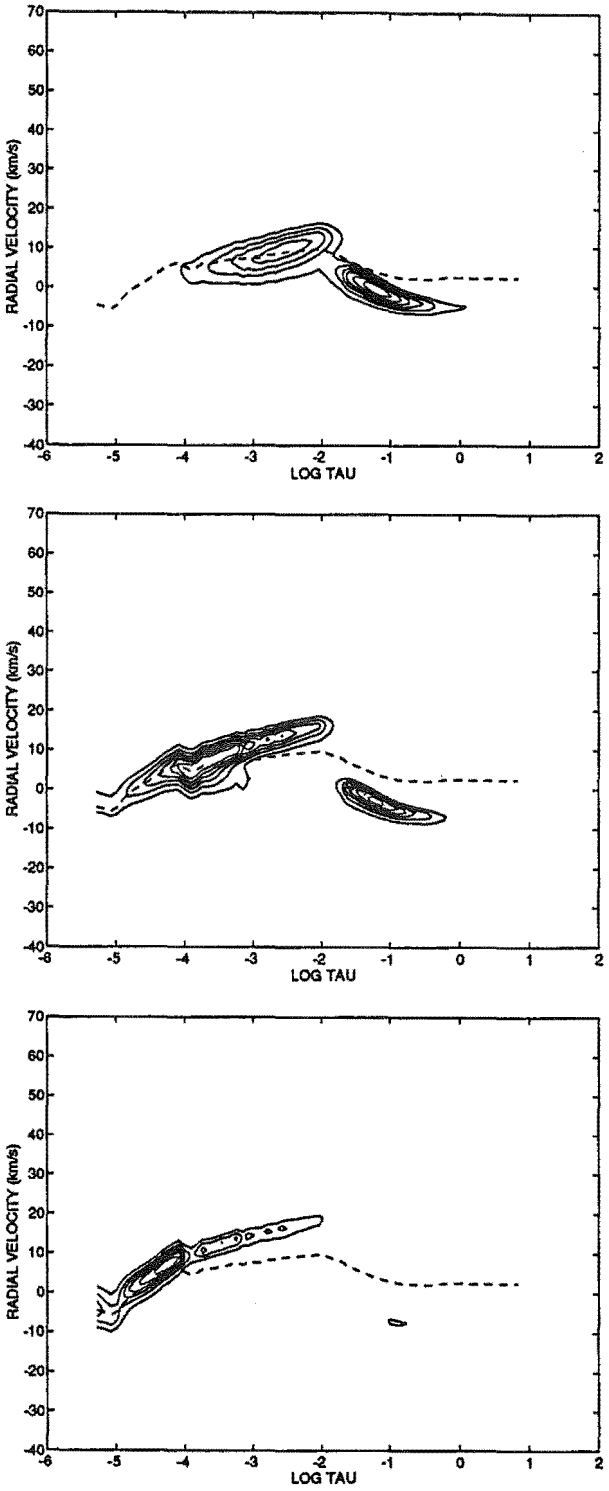

Figure 6.15: As in Fig. 6.3 for model M70475.

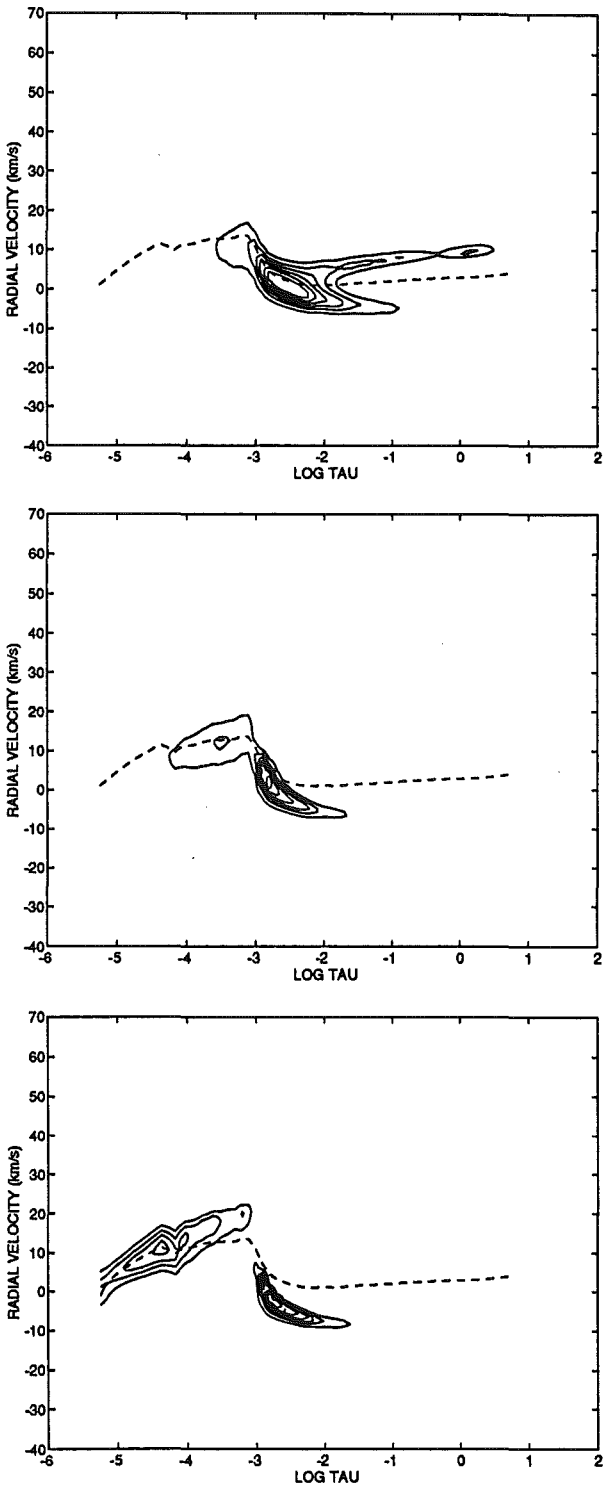

Figure 6.16: As in Fig. 6.3 for model M70545.

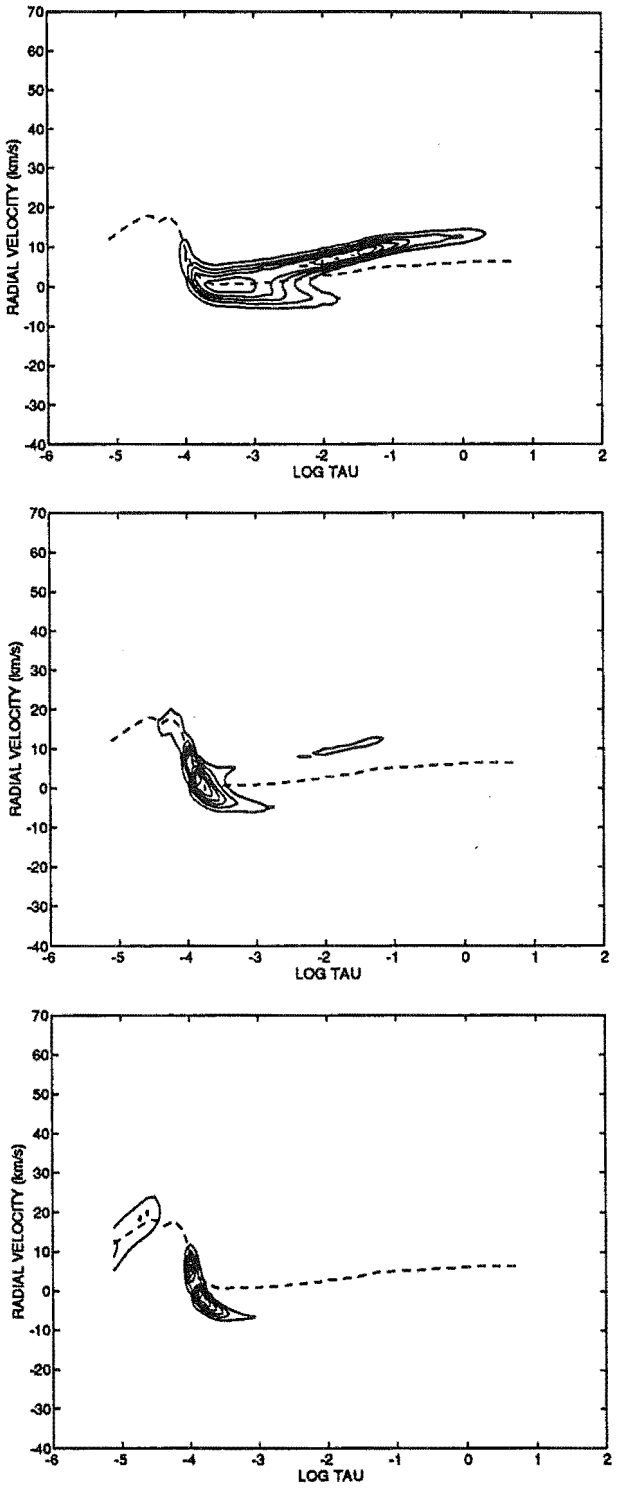

Figure 6.17: As in Fig. 6.3 for model M70645.

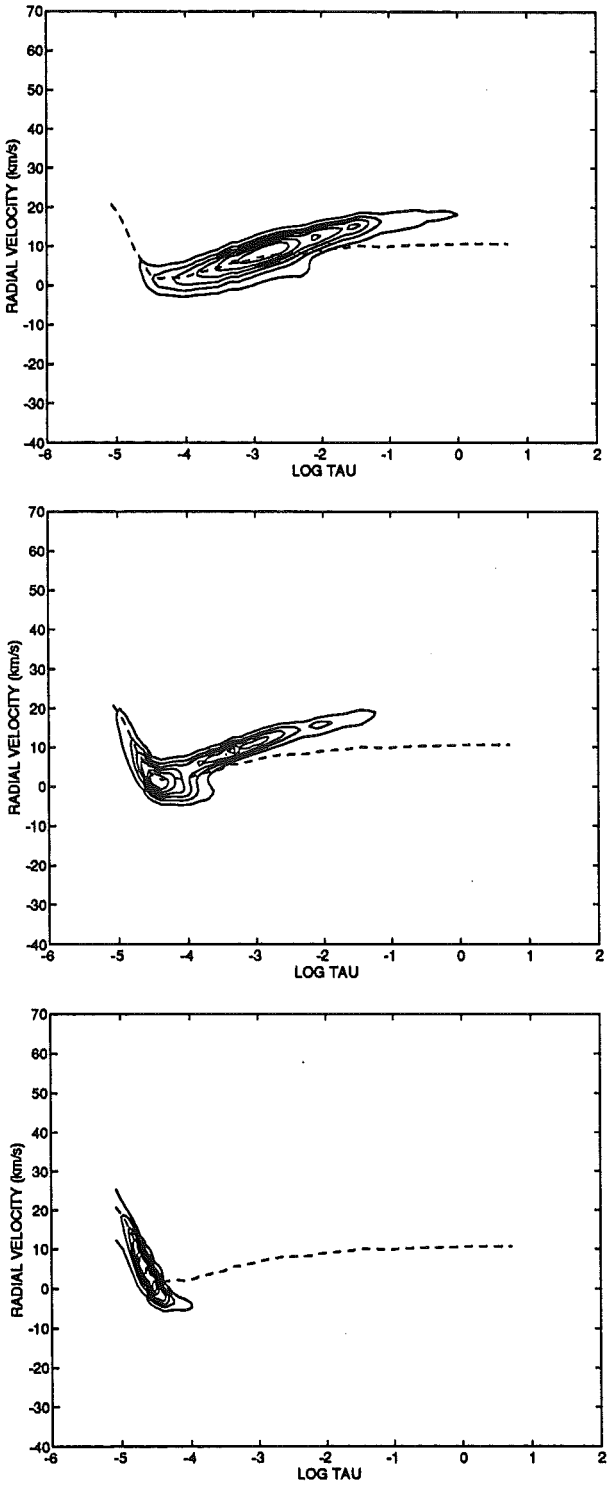

Figure 6.18: As in Fig. 6.3 for model M70715.

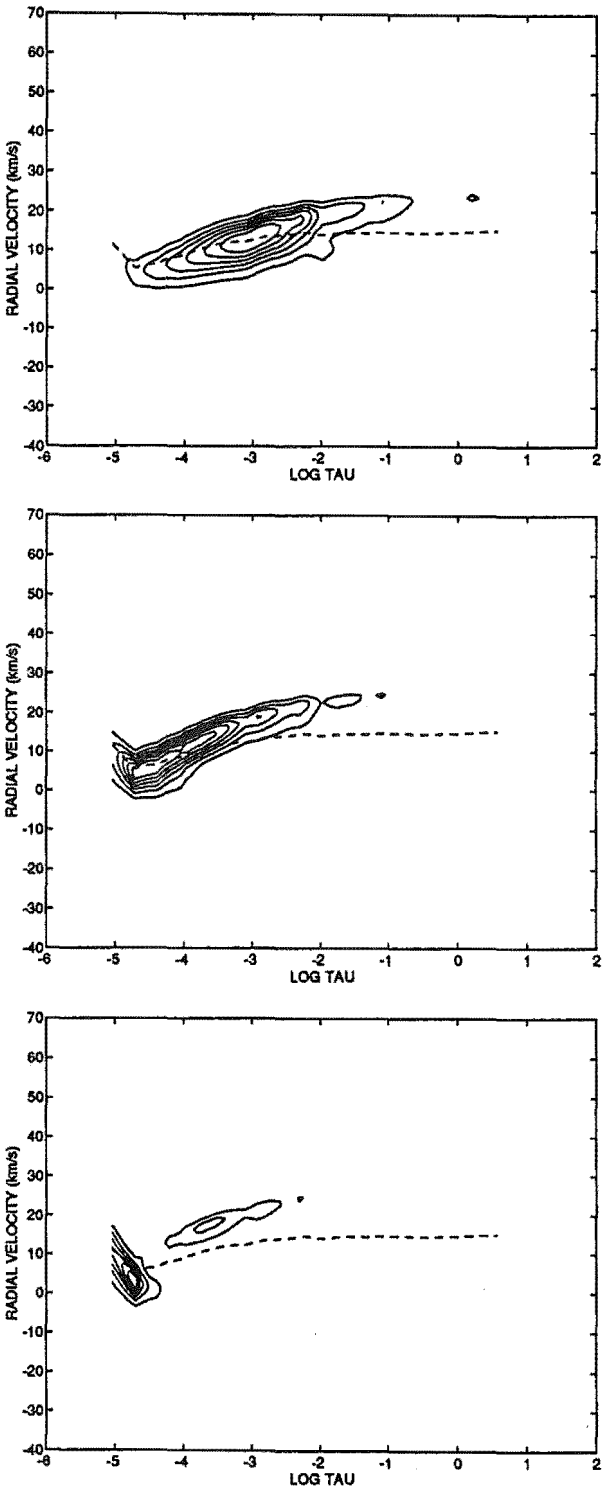

Figure 6.19: As in Fig. 6.3 for model M70735.

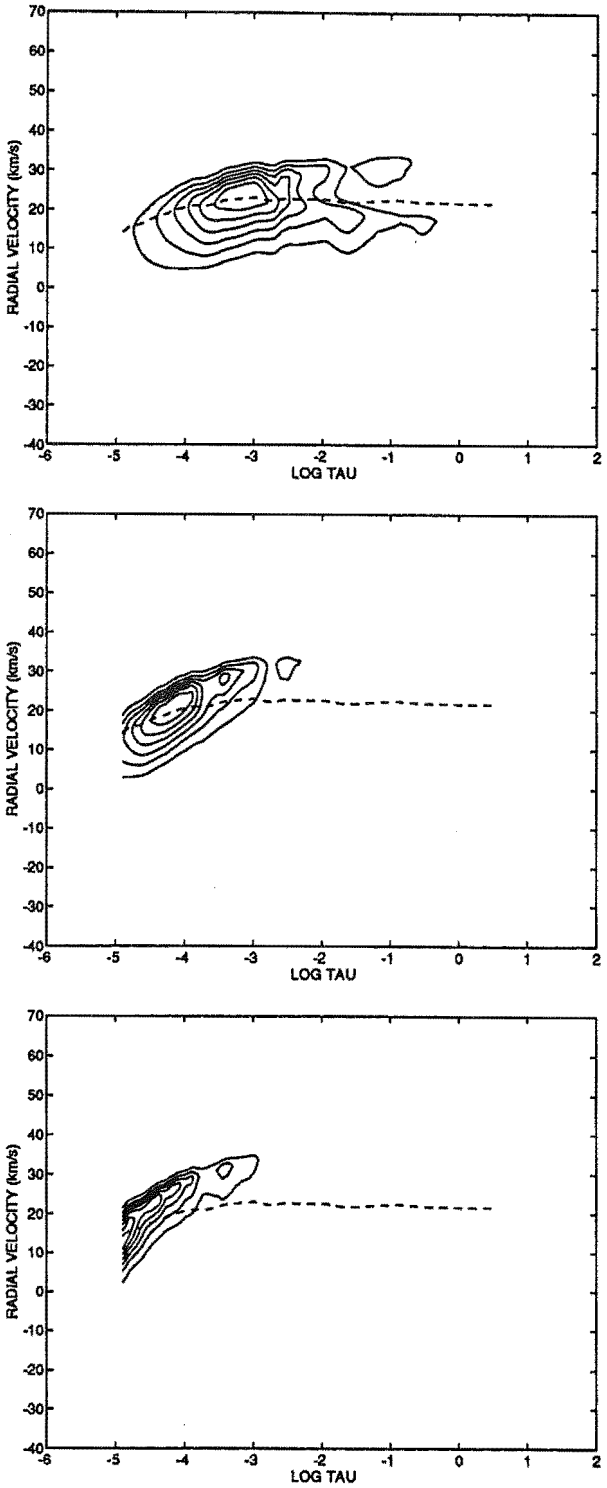

Figure 6.20: As in Fig. 6.3 for model M70745.

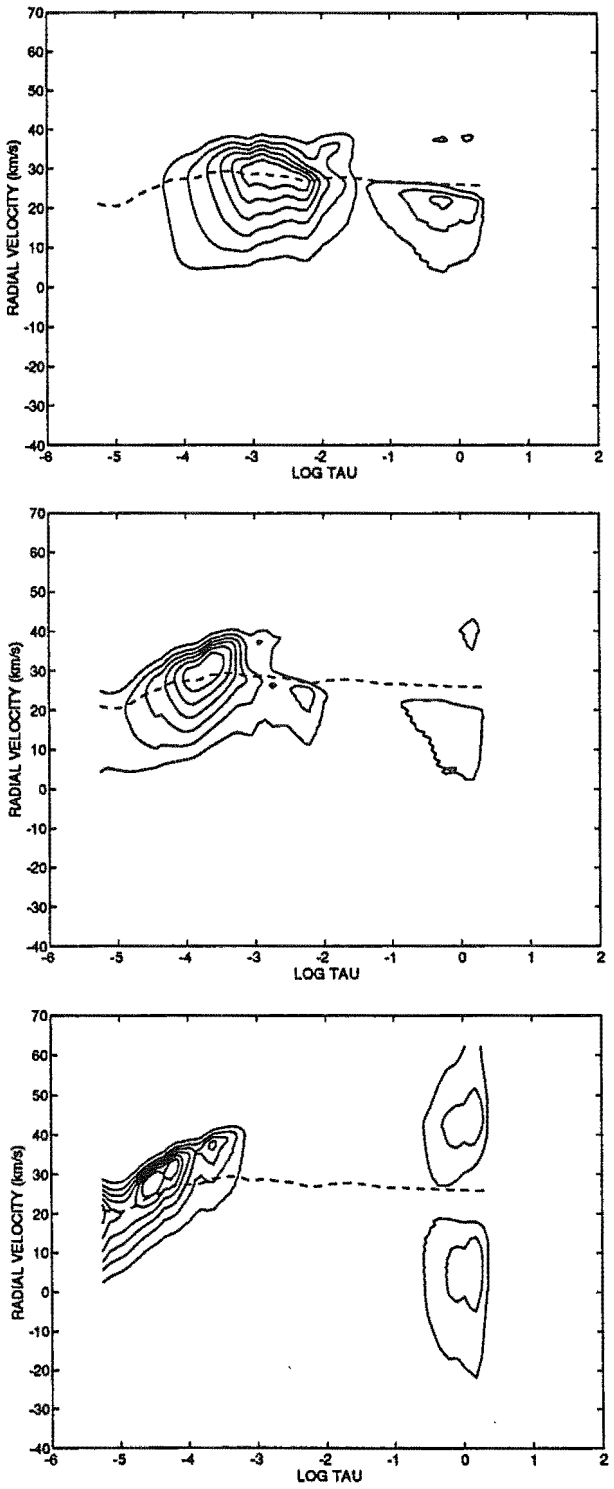

Figure 6.21: As in Fig. 6.3 for model M70750.

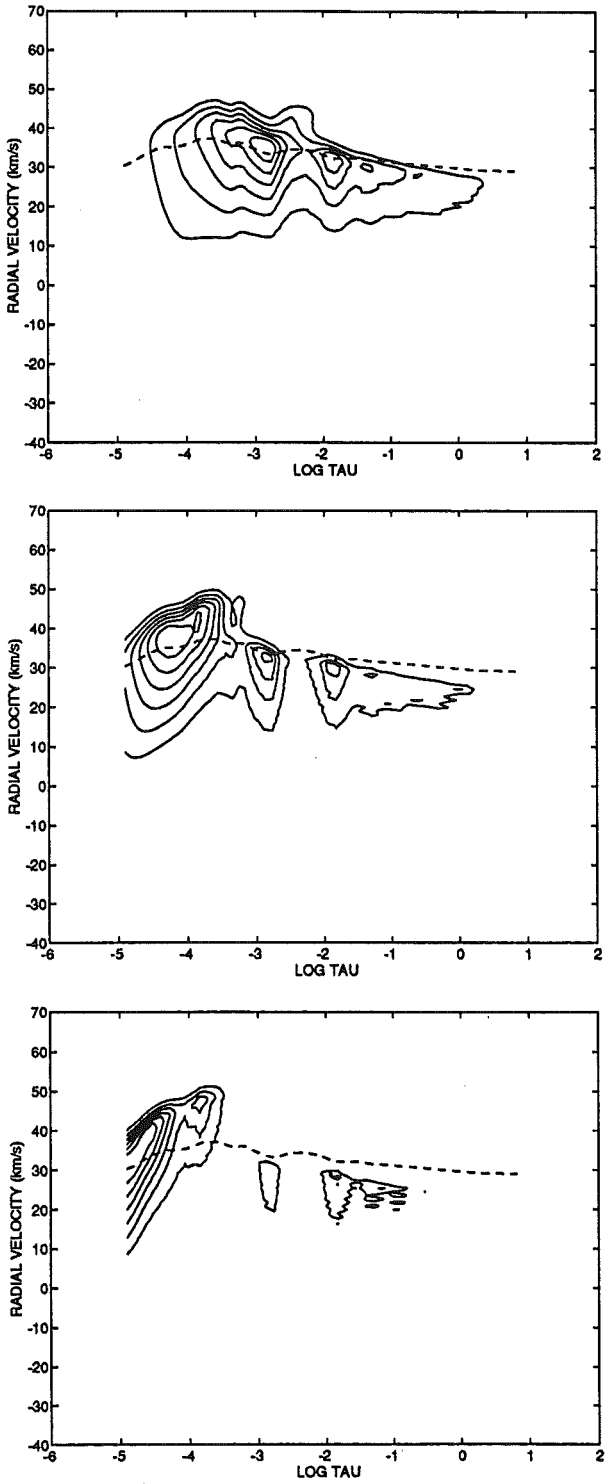

Figure 6.22: As in Fig. 6.3 for model M70760.

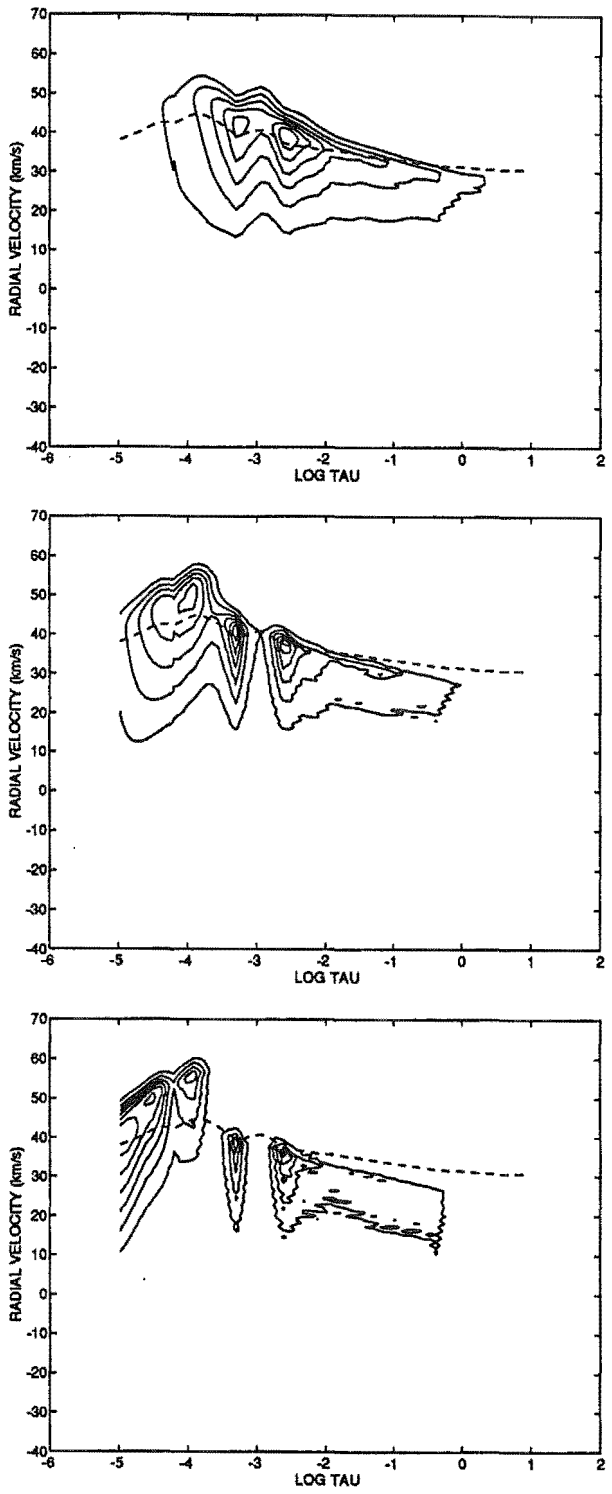

Figure 6.23: As in Fig. 6.3 for model M70785.

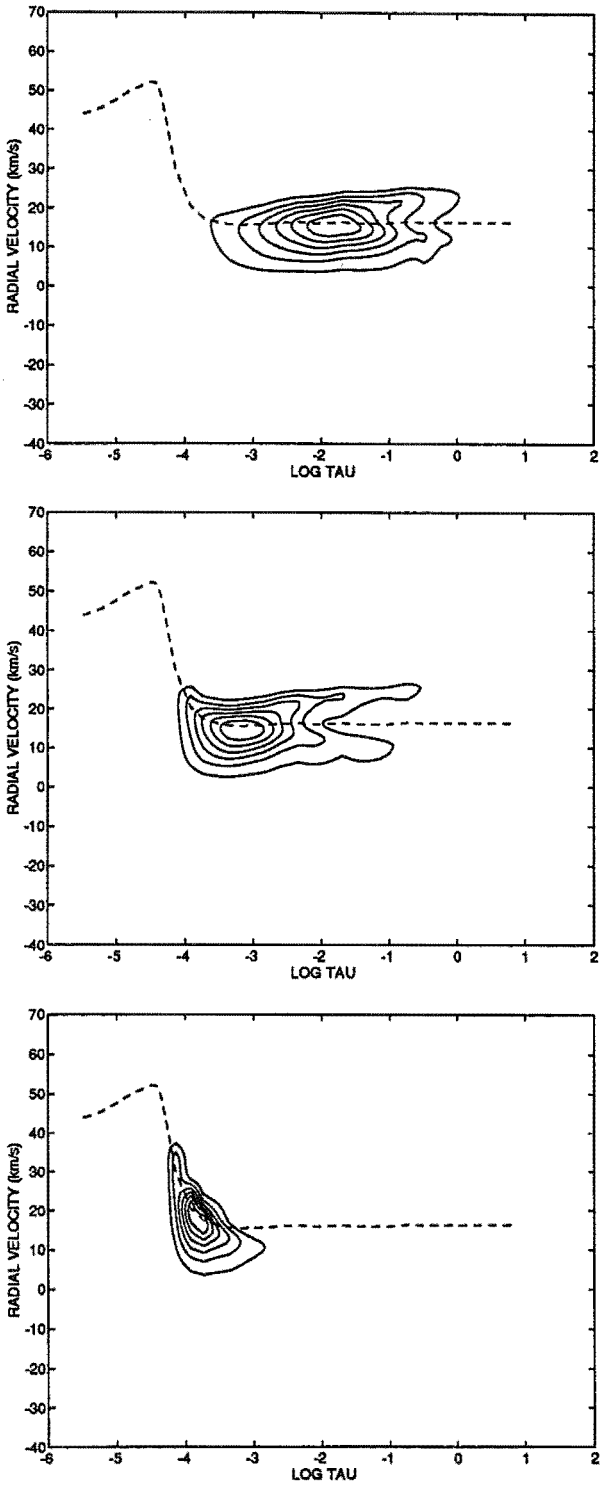

Figure 6.24: As in Fig. 6.3 for model M71090.

wing makes no contribution because it is masked by the Doppler shifted 'core' absorption. The observed core of the spectral line, which appears with a radial velocity of ~ 5 km s^{-1}, contains contributions from the blue wing of the unshifted line and the redshifted 'core'.

The effect is still present if the velocity at deeper layers is non-zero but is less than the velocity at shallower layers. Examples of this can be seen in Figs 6.22 and 6.23. It is surprising how modest a velocity gradient is required to produce this phenomenon. For the weak lines we have calculated that a velocity gradient of 10 km s^{-1} over the interval $-3 < \log\tau < -1$ is quite sufficient. However, the magnitude of the effect is strongest when the inner velocity is near to zero.

For the weak line of model M70325 (see Fig. 6.11), the additional absorption centre is caused by a slightly different circumstance. A dip in the velocity at $\log\tau \sim -1.3$ gives an extra Doppler shift to what would otherwise have been wing absorption and would have been masked by the main absorption centre.

The lines of higher strength, calculated with $\log gf = -1$ and $\log gf = 0$, are formed nearer to the stellar surface than those with $\log gf = -2$. The velocity gradients tend to increase near the surface and consequently the presence of multiple absorption centres is much more common in the higher strength lines. We would expect this to be even more so for Hα since it is formed over such a great distance. It is unlikely that multiple components resolved in the Hα profiles of Cepheids are particularly representative of atmospheric velocities.

To quantify these statements somewhat, we consider the equivalent widths of the synthetic line profiles. Those calculated with $\log gf = -2$ have equivalent widths in the range 90–250 mÅ and 4 of the 22 models show significant multiple absorption. Those with $\log gf = -1$ have equivalent widths of 150–340 mÅ and 8 of the models have multiple absorption centres. The models with $\log gf = 0$ have equivalent widths in the range 240–500 mÅ and 7 of the models have significant multiple absorption. The latter profiles are often forming right at the surface of the model atmospheres and would presumably show more multiple absorption were the models extended to smaller optical depths and included chromospheres.

From inspection of all the contour diagrams (Figs 6.3-6.24), it would appear that multiple absorption is relatively common and is usually not resolved. Even subtle velocity gradients can have a large effect on the depth of formation of a spectral line. This makes it very difficult, and perhaps even impossible, to

use spectral lines of different excitation potentials as tracers of differential atmospheric motion in pulsating stars.

The phases of two of the models discussed above, M70325 and M70475, are those at which bumps are present on the ascending part of the radial velocity curve (see Fig. 5.7). As we look to the lines of greater strength in these models, the main centre of absorption shifts from the deeper location to the shallower layers (Figs 6.11 and 6.15), accompanied by a lowering of the amplitude of the radial velocity curve bumps (see Figs 5.6 and 5.5). This is very similar to the behaviour observed in W Sgr (Figs 3.4 and 3.5) where the bump on the metallic line radial velocity curve near phase 0.4 becomes a shoulder on the Hα curve.

6.2 Projected radial velocities

We will now compare our measured radial velocities from the synthetic spectra with the velocities present in the model atmospheres. There are two approaches which we can take and we will look at each one in turn. The first of these is to adopt the static atmosphere projection factors calculated in Chapter 2. We can then calculate pulsational velocities from our radial velocities and compare them directly with the atmospheric velocities. The second approach (see Sections 6.3 and 6.4) is to work in the other direction and use the measured radial velocities and the known atmospheric velocities to compute projection factors which we can compare with those previously calculated.

We start with the first of these approaches and will exclusively use the synthetic spectra calculated with $\log gf = -2$ (Fig. 5.4). We are most interested in these weak-to-moderate strength metallic lines as they are predominantly used for radial velocity measurements. Since these lines have γ values ranging as high as 4 (Fig. 5.10), we use (2.4) and (2.5) for the projection factors rather than adopting constant values. Pulsational velocities were calculated from the bisectors of each of the synthetic lines at depths of 0.5 and 0.9. These were compared to the velocities at the appropriate phase of each zone in the hydrodynamic model. The best-fit zone was then determined in a least squares sense. Plots of the fitted velocities are shown in Figs 6.25 and 6.26 and the rms and maximum residuals are given in Table 6.1.

In order to eliminate effects due to the presence of multiple absorption centres in the model atmospheres, we repeated the fitting procedure after removing the velocities from the models showing significant multiple absorption. The models

Table 6.1: Summary of rms and maximum residuals for the zones in the hydrodynamic model best fitted by the projected radial velocity measurements.

models	line depth	zone	σ (km s^{-1})	max. resid. (km s^{-1})
all	0.5	37	1.4	3.4
	0.9	37	1.3	3.3
no double	0.5	36	1.6	4.0
absorption	0.9	37	1.2	3.3
no bump	0.5	38	1.0	2.3
phases	0.9	37	0.9	1.7
no bump or	0.5	38	1.0	2.3
piston phases	0.9	37	0.9	1.7

eliminated were M70325, M70475, M70760 and M70785 with phases 0.385, 0.574, 0.902 and 0.938 respectively. The results are given in Table 6.1, but they are not significantly different from those obtained with these models included.

The process was repeated again, this time with the elimination of those models at phases where the main bumps are present on the velocity curves. The models removed were M70310, M70325, M70475, M70545 and M70645 with phases 0.353, 0.385, 0.574, 0.617 and 0.662 respectively. Additional to these, the fitting procedure was also carried out with the model, M71090, at the piston phase 0.985 removed. The results from these fits are again given in Table 6.1. The rms velocity error was reduced for each of these fits, but the best fit zone did not change significantly. The velocities at any given phase for zones 36–38 are almost identical so we do not give plots of these fits. We will now look at the second approach.

6.3 Projection factors

When we come to calculate projection factors from the radial velocities measured from the synthetic spectra, there is an immediate question as to what is the appropriate pulsational velocity to use. In a velocity-stratified atmosphere, the concept of a single stellar pulsational velocity is not well defined. We have used a mean velocity weighted by the contribution function for each spectral line.

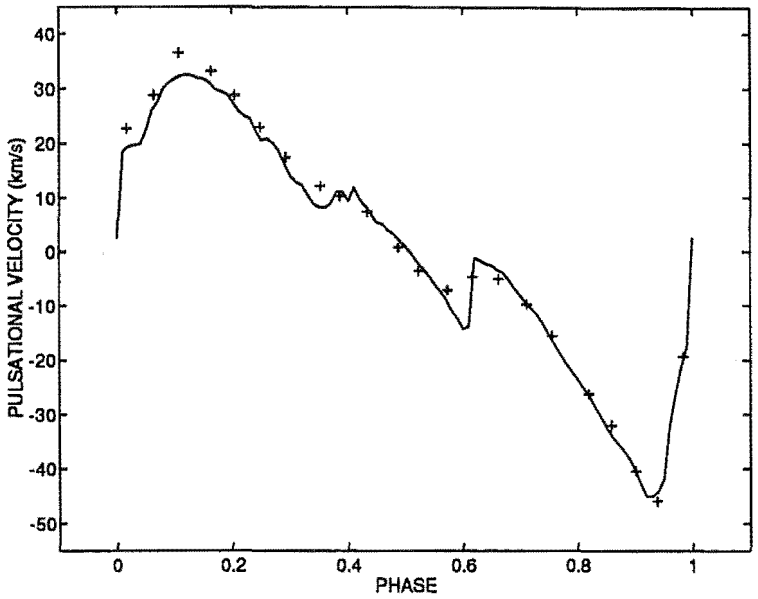

Figure 6.25: Comparison of the velocities of the best fit zone from the hydrodynamic model, ——, with the projected radial velocities, +, for line depth 0.5.

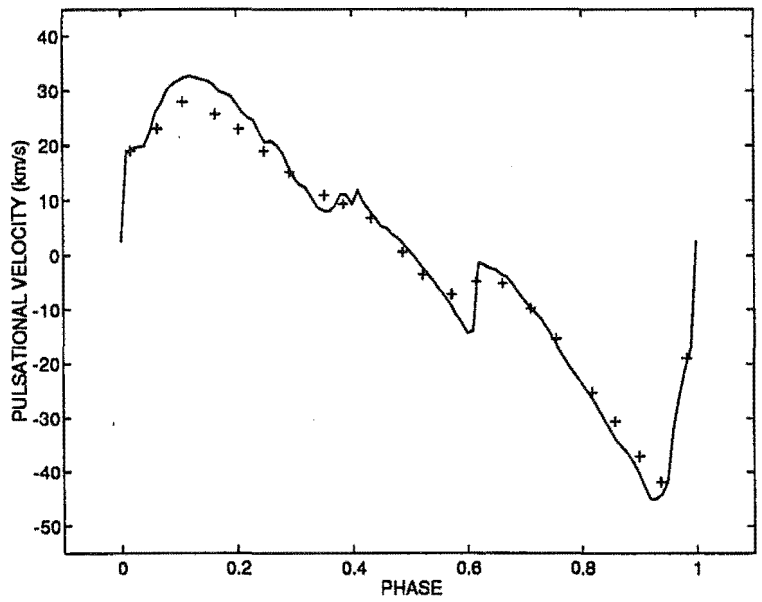

Figure 6.26: As for Fig. 6.25, but for line depth 0.9.

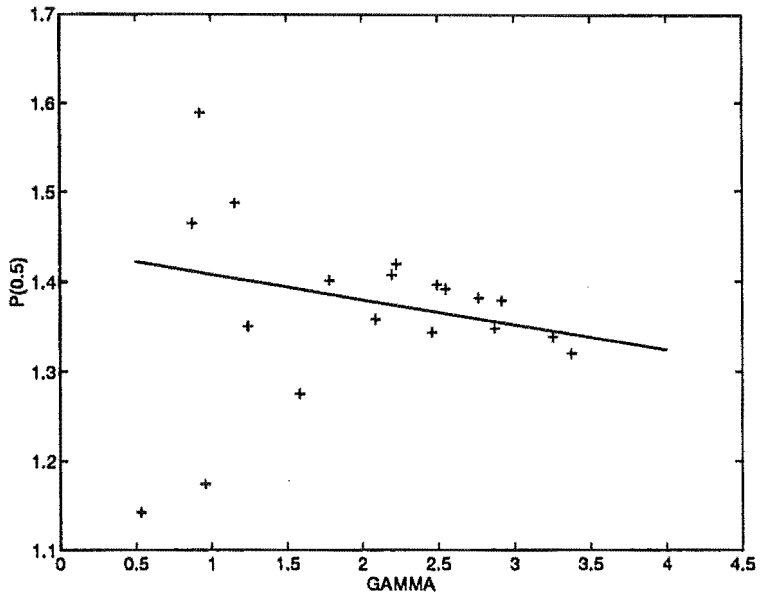

Figure 6.27: Projection factor versus γ for the synthetic line profiles measured at line depth 0.5 with $\log gf = -2$, (+). Pulsational velocities defined by (6.15). Also shown is the relation derived from static model atmospheres, (2.4), (——).

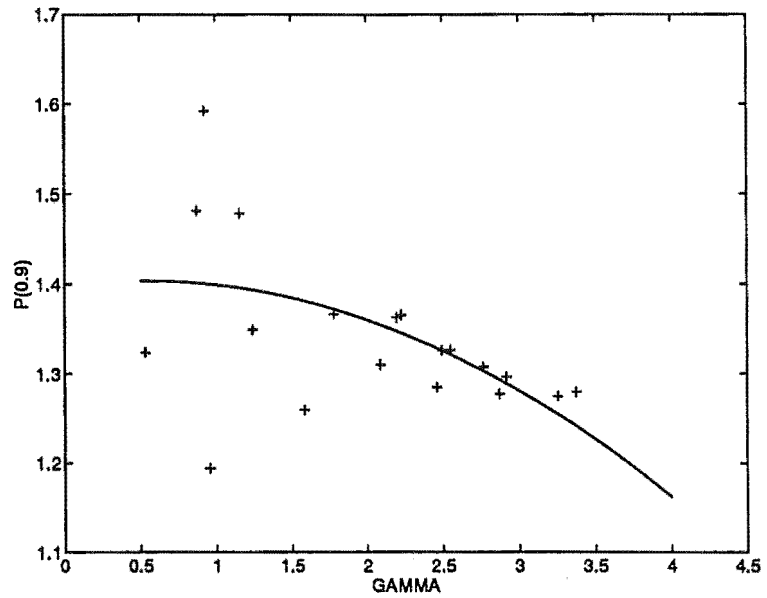

Figure 6.28: As for Fig. 6.27 for line depth 0.9, (+). Static atmosphere relation (2.5), (——).

Thus

$$V_P = \frac{\sum_\lambda \int_{-\infty}^{+\infty} C_U(x) v(x) \mathrm{d}x}{\sum_\lambda \int_{-\infty}^{+\infty} C_U(x) \mathrm{d}x}, \tag{6.15}$$

where $x = \log_{10} \tau_0$, $v(x)$ is the atmospheric velocity field, and the summation is for equally spaced wavelength points over the line profile. The projection factors obtained using this pulsational velocity and the radial velocities measured from the synthetic line profiles are shown in Figs 6.27 and 6.28, along with the relations (2.9) and (2.10) obtained using static model atmospheres.

For line depth 0.5 and $\gamma \gtrsim 2$ the points agree well with the relation (2.9). There is considerable scatter at low γ-values. For line depth 0.9, there is again considerable scatter for $\gamma \lesssim 2$, while the points at higher γ-values do not follow the static atmosphere relation (2.10) as well as those from line depth 0.5. This is consistent with the low asymmetry at maximum γ in Fig. 5.10 and indicates that the radial velocity at line depth 0.5 may be more reliable than that at line depth 0.9 in this case. However, this cannot be true in all circumstances because there are points lying *above* the constant-velocity curve, near $\gamma = 2.8$ in Fig. 6.27, while the corresponding points in Fig. 6.28 lie *on* the constant-velocity curve.

An alternative way of determining constant projection factors is to match the radial velocities we have measured, to the pulsational velocity of each zone in the hydrodynamic model. For each zone and line depth, a projection factor can be calculated by minimising the sum of the squared residuals,

$$P = \frac{\sum_j v_{r,j} v_{p,j}}{\sum_i v_{r,i}^2}, \tag{6.16}$$

where $v_{r,j}$ and $v_{p,j}$ are respectively the radial velocity and pulsational velocity at phase j. The best-fit zone can then be deemed to be that with the smallest rms error. We have already determined (Section 6.2) that the pulsational velocities at the bump phases are not well fitted by the radial velocities so we will exclude these phases (listed in Section 6.2) from our calculation. The best-fit zones and their projection factors and rms errors are given in Table 6.2.

Comparing these rms residuals with those of Table 6.1, we can see that marginally better fits can be obtained by using the relations (2.4) and (2.5) for the projection factor than by using even the best constant factor. We note that using (2.4) and (2.5), the mean projection factors for these line profiles would be $P(0.5) = 1.38$ and $P(0.9) = 1.35$.

Table 6.2: Summary of the constant projection factors and velocity residuals for the best-fitted zones in the hydrodynamic model.

models	line depth	zone	P	σ (km s^{-1})	max. resid. (km s^{-1})
all	0.5	37	1.36	1.5	3.0
	0.9	37	1.30	1.4	3.2
no bump	0.5	38	1.36	1.1	2.6
phases	0.9	38	1.30	1.0	2.0

6.4 Motion of the photosphere

So far we have considered the projection of the radial velocities of our synthetic spectra onto the pulsation velocity of mass zones in the hydrodynamic model. In the Baade-Wesselink method, a fractional change in the radius of the photosphere is determined photometrically. This photospheric radius is the point in the stellar atmosphere where the Rosseland mean optical depth equals one or the temperature equals the effective temperature. What needs to be determined spectroscopically is the absolute change in the photospheric radius in a given phase interval. The motion of the photospheric radius will, in general, not be the same as the motion of any given mass element.

In each of the converged model atmospheres (Chapter 4), we have determined the point at which the temperature equals the effective temperature. We have also determined the point where the Rosseland mean optical depth equals one. Because these model atmospheres have the same pressure-density-velocity structure as the hydrodynamic model, we can easily determine the radius at these points. We have found in our model atmospheres that the radii of the two points always agree to better than 0.1 per cent. In Fig. 6.29, we plot the photospheric radius of our model against phase along with the radius of zone 37, which was determined as one of the best-fit zones in Sections 6.2 and 6.3.

The radius of the best-fit mass zone to the radial velocity measurements follows the photospheric radius only near the phase of minimum radius, when the atmosphere is most compressed. Near maximum radius, the atmosphere is more extended and the depth of spectral line formation is spatially separated from the photospheric radius. The rms difference in radii between the two is 0.66 $R_\odot$. This is at least an order of magnitude greater than the separation between the line and

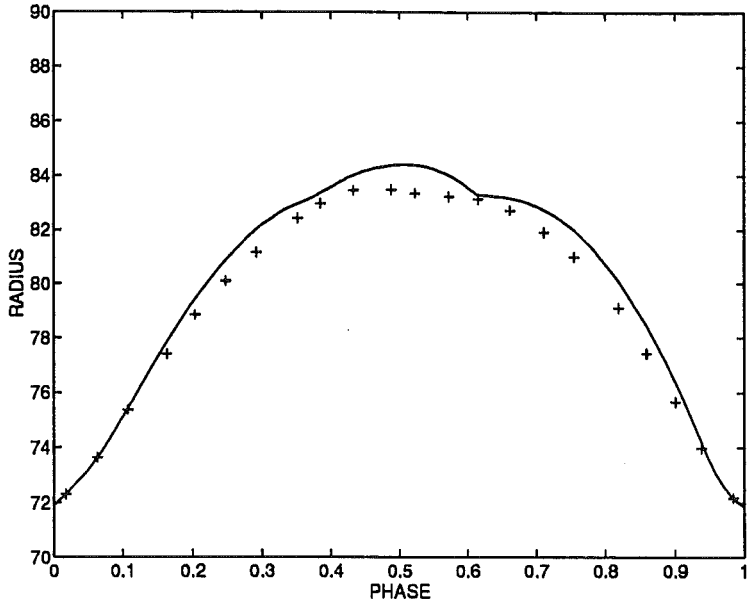

Figure 6.29: Radii of the photosphere (+) and zone 37 (——) as a function of phase.

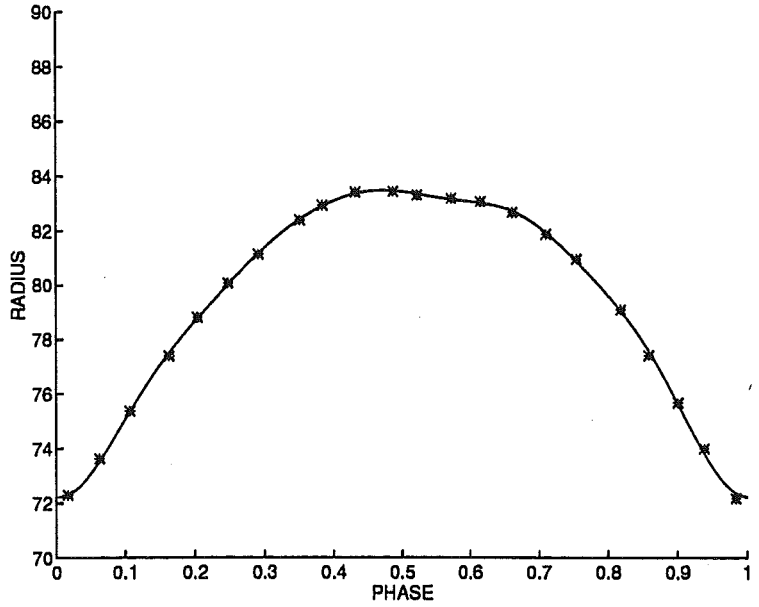

Figure 6.30: Fifth-order Fourier series fit to the photospheric radius.

continuum forming depths calculated by Gautschy (1987) from the static models of Kurucz (1979) but still justifies the use of plane-parallel models.

In order to determine a velocity curve we have fitted a 5th order Fourier series to the photospheric radius values (Fig. 6.30). The standard deviation of the fitted points is $\sigma_R = 0.12\ R_\odot$ and the mean radius <R> = (79.4486±0.0006) $R_\odot$. Differentiating this curve analytically gives the photospheric velocity curve which we compare in Figs 6.31 and 6.32 with the radial velocities projected using (2.9) and (2.10). There is a significant phase lag between the two curves which changes with phase because of the different and changing mass zones contributing to the velocity of each. In particular, there is an overestimate of the photospheric velocity near pulsation velocity minimum (radial velocity maximum) of ~ 15 km s^{-1}. Moffett (1989) comments that given a correct surface brightness relation, photometric and spectroscopic curves should be in both phase and shape agreement. This will clearly not be so if, as for our model, there is an intrinsic difference between the two curves because of this level effect. The rms velocity differences between the projected radial velocities and the photospheric velocities are 5.6 km s^{-1} and 4.5 km s^{-1} for line depths 0.5 and 0.9 respectively. Although these velocity errors seem high, they would lead to standard errors in a maximum likelihood radius measurement of only 0.81 $R_\odot$ for line depth 0.5 and 0.65 $R_\odot$ for line depth 0.9, assuming that the errors are normally distributed (Balona 1977). This is more likely to be the case if phases of maximum radial velocity are excluded. The radius errors are consistent with the rms difference (0.66 $R_\odot$) found above between the photospheric radius and the radius of zone 37 of the hydrodynamic model.

We have determined projection factors by dividing the photospheric velocity at the appropriate phase by each of the radial velocity measurements. Because of the different shapes of the photospheric and radial velocity curves, due mainly to the phase lag, there is a large scatter in the derived values of the projection factors. Consequently we do not quote them here.

6.5 Asymmetry

We now return to the subject of the asymmetries of spectral lines. In Chapter 2 we derived a relationship between spectral line asymmetry and γ, the ratio of pulsation velocity to line half width at half height, for an atmosphere with a constant radial velocity. In Chapter 3 we found that Cepheid line profiles are

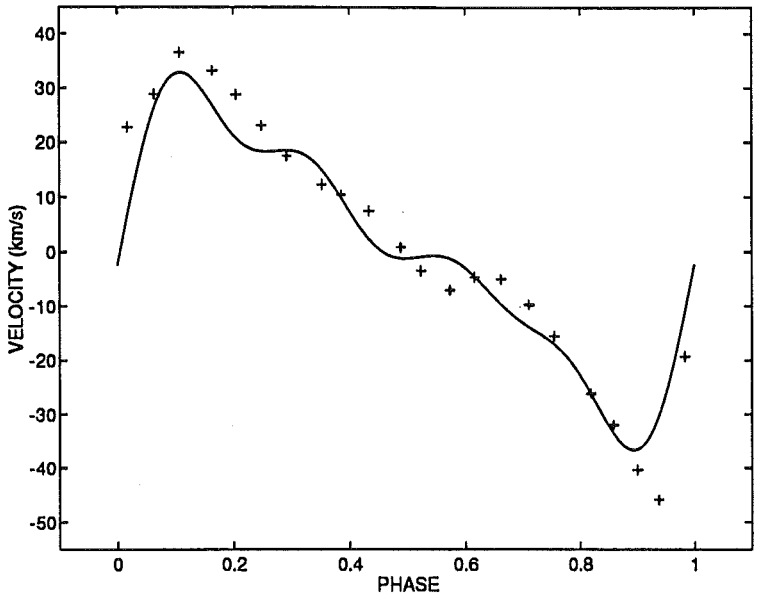

Figure 6.31: Velocity of the photosphere (——) and projected radial velocities from line depth 0.5 (+) as a function of phase.

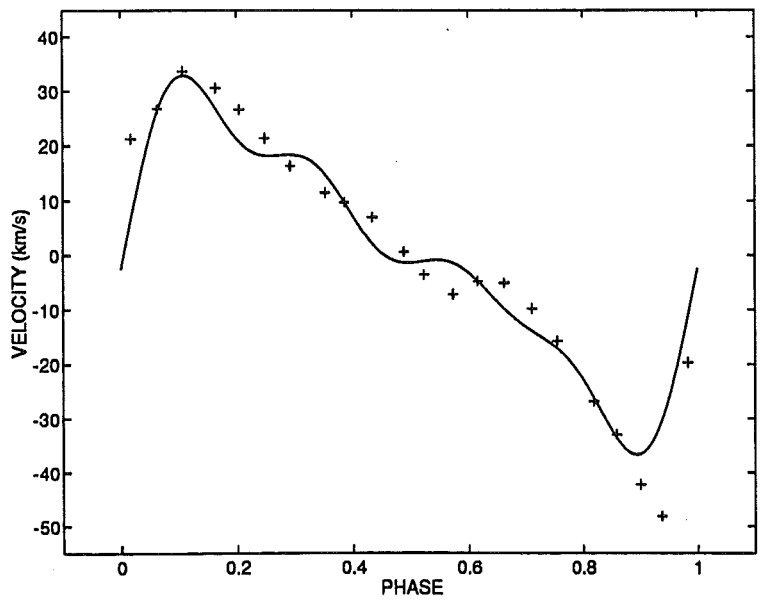

Figure 6.32: As for Fig. 6.31, but for line depth 0.9

Table 6.3: Line asymmetries found from tests of different velocity fields.

Velocity	γ	A	Velocity	γ	A
$2(\log\tau)$	0.43	0.02	$-(\log\tau)+30$	2.64	1.02
$4(\log\tau)$	0.80	-0.11	$-2(\log\tau)+30$	2.97	1.12
$-2(\log\tau)-10$	0.73	-0.15	$-3(\log\tau)+30$	3.06	0.90
$-4(\log\tau)-20$	1.16	-0.43	$-(\log\tau)+15$	1.77	0.22
$6(\log\tau)$	1.06	-0.29	$-2(\log\tau)+15$	1.94	0.18
$(\log\tau)^2$	0.58	-0.27	$-3(\log\tau)+15$	2.05	0.07
$2(\log\tau)^2$	0.86	-0.83	$5e^{-2(\log\tau+2)^2}+15$	1.81	0.13
$(\log\tau+4)^2$	0.61	-0.61	$10e^{-2(\log\tau+2)^2}+15$	1.90	-0.08
$2(\log\tau+4)^2$	0.85	-2.26	$15e^{-2(\log\tau+2)^2}+15$	1.90	-0.50
$(\log\tau+2)^2$	0.18	-0.03	$10e^{-(\log\tau+2)^2}+15$	2.00	0.00
$2(\log\tau+2)^2$	0.35	-0.19	$10e^{-2(\log\tau+2.5)^2}+15$	1.90	-0.06
$-\frac{1}{2}(\log\tau+2)^2+30$	2.79	1.11	$15e^{-2(\log\tau+2.5)^2}+15$	1.89	-0.43
$\frac{1}{2}(\log\tau+2)^2+30$	2.84	1.23	$10e^{-(\log\tau+2.5)^2}+15$	1.96	-0.01
$-(\log\tau+2)^2+30$	2.70	0.91	$15e^{-(\log\tau+2.5)^2}+15$	1.91	-0.32
$-2(\log\tau+2)^2+30$	2.44	0.61	$5e^{-(\log\tau+2.5)^2}+15$	1.82	0.16
30	2.85	1.22	$10e^{-\frac{1}{2}(\log\tau+2.5)^2}+15$	2.02	0.11

observed to have asymmetries which do not agree with this relationship. There is an enhanced asymmetry at phases of positive radial velocity and, for some stars, an inverse, or negative, asymmetry at negative radial velocity phases. The line profiles of the model Cepheid that were calculated in Chapter 5 show asymmetry more like the constant velocity relationship than the Cepheid observations. The question which we now investigate is whether the asymmetries observed in Cepheid line profiles can be explained by the presence of some other macroscopic velocity field in the stellar atmosphere.

6.5.1 Negative asymmetry

The only model we have calculated that showed significant negative asymmetry in the weaker set of line profiles is M70545 (see Fig. 5.7 at phase 0.62 and Fig. 5.10) . An examination of the flux contribution contour diagram for this model (Fig. 6.16) shows that the line is forming in a region of the atmosphere

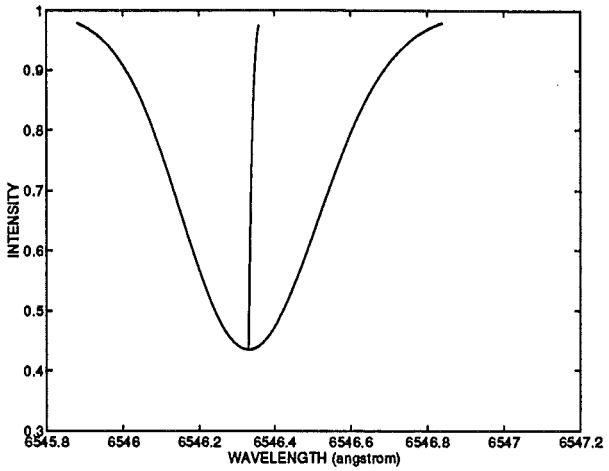

Figure 6.33: Line profile and bisector for velocity field $V = (\log \tau)^2$. The rest wavelength is 6546.245 Å. The asymmetry $A = -0.27$ km s^{-1}.

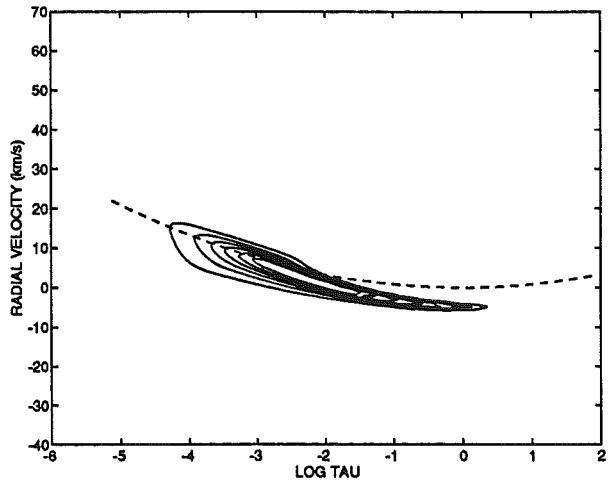

Figure 6.34: Flux contribution contour diagram for $V = (\log \tau)^2$.

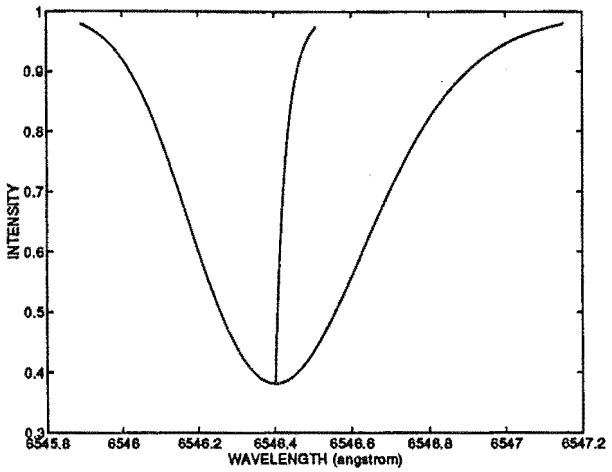

Figure 6.35: Line profile and bisector for velocity field $V = 2(\log \tau)^2$. $A = -0.83$ km s^{-1}.

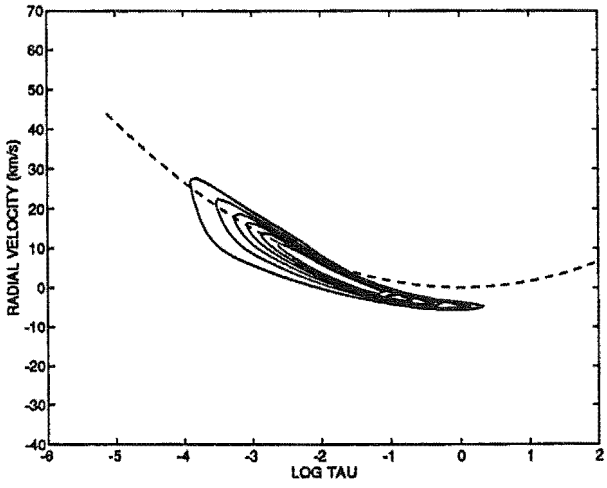

Figure 6.36: Flux contribution contour diagram for $V = 2(\log \tau)^2$.

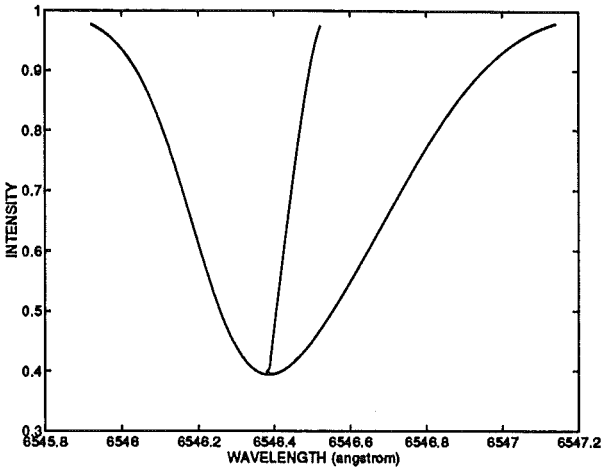

Figure 6.37: Line profile and bisector for velocity field $V = 2(\log \tau + 4)^2$. $A = -2.26$ km s^{-1}.

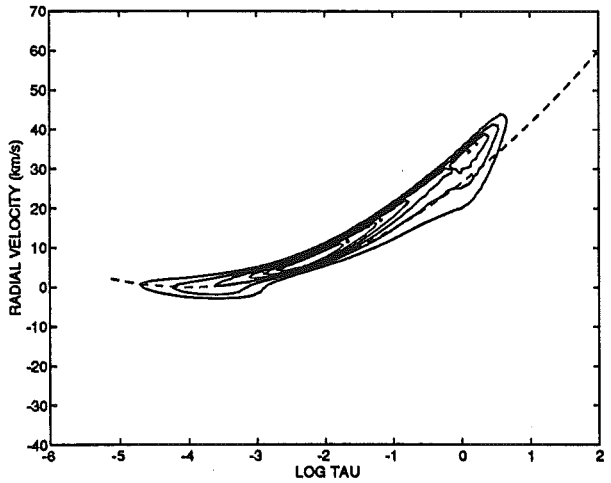

Figure 6.38: Flux contribution contour diagram for $V = 2(\log \tau + 4)^2$.

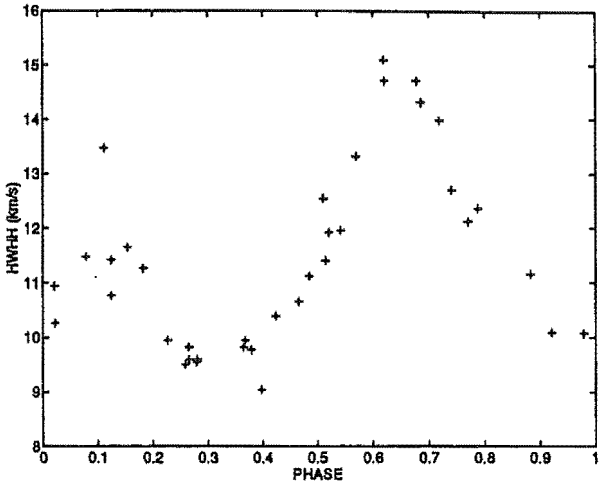

Figure 6.39: Half-width at half-height versus phase for the 6546 Å Fe I line of β Dor.

with a considerable velocity gradient. We have undertaken some numerical experiments by calculating line profiles for models containing different velocity fields. All were calculated using the Kurucz model with $T_{\rm eff} = 5000$ K, $\log g = 1.0$ and $\xi = 2$ km s^{-1}. The resulting γ-values and asymmetries are given in Table 6.3. We have found that a negative asymmetry can often result if there is a velocity gradient through the line forming region of the stellar atmosphere. The results are difficult to quantify because the degree of asymmetry depends not only on the magnitude of the velocity gradient, but also on the velocity itself and the detailed shape of the velocity field. In general, velocity gradients of $\sim$ 10–20 km s^{-1} between $-5 < \log\tau < 1$ are sufficient to produce spectral lines with negative asymmetries. In addition, strong lines are more affected by velocity gradients than weak lines. We show some examples of line profiles and flux contribution contour diagrams in Figs 6.33–6.38. The inverse asymmetry observed in the line profiles of S Mus, Y Oph and κ Pav (Figs 3.23, 3.35 and 3.29) may be indicative of the presence of velocity gradients through the line forming regions of these stars at phases of outward pulsation.

6.5.2 Enhanced asymmetry

We have carried out trials of many different velocity fields to seek one which will result in an enhanced asymmetry. We have found no velocity field which can produce a spectral line having an asymmetry greater than that which would occur if there was a constant velocity equal to the maximum magnitude of the

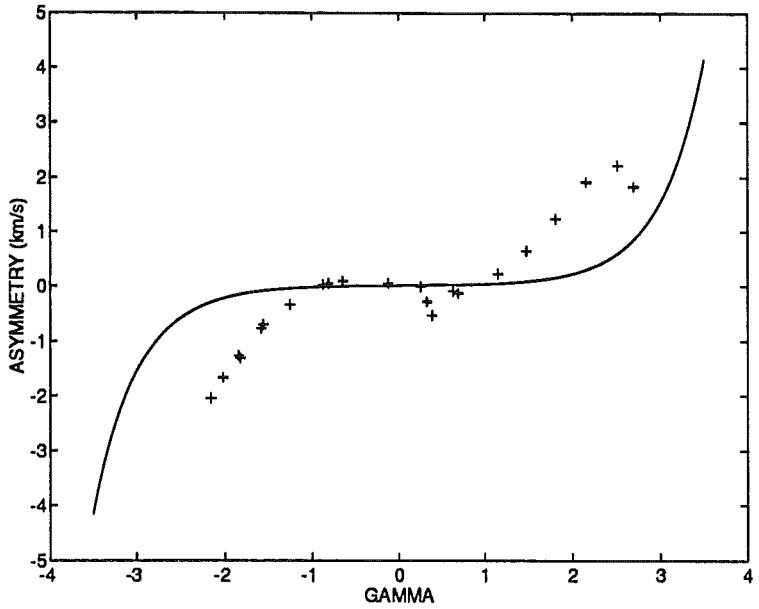

Figure 6.40: A versus γ for the synthetic spectra with $\zeta = 20$ km s^{-1}.

velocity field.

Until now, we have applied the same macroturbulent broadening function to all our synthetic spectra. Some recent studies (Breitfellner & Gillet 1993a, b, c, Kovacs & Buchler 1990) seemed to indicate the presence of a phase-dependent 'turbulence' in Cepheids. This turbulence is observed to increase markedly at the contraction phase of the pulsation cycle. An increase in half-width is also seen near radial velocity maximum in the spectra we have obtained. An example is shown in Fig. 6.39. The 10 km s^{-1} that we have used for radial-tangential macroturbulence gives our synthetic spectra a half-width consistent with those observed for most phases. A value of 16–20 km s^{-1} is required to broaden the synthetic spectra so that the maximum half-widths are similar to the maximum half-widths observed. However, an increase in radial-tangential macroturbulence to this amount has a significant effect on the line profiles. The asymmetry of the profiles is increased while γ is decreased. The A versus γ diagram for the synthetic spectra calculated with $\zeta = 20$ km s^{-1} is shown in Fig. 6.40, along with that for $\zeta = 10$ km s^{-1} (Fig. 6.41, a repeat of Fig. 5.10). If one imagines the negative-γ (negative radial velocity) part of Fig. 6.41 with the positive-γ (positive radial velocity) part of Fig. 6.40 then one would obtain a diagram similar to those observed in W Sgr, β Dor and S Nor (Figs 3.6,3.12 and 3.18). Of course

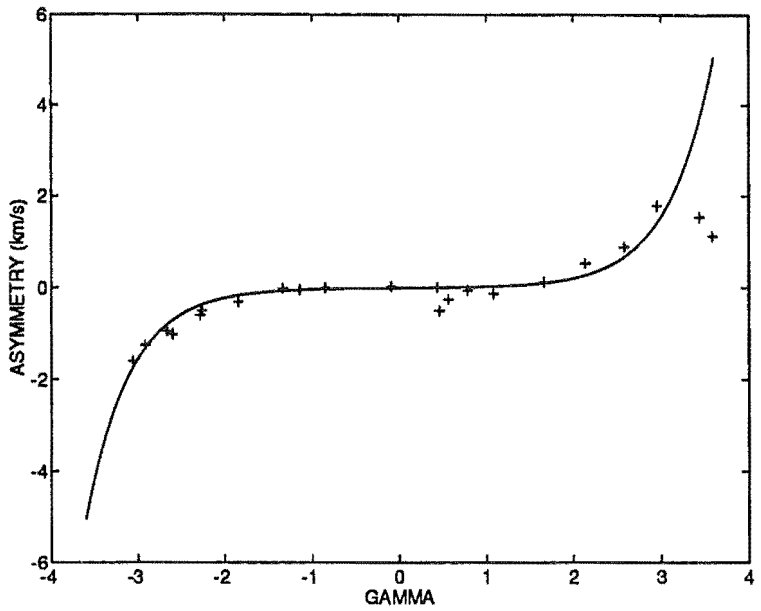

Figure 6.41: As in Fig. 6.40, but for $\zeta = 10$ km s^{-1}. (Same as Fig. 5.10.)

a detailed model for phase dependent turbulence would be required to do this properly, although the explaination seems plausible.

It is interesting to note that the effect of increasing asymmetry does not occur if the macroturbulence is isotropic rather than radial-tangential in nature. In this case a decrease is seen in both γ and asymmetry as the turbulence is increased. This is perhaps a more intuitive result than the radial-tangential one. The enhanced asymmetry observed in Cepheids is perhaps evidence for the reality of non-isotropic macroturbulence. We would recommend that isotropic models of turbulent broadening not be used for the interpretation of spectroscopic observations of Cepheids.

Chapter 7

Summary and future work

7.1 Summary

Using the new grid of static model atmospheres of Kurucz (1992), projection factors have been calculated for transforming Cepheid radial velocities into pulsational velocities. Models of isotropic, radial and radial-tangential macroturbulence have been used to broaden the line profiles. Calculations have been made for radial velocities measured at depths of 0.5 and 0.9 in the line profile. As shown by Parsons (1972), the projection factor depends strongly on γ, the ratio of pulsational velocity to spectral line half-width. The projection factors calculated are somewhat greater than those obtained by previous authors. The computations of Karp (1975b) have been shown to be flawed because an incorrect method was used to broaden the line profiles. The discrepancy between our results and those of Parsons (1972) are perhaps due to differences in the model atmospheres. Comparisons with the projection factors derived by Hindsley & Bell (1986) are difficult because one suspects their results to be rather dependent on the details of the mask used for their cross-correlation computations.

The asymmetry, A, of a spectral line has been defined to be the difference between the radial velocities measured at depths of 0.9 and 0.5 in the line profile. Asymmetries have been measured from the synthetic line profiles and have been found to depend on γ. The relationship found is significant because it allows comparison of Cepheid line profile asymmetries with those expected from geometric projection of a spatially-constant radial motion.

An ongoing programme of high resolution spectroscopic observations of Cepheids has been in progress for several years at Mt John University Observatory.

A survey has been made of the radial velocities and asymmetries of Hα and a moderate strength Fe I line for seven of the programme stars with reasonably complete phase coverage. The profiles of the Fe I line show a larger asymmetry than the synthetic profiles at phases of inward pulsation. The asymmetry at phases of outward velocity is smaller and in agreement with the synthetic profiles for some Cepheids. For others, however, the asymmetry at phases of outward pulsation is in the direction expected for inward motion.

A hydrodynamic model of an 11-day Cepheid has been calculated. A set of flux-constant, line-blanketed model atmospheres have been converged based on the density and effective gravity structure of the hydrodynamic model at different phases. A method for calculating the source function and mean intensity of the radiation field in a dynamic atmosphere has been derived and used to calculate synthetic profiles of the previously studied Fe I line. Radial velocity curves derived from the line profiles are more similar in shape to the 7-day Cepheid W Sgr than to any of the 10-day Cepheids observed.

A function has been derived which gives the relative contribution of different layers of a model atmosphere to the depression in flux of a spectral line. The flux contribution contour diagram is introduced as a means of studying the effects of velocity fields on the region of formation of spectral lines.

A static atmosphere has characteristic concentric V-shaped contours centered on zero velocity, with the line core forming at shallower layers than the wings. A constant non-zero velocity field Doppler shifts the core in wavelength space but has only a small effect on its formation depth. However, the region of formation of the trailing wing of the line is moved to much shallower layers, further out even than the core.

In the presence of a velocity gradient, the contours tend to follow the velocity. This can often result in the occurrence of more than one centre of absorption, separated in wavelength space and also in physical depth. This is likely when the velocity field is non-monotonic. Such multiple absorption centres will not usually be resolved in spectral observations. Velocity gradients of 10 km s^{-1} can have quite large effects on the location of line formation regions. The mapping of atmospheric velocity fields by using lines of different strength and excitation potential should be approached with caution. The depths of line formation are likely to be quite different than if the atmosphere was at rest.

The projection factors derived in Chapter 2 were used to map radial velocities

from the synthetic spectral lines back onto the hydrodynamic model. The projected radial velocities matched the pulsational velocity of a best fit mass zone with an rms error of $\sim$ 1.4 km s^{-1}. This could be reduced to $\sim$ 1.0 km s^{-1} if phases of bumps on the radial radial velocity curve were avoided.

A projection of the radial velocities onto the velocity of the photosphere was rather worse, with rms velocity differences of $\sim$ 5 km s^{-1}. This was due to the photospheric radius being at deeper layers than the line formation region. Both of these moved through mass zones with phase but not in unison. This resulted in a temporally changing phase lag between the motion of the photospheric radius and the projected radial velocities. In particular, the projected radial velocities significantly overestimated the photospheric velocity near radial velocity maximum. It is recommended that a phase gap of $\sim$ 0.1 around radial velocity maximum be excluded from Baade-Wesselink solutions.

Some investigation has been carried out into the question of the inverse and enhanced asymmetries observed in Cepheids. An inverse or negative asymmetry can result if there are velocity gradients of $\gtrsim$ 10 km s^{-1} through the region of line formation in the stellar atmosphere. Such an asymmetry can also be caused by the effects of radial macroturbulence. We have found no macroscopic radial velocity field which can result in the enhanced asymmetry observed at phases of inward motion. An increase in macroturbulence at these phases may be responsible, but only if the turbulence is non-isotropic.

7.2 Future work

There are several areas addressed in this thesis for which further work would be useful. There are a number of additional Cepheids being observed in an ongoing programme at Mt John which will add data to our survey of line profile asymmetries. These observations are essential to provide constraints for models of atmospheric velocities and turbulent broadening. As models become more sophisticated, our observations need to be obtained with higher signal to noise ratios and higher spectral resolution. This may mean that even well studied objects need to be reobserved.

Calculations of projection factors and line asymmetries from static models need to be made for higher values of macroturbulence and other macroturbulent models. More study is required of the phase dependence of turbulence in Cepheids, particularly of the form of the turbulence.

Thus far we have only created a series of model atmospheres based on one hydrodynamic model. Further sets of model atmospheres based on hydrodynamic models of Cepheids with different periods, masses, luminosities and metallicities would be useful to explore the effect of these changing parameters on line profiles. Sets of such models would also enable investigation of dynamic effects in colour – effective temperature calibrations and (in particular) abundance determinations.

Acknowledgements

Although a Ph.D. is in principle the work of an individual, in practice there are many people who make contributions. Thank you to my supervisor, Dr Peter Cottrell, for his advice and support. He was always ready to listen to problems and offer solutions with cheerful enthusiasm.

Mike Clark was responsible for taking many of the observations, setting up the telescope, spectrograph and detectors and helping to sort out equipment problems, often at ungodly hours.

Thank you to the others who took observations for this programme, Karen Pollard and Drs George Wallerstein and Warrick Lawson.

Thanks are due to Dr Peter Wood for his stellar pulsation code and Dr Bob Kurucz for providing his model atmosphere codes and grids of model atmospheres.

Useful conversations were held with several astronomers including Karen Pollard and Drs George Wallerstein, Bob Hindsley, Dave Latham and Dimitar Sasselov.

During the course of this work I was supported by a New Zealand University Grants Committee Scholarship (later to be known as a New Zealand Vice Chancellors' Committee Scholarship) and a William Georgetti Scholarship. Attendance at the XXIst General Assembly of the IAU in Buenos Aires, Argentina, and IAU Symposium 149 in Angra dos Reis, Brazil, in 1991 was made possible by grants from the IAU, the Kingdon-Tomlinson bequest of the Royal Astronomical Society of New Zealand, the Department of Physics and Astronomy of the University of Canterbury, the Young Scientists' Fund of the Royal Society of New Zealand, and the Canterbury Branch of the Royal Society of New Zealand. Grants were received from the IAU, the Frank Bradshaw and Elizabeth Pepper Wood Fund, the Kingdon-Tomlinson bequest and the New Zealand Institute of Physics towards attending IAU Colloquium 139 in Victoria, Canada, in 1992.

Thank you to the other members of the astronomy group for discussions and

distractions - John, William, Warrick, Kaylene, Karen, Steve, Alan, Lyndon, Donna, David, Frank, John, Irene, Ben and Saskia.

Thank you to my family and to my wife and best friend Karen.

References

Abt H.A., 1958, ApJ, 127, 658

Achmad L., de Jager C., Nieuwenhuijzen H., 1991, A&A, 250, 445

Albrow M.D., Cottrell P.L., 1994, MNRAS, 267, 548

Avrett E.H., Krook M., 1963, ApJ, 137, 874

Babel J., Burki G., Mayor M., Waelkens C., Chmielewski Y., 1989, A&A, 216, 125

Baker N.H., Kippenhahn R., 1962, Z. Astrophys, 54, 114

Baker N.H., Kippenhahn R., 1965, ApJ, 142, 868

Balona L.A., 1977, MNRAS, 178, 231

Barnes T.G., Evans D.S., Parsons S.B., 1976, MNRAS, 174, 503

Barnes T.G., Dominy J.F., Evans S.E., Kelton P.W., Parsons S.B., Stover R.J., 1977, MNRAS, 178, 661

Barnes T.G., Moffett T.J., Gieren W.P., 1993, ApJ, 405, L51

Bell R.A., Rodgers A.W., 1967, MNRAS, 135, 121

Belopolsky A.A., 1895, ApJ, 1, 366

Benz W., Mayor M., 1982, A&A, 111, 224

Bessell M.S., Brett J.M., Scholz M., Wood P.R., 1989a, A&A, 213, 209

Bessell M.S., Brett J.M., Scholz M., Wood P.R., 1989b, A&AS, 77, 1

Bevington P.R., 1969, Data reduction and error analysis for the physical sciences, McGraw-Hill, New York.

Böhm-Vitense E., 1958, Z.Astrophys, 277, 149

Böhm-Vitense E., 1964, In SAO Special Report, 167

Böhm-Vitense E., Clark M., Cottrell P.L., Wallerstein G., 1990, AJ, 99, 1

Breitfellner M.G., Gillet D., 1993a, A&A, 277, 524

Breitfellner M.G., Gillet D., 1993b, A&A, 277, 541

Breitfellner M.G., Gillet D., 1993c, A&A, 277, 553

Bowen G.H., 1988, ApJ, 329, 299

Bruzual A.G., 1992, in Barbuy B., Renzini A., eds, Proc. IAU Symp. 149, The Stellar Populations of Galaxies, Kluwer Academic Publishers, Dordrecht, p. 225

Butler R.P., 1993, ApJ, 415, 323

Campbell W.W., 1901, ApJ, 13, 90

Caccin B., Onnembo A., Russo G., Sollazzo C., 1981, A&A, 97, 104

Carson T.R., Stothers R.B., 1988, ApJ, 328, 196

Chandrasekhar S., 1945, Rev. Mod. Phys., 17, 138

Chiosi C., Wood P.R., Capitanio N., 1993, ApJS, 86, 541

Christy R.F., 1967, PASP, 79, 429

Côte P., Welch D.L., Mateo M., Fischer P., Madore B.F., 1991, AJ, 101, 1681

Cottrell P.L., Norris J., 1978, ApJ, 221, 893

Coulson I.M., Caldwell J.A.R., 1989, MNRAS, 240, 285

Cox J.P., 1963, ApJ, 138, 487

Cox J.P., 1974, Rep. Prog. Phys., 37, 563

Cox A.N., Brownlee R.R., Eilers D.D., 1966, ApJ, 144, 1024

Cox J.P., Cox A.N., Olsen K.H., King D.S., Eilers D.D., 1966, ApJ, 144, 1038

Deasy H.P., 1988, MNRAS, 231, 673

Deasy H., Butler C.J., 1986, Nature, 320, 726

Duval P., Karp A.H., 1978, ApJ, 222, 220

Eddington A.S., 1918a, MNRAS, 79, 2

Eddington A.S., 1918b, MNRAS, 79, 177

Evans N.R., 1991, ApJ, 372, 597

Evans N.R., 1992a, ApJ, 384, 220

Evans N.R., 1992b, ApJ, 389, 657

Feast M.W., Walker A.R., 1987, Ann. Rev. Astron. Astrophys, 25, 345

Fernie J.D., 1969, PASP, 81, 707

Fernie J.D., 1990, PASP, 102, 905

Fernie J.D., Kamper K.W., Seager S., 1993, ApJ, 416, 820

Fokin A.B., 1991, MNRAS, 250, 258

Fox M.W., Wood P.R., 1982, ApJ, 259, 198

Fraley G.S., 1968, A&SS, 2, 96

Gautschy A., 1987, Vistas in Astron., 30, 197

Gieren W.P., Barnes T.G., Moffett T.J., 1989, ApJ, 342, 467

Gieren W.P., 1989, A&A, 225, 381

Gray D.F., 1992, The Observation and Analysis of Stellar Photospheres, 2nd edn. Cambridge University Press, Cambridge

Gray D.F., Toner C.G., 1986, PASP, 98, 499

Gustafsson B., Bell R.A., Eriksson K., Nordlund A., 1975, A&A, 42, 407

Harris H.C., Welch D.L., 1989, AJ, 98, 981

Hearnshaw J.B., 1978, Sky&Telesc, 56, 6

Hearnshaw J.B., 1986, The Analysis of Starlight, Cambridge University Press, Cambridge

Hindsley R., Bell R.A., 1986, PASP, 98, 881

Hindsley R., Bell R.A., 1989, ApJ, 341, 1004

Huebner W.F., Merts A.L., Magee N.H., Argo M.F., 1977, Los Alamos Scientific Laboratory Report LA-6760-M

Hummer D.G., Rybicki G.B., 1968, ApJ, 153, L107

Iglesias C.A., Rogers F.J., 1991a, ApJ, 371, 408

Iglesias C.A., Rogers F.J., 1991b, ApJ, 371, L73

Jacobsen T.S., 1974, ApJ, 191, 691

Karp A.H., 1973, ApJ, 180, 895

Karp A.H., 1975a, ApJ, 199, 448

Karp A.H., 1975b, ApJ, 201, 641

King D.S., Cox J.P., Eilers D.D., 1966, ApJ, 144, 1069

Kovacs G., Buchler J.R., 1990, in Cacciari C., Clementini G., eds, ASP Conf. Ser., Confrontation Between Stellar Pulsation and Evolution. Astron. Soc. Pac., San Fransisco, p. 226

Kovacs G., Kisvarsanyi E.G., Buchler J.R., 1990, ApJ, 351, 606

Kraft, R.P., 1966, ApJ, 144, 1008

Kunasz P.B., Hummer D.G., 1974, MNRAS, 166, 57

Kurucz R.L., 1969, ApJ, 156, 235

Kurucz R.L., 1970, SAO Special Report, 309

Kurucz R.L., 1979, ApJS, 40, 1

Kurucz R.L., 1991, in Crivellari L., Hubeny I., Hummer D.G., eds, NATO ASI Ser., Stellar Atmospheres: Beyond Classical Models, Kluwer Academic Publishers, Dordrecht

Kurucz R.L., 1992, in Barbuy B., Renzini A., eds, Proc. IAU Symp. 149, The Stellar Populations of Galaxies, Kluwer Academic Publishers, Dordrecht, p. 225

Lambert D.L., 1968, MNRAS, 138, 143

Lambert D.L., Warner B., 1968, MNRAS, 138, 181

Laney C.D., Stobie R.S., 1993, MNRAS, 260, 408

Luck E.R., Bond H.E., 1989, ApJ, 342, 476

Luck E.R., Lambert D.L., 1981, ApJ, 245, 1018

MacQueen P.J., 1986, PhD thesis, University of Canterbury

Magain, P., 1986, A&A, 163, 135

McAlary C.W., Welch D.L., 1986, AJ, 91, 1209

Mermilliod J.C., Mayor M., Burki G., 1987, A&AS, 70, 389

Mihalas D., Kunasz P.B., Hummer D.G., 1975, ApJ, 202, 465

Moffett T.J., 1989, in Schmidt E.G., ed, Proc. IAU Colloq. 111, The Use of Pulsating Stars in Fundamental Problems of Astronomy. Cambridge University Press, Cambridge, p. 191

Oke J.B., Giver L.P., Searle L., 1962, ApJ, 136, 393

Opolski A., 1988, AcA, 38, 375

Oudmaijer R.D., Van der Veen W.E.C.J., Waters L.B.F.M., Trams N.R., Waelkens C., Engelsman E., 1992, A&AS, 96, 625

Parsons S.B., 1972, ApJ, 174, 57

Rogers A.W., Bell R.A., 1968, MNRAS, 138, 23

Rogers F.J., Iglesias C.A., 1992, ApJS, 79, 507

Ross J.E., Aller L.E., 1976, Science, 191, 1223

Sasselov D.D., Lester J.B., 1990, ApJ, 362, 333

Sasselov D.D., Lester J.B., 1994a, ApJ, in press

Sasselov D.D., Lester J.B., 1994b, ApJ, in press

Sasselov D.D., Lester J.B., 1994, ApJ, in press

Sasselov D.D., Lester J.B., Fieldus M.S., 1989, ApJ, 337, L29

Sasselov D.D., Raga A., 1992, in Giampapa M.S., Bookbinder J.A., eds, ASP Conf. Ser., Seventh Cambridge Workshop on Cool Stars, Stellar Systems, and the Sun, Astron. Soc. Pac., San Fransisco, p. 549

Schmid-Burgk J., Scholz M., 1984, in Kalkofen W., ed, Methods in Radiative Transfer, Cambridge University Press, Cambridge, p. 381

Shobbrook R.R., 1992, MNRAS, 255, 486

Stappers B.W., 1993, BSc(Hons) Project Report, University of Canterbury

Stobie R.S., 1969a, MNRAS, 144, 461

Stobie R.S., 1969b, MNRAS, 144, 485

Stobie R.S., 1969c, MNRAS, 144, 511

Szabados L., 1989, Comm. Konkoly Obs., 11, part 1, No. 94

Tobin W., 1991, Mt John Photometrics CCD System Use and Performance Note, 8

Tobin W., 1993, Mt John Photometrics CCD System Use and Performance Note, 13

van Hoof A., Deurinck R., 1950, ApJ, 115, 166

Wallerstein G., 1972, PASP, 84, 656

Wallerstein G., 1983, PASP, 95, 422

Wallerstein G., Jacobsen T., Cottrell P.L., Clark M., Albrow,M., 1992, MNRAS, 259, 474

Wesselink A.J., 1946, Bull. Astr. Inst. Netherl., 10, 468

Wood P.R., 1974, ApJ, 190, 609

Appendix A

UNIX shells for FIGARO image reduction

```
#! /bin/csh
#
# IPREPGEN  a general shell for preparing a MJUO CCD echelle
#           image for reduction (rotate, bclean)
#
# written by Michael Albrow 18/12/91
#
# modified by PLC 22/3/92
#
# Usage:  iprepgen imagename & (& for background operation)
#
# Start figaro
figaro
#
# Orient the image correctly
echo Orienting $1
  rotate image=$1 output=$1
  rotate image=$1 output=$1
  rotate image=$1 output=$1
  purge $1
#
# Remove cosmic rays from image
echo Cleaning $1
bclean image=$1 auto=n output=$1 crsig=3 crfact=0.3 crminv=20 crp=4 \\
#

#! /bin/csh
#
#  ITRACK    a shell to divide the OBJECT image by its FLAT FIELD,
#            find the orders on the OBJECT image and correct distortions
#            in the ARC and OBJECT images using this information
#
#  written by Michael Albrow  19/12/91
#
```

```
#  modified by PLC 29/3/92
#
#  Usage: itrack object arc flat\_field
#
# Check for correct number of parameters
if ( $#argv != 3 ) then
  echo Usage: itrack object arc flat\_field
  exit
endif
#
# Startup figaro
figaro
#
# Display the image
echo Imaging object
image $1 ystart=1 yend=384 xstart=1 xend=576 low=0 high=5000 \\
#
# Get centre of each order interactively
echo Use cursor to mark centre of each order
icur
#
# Track orders
echo Tracking orders ..
sdist image=$1 col=8 tr=G wi=4 max=3 di=y so=y \\
#
#
# Divide the object by the flat field
echo Dividing by flat field
icdiv image=$3 fac=8000 out=$3
idiv image=$1 image1=$3 out=$1
echo Output written to $1
#
# Correct distortions in object and arc
echo Straightening object orders ..
cdist image=$1 ys=1 ye=384 out=$1{s} max=5 \\
echo Corrected object image written to $1{s}
echo Straightening arc orders ..
cdist image=$2 ys=1 ye=384 out=$2{s} max=5 \\
echo Corrected arc image written to $2{s}
#


#! /bin/csh
#
#  ICOL  a shell to select the rows to be used for spectrum and sky in
#        OBJECT and ARC images & collapse these images
#
#  written by Michael Albrow  19/12/91
#
#  modified by PLC 29/3/92
#
#  Usage: icol object arc
#
# Check for correct number of parameters
if ( $#argv != 2 ) then
```

```
  echo Usage: icol object arc
  exit
endif
#
# remove old versions of echselect.lis
unalias rm
rm echselect.lis*
# Startup figaro
figaro
#
# select rows for object
echo Selecting object rows ..
echselect image=$1 pre=n wh ms=37 md=-1 objout=$1{e} skyout=$1{k} \\
echo Object spectra written to $1{e}, sky to $1{k}
#
# select rows for arc
echo Selecting arc rows ..
echselect image=$2 pre=y wh ms=37 md=-1 objout=$2{e} skyout=temp \\
echo Arc spectra written to $2{e}, sky to temp
#
# remove sky files
rm temp*
#
# Example of how to subtract sky from OBJECT
echo Subtracting sky from object spectrum ..
isub $1{e} $1{k} $1{s}
echo Sky-subtracted spectrum written to $1{s}
#



#! /bin/csh
#
#  CALIBRATE   a shell which finds a dispersion solution for the ARC,
#              copies this to the OBJECT, rebins the OBJECT and
#              merges the OBJECT into a single spectrum and soft
#       plot the final spectrum
#
#  written by Michael Albrow  19/12/91
#
#  modified by PLC 29/3/92
#
#  Usage: calibrate object arc final\_name
#
# Check for correct number of parameters
if ( $#argv != 3 ) then
  echo Usage: calibrate object arc final\_name
  exit
endif
#
# Startup figaro
figaro
#
# Interactively find the dispersion solution
echo Selecting arc lines ..
echarc image=$2 ar=thar pre int=4 nc=3 si=1.5 wa=$2{1} \\
```

```
echo Wavelength data written to $2{1}
#
# Create structure in object file for wavelength solution
echo Creating structure in $1 for wavelength information ..
crobj obj=$1{.x} ty='Struct'
crobj obj=$1{.x.data[576,4]} ty='Double'
#
# Copy in the solution
echo Copying wavelength information to $1 ..
let $1{.x.data} = $2{1.z.data}
#
# Rebin data to 25 pts per angstrom
echo Rebinning data in $1 ..
scrunch sp=$1 lo=n ws=6100 we=6800 bi=17501 me=n qu ou=$1 \\
#
# Merge to a single spectrum
echo Merging to one spectrum ..
echmerge image=$1 out=$1{m} \\
echo Spectrum written to $1{m}
#
# Plot spectra to screen
splot $1{m} lin xs=6180 xe=6220 au \\
splot $1{m} lin xs=6350 xe=6390 au \\
splot $1{m} lin xs=6535 xe=6575 au \\
splot $1{m} lin xs=6725 xe=6765 au \\
#
# Example for extracting separate spectra
# echo Subsetting spectrum ...
# isubset image=$1{m} xs=6185 xe=6220 out=$3{a}
# echo Written $3{a}
#
# Example for plotting spectra and making hard copies
# echo Plotting spectra ..
# splot $3{a} lin wh au label=$3{a} bu \\
# bplot soft
# bplot hard
# mv pgplot.ps $3{a.ps}
# echo Written $3{a.ps}
#
```

Appendix B

Parameters measured from the 6546 Å Fe I line.

Table B.1: W Sgr

Phase	JD +2440000	W_λ (Å)	v(0.5) (km s^{-1})	v(0.9) (km s^{-1})	HWHH (km s^{-1})	γ (km s^{-1})
0.013	7308.879	0.1178	-45.03	-45.04	11.603	-2.046
0.064	7256.105	0.1401	-43.12	-43.09	11.527	-1.827
0.097	7241.168	0.1439	-41.87	-41.72	11.183	-1.727
0.234	7242.207	0.1476	-35.67	-35.73	10.031	-1.060
0.284	7310.941	0.1498	-34.67	-34.54	9.487	-0.973
0.389	7304.141	0.1818	-29.38	-28.76	10.141	-0.180
0.415	7311.934	0.2034	-30.40	-30.24	10.711	-0.304
0.465	7221.180	0.1876	-30.35	-30.25	9.747	-0.327
0.494	7244.180	0.2119	-29.25	-29.47	9.558	-0.172
0.541	7312.895	0.2018	-25.32	-25.07	9.751	0.396
0.577	8141.012	0.1871	-22.82	-22.44	9.994	0.736
0.599	7222.195	0.1926	-19.53	-19.06	9.913	1.207
0.674	7313.906	0.2010	-12.85	-12.03	10.563	2.018
0.707	8141.992	0.1964	-9.45	-8.23	12.194	2.138
0.715	8104.082	0.1988	-9.67	-8.52	13.338	1.932
0.732	7223.207	0.2242	-7.29	-6.44	13.245	2.197
0.799	7254.090	0.2104	-5.42	-4.17	15.036	2.109
0.806	8195.910	0.2092	-4.63	-3.57	14.704	2.232
0.831	7239.152	0.1965	-8.81	-7.84	15.676	1.721
0.854	8105.141	0.1943	-15.85	-13.59	17.678	0.968
0.882	7247.129	0.1850	-24.74	-24.18	13.288	0.351
0.895	7307.984	0.1661	-28.20	-28.13	12.628	-0.014
0.930	7255.090	0.1456	-36.94	-37.18	12.214	-1.016

Table B.2: β Dor

Phase	JD +2440000	W_λ (Å)	v(0.5) (km s^{-1})	v(0.9) (km s^{-1})	HWHH (km s^{-1})	γ (km s^{-1})
0.021	7253.836	0.1599	1.41	1.65	10.942	-0.921
0.022	7184.949	0.1525	2.33	2.16	10.263	-0.857
0.078	7224.875	0.1644	-1.66	-1.85	11.482	-1.252
0.111	7116.930	0.1862	-3.62	-5.19	13.472	-1.271
0.124	7185.953	0.1759	-5.23	-5.66	11.417	-1.697
0.124	7254.852	0.1761	-5.16	-5.46	10.764	-1.791
0.154	8200.027	0.1954	-5.92	-5.76	11.650	-1.746
0.182	7225.902	0.1853	-4.17	-4.32	11.266	-1.588
0.227	7255.867	0.1881	-1.13	-1.31	9.947	-1.371
0.259	7275.867	0.1960	1.25	1.18	9.511	-1.084
0.265	8142.055	0.1712	1.85	1.77	9.827	-0.963
0.266	7216.879	0.2061	2.07	1.92	9.599	-0.954
0.280	7226.859	0.1945	3.86	3.91	9.552	-0.696
0.281	7089.078	0.2096	3.92	3.93	9.598	-0.684
0.365	7217.855	0.2234	11.94	12.22	9.818	0.475
0.379	7217.988	0.2270	12.43	12.74	9.771	0.547
0.398	7100.070	0.1831	13.51	14.27	9.044	0.758
0.466	7218.848	0.2271	20.71	21.55	10.659	1.589
0.485	7219.035	0.2259	22.52	23.07	11.131	1.749
0.511	7179.922	0.2078	22.46	23.25	12.559	1.544
0.515	7179.961	0.2375	23.63	24.43	11.412	1.842
0.521	8105.211	0.2142	24.49	25.28	11.929	1.864
0.542	8194.000	0.2107	25.80	26.60	11.970	2.010
0.570	7219.871	0.2287	26.29	27.24	13.325	1.857
0.620	7180.996	0.2578	24.50	26.17	15.100	1.473
0.621	8106.199	0.2302	26.72	28.03	14.722	1.722
0.678	7220.938	0.2159	20.79	21.96	14.720	1.158
0.686	7093.070	0.2193	18.89	19.29	14.323	1.005
0.719	7181.973	0.2280	12.81	13.47	13.989	0.420
0.741	8195.961	0.1935	10.88	10.86	12.708	0.250
0.770	7221.848	0.2072	6.90	7.44	12.130	-0.198
0.788	7222.023	0.2137	5.25	5.42	12.369	-0.380
0.883	7222.961	0.1939	1.43	1.66	11.169	-0.900
0.921	7183.957	0.1771	1.13	1.15	10.091	-1.038
0.979	7223.906	0.1489	2.04	1.91	10.077	-0.913

Table B.3: S Nor

Phase	JD +2440000	W_λ (Å)	v(0.5) (km s^{-1})	v(0.9) (km s^{-1})	HWHH (km s^{-1})	γ (km s^{-1})
0.008	8105.992	0.1483	-1.96	-2.19	10.934	-0.930
0.027	7325.832	0.1724	-1.63	-1.30	11.064	-0.877
0.082	7306.863	0.1821	-4.89	-5.07	11.576	-1.233
0.112	8106.988	0.2016	-8.53	-8.58	12.009	-1.613
0.136	7317.141	0.1987	-7.90	-8.13	11.844	-1.561
0.187	7307.895	0.1903	-6.48	-7.08	10.880	-1.516
0.228	7318.039	0.2039	-3.01	-2.93	10.610	-1.097
0.284	7308.844	0.2001	1.51	1.60	10.216	-0.520
0.285	7221.063	0.1921	1.71	1.98	10.012	-0.502
0.326	8196.891	0.2291	6.63	6.59	9.670	0.192
0.379	8285.188	0.2300	8.22	8.37	8.545	0.478
0.392	8099.984	0.1939	11.91	11.59	9.888	0.935
0.394	7222.117	0.2292	11.25	12.10	10.552	0.789
0.445	7242.129	0.2507	15.37	16.65	11.006	1.281
0.502	7223.176	0.2510	20.62	22.19	12.626	1.698
0.593	7311.855	0.2430	24.32	26.29	14.882	1.789
0.635	8199.891	0.2718	21.02	21.31	17.716	1.242
0.650	7244.129	0.2379	20.28	21.62	15.717	1.334
0.667	7254.043	0.2523	17.36	18.99	17.258	0.978
0.690	8141.902	0.2139	14.15	14.33	14.063	0.881
0.769	7255.043	0.2115	1.30	0.96	12.713	-0.441
0.797	7304.082	0.1854	-1.50	-1.29	12.307	-0.774
0.847	7323.961	0.1811	-2.47	-2.63	11.449	-0.951
0.897	7305.055	0.2098	-2.78	-2.84	11.294	-1.002
0.903	8104.957	0.1747	-2.04	-1.71	11.013	-0.933
0.953	7247.074	0.1748	-1.84	-1.98	10.822	-0.924
0.988	7305.949	0.1702	-2.63	-2.13	12.065	-0.921

Table B.4: S Mus

Phase	JD +2440000	W_λ (Å)	v(0.5) (km s^{-1})	v(0.9) (km s^{-1})	HWHH (km s^{-1})	γ (km s^{-1})
0.010	8007.844	0.1588	-11.17	-11.04	12.889	-1.158
0.012	8036.836	0.1548	-12.02	-11.71	11.679	-1.379
0.056	7959.984	0.2147	-9.61	-9.57	12.297	-1.036
0.057	8104.895	0.1478	-12.00	-11.79	11.856	-1.357
0.068	7225.957	0.1741	-11.17	-11.48	13.248	-1.127
0.075	7254.996	0.1632	-10.98	-10.78	11.692	-1.254
0.123	8095.875	0.1563	-9.48	-9.34	11.389	-1.103
0.163	8105.922	0.2402	-7.93	-7.31	12.680	-0.820
0.164	7226.883	0.1817	-6.34	-6.78	11.516	-0.709
0.181	7256.020	0.1759	-8.09	-7.81	11.463	-0.925
0.221	8038.867	0.1480	-7.12	-7.20	10.949	-0.845
0.222	8096.832	0.1459	-7.71	-7.13	11.799	-0.855
0.223	8009.902	0.1420	-5.95	-6.02	11.094	-0.686
0.249	7247.020	0.1625	-7.05	-6.73	11.114	-0.824
0.250	7304.992	0.1602	-6.35	-6.26	10.848	-0.753
0.258	8106.832	0.1706	-7.56	-7.25	12.186	-0.810
0.263	7961.984	0.1722	-4.89	-4.86	11.154	-0.550
0.315	7324.941	0.1832	-6.46	-6.16	11.936	-0.698
0.316	7943.176	0.1803	-8.83	-8.80	11.854	-0.982
0.365	7219.145	0.2453	-7.64	-7.32	13.292	-0.751
0.400	8001.961	0.1958	-7.39	-7.10	11.175	-0.862
0.413	7296.902	0.2081	-7.58	-7.68	12.880	-0.769
0.426	7239.066	0.2085	-6.02	-5.92	11.261	-0.685
0.439	7306.816	0.1916	-5.90	-5.70	10.908	-0.692
0.496	8002.883	0.1772	0.33	0.95	10.902	0.108
0.501	8196.121	0.2129	1.55	1.67	11.605	0.248
0.504	7317.102	0.2146	-0.25	0.04	11.110	0.033
0.541	8099.906	0.2026	3.86	3.71	10.837	0.564
0.558	7221.020	0.2102	5.06	5.74	11.339	0.688
0.594	8197.016	0.2153	7.57	8.78	11.848	0.955
0.596	7317.984	0.2220	7.15	8.06	11.538	0.930
0.606	8032.914	0.2513	8.27	9.20	12.761	0.963
0.629	7241.031	0.2314	10.33	11.45	11.668	1.301
0.641	8100.875	0.2337	12.29	13.35	12.812	1.399
0.645	8013.973	0.1710	9.19	10.45	12.838	1.058
0.651	7221.926	0.2623	12.41	13.54	12.588	1.437
0.666	7251.051	0.3430	12.49	13.32	15.524	1.172
0.672	7685.801	0.2105	15.47	16.56	12.599	1.775
0.736	7242.059	0.2041	17.18	18.03	13.431	1.844
0.764	7223.020	0.2434	16.57	18.25	14.711	1.625
0.822	7358.816	0.2018	12.68	13.16	13.582	1.360
0.862	7223.957	0.2916	6.12	6.53	16.337	0.569
0.862	7310.902	0.2084	5.81	6.46	13.972	0.633
0.870	8276.965	0.2031	4.53	5.52	13.884	0.508
0.882	8141.840	0.1789	4.20	3.98	13.575	0.485
0.914	8200.109	0.1893	-3.57	-3.53	14.693	-0.291
0.943	7244.082	0.1732	-8.70	-8.59	13.472	-0.851
0.950	7736.785	0.1694	-8.24	-8.32	12.975	-0.834
0.961	7224.914	0.2605	-9.21	-8.91	14.156	-0.861
0.971	7253.992	0.2238	-11.25	-10.81	13.853	-1.086

Table B.5: Y Oph

Phase	JD +2440000	W_λ (Å)	v(0.5) (km s^{-1})	v(0.9) (km s^{-1})	HWHH (km s^{-1})	γ (km s^{-1})
0.241	7358.891	0.2621	-16.97	-16.41	12.663	-0.914
0.262	7444.887	0.2176	-13.60	-12.98	11.132	-0.616
0.316	7325.914	0.2256	-10.84	-10.52	10.197	-0.294
0.331	8096.891	0.2329	-8.58	-8.00	10.683	0.016
0.370	7343.969	0.2215	-8.06	-7.67	10.165	0.088
0.443	7310.969	0.2362	-5.14	-4.58	10.908	0.457
0.501	7311.969	0.2350	-2.87	-1.96	11.388	0.717
0.565	7313.059	0.2488	-0.68	0.16	11.492	0.977
0.617	7313.953	0.2536	-0.13	0.93	12.314	0.974
0.754	8378.160	0.2199	-2.52	-2.22	11.958	0.724
0.807	8105.035	0.2023	-4.34	-3.51	11.940	0.511
0.858	7318.082	0.1964	-6.90	-6.76	11.755	0.214
0.867	8106.070	0.1852	-6.80	-6.53	12.109	0.220
0.905	8140.969	0.1601	-10.35	-9.99	11.079	-0.209
0.918	8106.922	0.1607	-10.54	-10.55	11.271	-0.229
0.930	7404.949	0.1660	-11.61	-11.02	11.888	-0.343
0.971	7439.895	0.1852	-12.24	-11.63	12.065	-0.411

Table B.6: κ Pav

Phase	JD +2440000	W_λ (Å)	v(0.5) (km s^{-1})	v(0.9) (km s^{-1})	HWHH (km s^{-1})	γ (km s^{-1})
0.066	8193.977	0.1912	34.30	34.68	9.477	-0.494
0.083	7222.215	0.2339	36.20	36.70	10.329	-0.196
0.172	7241.191	0.2442	40.04	40.76	10.151	0.330
0.173	8104.109	0.1989	38.53	38.71	10.285	0.120
0.195	7223.227	0.3007	40.61	41.22	10.497	0.395
0.241	8141.059	0.2480	42.32	42.92	10.161	0.644
0.283	8195.941	0.2533	43.64	44.41	10.211	0.822
0.287	7242.227	0.2448	45.31	46.10	10.840	0.990
0.289	8105.168	0.2181	44.52	44.84	10.245	0.939
0.346	8142.020	0.2098	47.17	47.36	11.264	1.184
0.380	7324.832	0.2471	50.03	50.56	10.696	1.621
0.395	8196.961	0.2679	48.66	48.87	10.686	1.443
0.399	8106.168	0.2286	50.12	50.55	10.599	1.648
0.407	7306.902	0.2675	50.96	51.41	11.143	1.673
0.475	7243.938	0.2086	52.80	53.30	11.584	1.831
0.528	7308.008	0.1886	52.48	53.96	14.194	1.463
0.594	7254.109	0.2073	45.78	42.28	22.265	0.511
0.626	7308.898	0.1431	33.28	32.51	13.697	-0.446
0.705	7255.109	0.1533	24.70	25.51	11.295	-1.605
0.729	8199.996	0.1831	24.88	24.43	14.320	-1.248
0.731	8100.098	0.1007	26.17	26.47	10.745	-1.495
0.766	8282.078	0.1395	25.04	25.90	12.784	-1.380
0.811	7346.902	0.1378	24.80	25.73	10.731	-1.676
0.816	7256.125	0.1621	25.47	26.61	10.523	-1.620
0.864	8282.973	0.1235	23.41	24.39	9.836	-2.026
0.883	8283.145	0.1228	23.70	24.63	10.003	-1.952
0.944	7239.121	0.2148	31.27	31.77	9.763	-0.914
0.949	8192.910	0.1666	29.19	29.58	9.552	-1.239
0.972	7221.207	0.2047	31.41	32.10	10.079	-0.866

Table B.7: U Car

Phase	JD +2440000	W_λ (Å)	v(0.5) (km s^{-1})	v(0.9) (km s^{-1})	HWHH (km s^{-1})	γ (km s^{-1})
0.015	7943.070	0.3533	22.78	24.09	18.711	1.495
0.044	7323.906	0.3470	22.63	23.57	17.029	1.630
0.059	8099.828	0.3527	23.90	23.95	18.508	1.596
0.069	7324.883	0.2965	22.49	23.09	17.172	1.605
0.133	8723.021	0.2139	20.48	20.06	15.970	1.550
0.150	8142.141	0.1937	4.50	2.82	19.587	0.122
0.188	8104.844	0.1280	-17.00	-18.38	18.186	-1.524
0.210	8726.001	0.1071	-16.87	-20.57	14.885	-1.850
0.214	8105.852	0.1376	-21.28	-22.64	17.890	-1.884
0.263	8728.042	0.1285	-23.70	-24.59	12.538	-2.959
0.345	8576.165	0.1692	-18.16	-19.27	13.407	-2.189
0.384	8345.066	0.2086	-17.23	-17.48	10.180	-2.755
0.389	8694.175	0.1802	-18.33	-18.57	11.280	-2.623
0.539	8196.008	0.2499	-4.82	-4.30	10.587	-1.008
0.558	7343.863	0.2617	-1.74	-1.73	9.804	-0.648
0.639	8471.227	0.2548	1.31	2.06	9.950	-0.210
0.703	8590.042	0.2811	8.45	8.75	10.141	0.780
0.725	8397.052	0.3267	7.31	7.15	10.820	0.584
0.734	7311.902	0.3484	12.16	12.72	11.475	1.142
0.784	7313.859	0.3385	14.81	15.79	12.937	1.300
0.833	8595.073	0.3342	16.87	17.94	12.250	1.608
0.861	7316.848	0.3821	18.73	19.25	14.975	1.489
0.931	7242.000	0.4111	20.29	21.11	16.620	1.473

Appendix C

Pretabulation of coefficients for calculation of the source function

```
      program coeffs
c
c This calculates the matrix coefficients used by the SPECTRUM program
c to solve the mean intensity with an angular dependent source function.
c The theory is described a separate document.
c Note that the program should be compiled (NOT with the /G_FLOATING option)
c and linked to the NAG library. The /PARALLEL option can be used to
c take advantage of the VAX FORTRAN parallel processing facility.
c                                                          mda 30-11-89
c
c Linear interpolation routine added 20-03-90 (mda)
c Extended depth scale 11-10-91
c newparco routine added 16-10-91
c
c
      implicit real*8 (a-h,l,m-z)
      integer n,p,p0,tsign,psign
      real*8 t(44),mu(43)
cpar$ private ii,ir,ik,iw,tsign,psign,ppco,tpco,csum
cpar$ private mup,mup1,tj,tl,a,c,den,bfac,b,ifail,e0,e1,term0,term1
cpar$ private tdiff,tdiffexp,sum,beta,quo
cpar$ private j,k,i,tau,ntau,j12,x1,x2,x3,x4,d,xxd,parco
c
c
      data n/43/
      data p/41/
      data p0/10/
      data t/ 0.       , 0.000032 , 0.000056 ,
     1        0.0001   , 0.00018  , 0.00032  , 0.00056  , 0.001    ,
     1        0.0018   , 0.0032   , 0.0056   , 0.01     , 0.016    ,
     1        0.025    , 0.042    , 0.065    , 0.096    , 0.139    ,
     1        0.196    , 0.273    , 0.375    , 0.5      , 0.63     ,
     1        0.78     , 0.95     , 1.15     , 1.35     , 1.6      ,
     1        1.85     , 2.15     , 2.45     , 2.75     , 3.15     ,
```

```
     1        3.65     , 4.15     , 4.9      , 6.1      , 7.7      ,
     1       10.0      ,12.5      ,15.0      ,17.5      ,20.0      ,
     1     1020./
      data mu/ -0.95 ,
     1         -1.   ,-0.95 ,-0.9  ,-0.85 ,-0.8  ,-0.75 ,-0.7  ,
     1         -0.65 ,-0.6  ,-0.55 ,-0.5  ,-0.45 ,-0.4  ,-0.35 ,
     1         -0.3  ,-0.25 ,-0.2  ,-0.15 ,-0.1  ,-0.05 , 0.   ,
     1          0.05 , 0.1  , 0.15 , 0.2  , 0.25 , 0.3  , 0.35 ,
     1          0.4  , 0.45 , 0.5  , 0.55 , 0.6  , 0.65 , 0.7  ,
     1          0.75 , 0.8  , 0.85 , 0.9  , 0.95 , 1.   , 0.95/
c
c
      open(unit=1,status='old')
      read(1,*) jl1,jl2
      close(1)
      open(unit=10,status='new')
      do 600 jl=jl1,jl2
        do 600 jj=1,n
          do 600 jp=1,p
c Calculate coeff(jl,jp,jj) if non-zero.
            if ((jl.ge.jj+1.and.jp.le.22).or.(jl.gt.jj-2.and.jl.lt.
     1         jj+1).or.(jl.le.jj-2.and.jp.ge.20)) then
              coe=0.d0
cpar$         do_parallel
              do 500 ii=1,n
c for parco or newparco
c               if ((jj.ge.(ii-1)).and.(jj.le.(ii+2))) then
c for linco
                if ((ii.eq.jj).or.(ii.eq.(jj+1))) then
                  tsign=1
                  if (ii.lt.jl) tsign=-1
                  do 400 ik=1,3
c                   tpco=newparco(ii,ik,jj,t,n)
                    tpco=parco(ii,ik,jj,t,n)
c                   tpco=linco(ii,ik,jj,t,n)
                      do 400 ir=1,2
                        do 400 iw=1,p
                          psign=1
                          if (iw.le.20) psign=-1
                          if (psign.eq.tsign) then
c for parco or newparco
c                           if ((jp.ge.(iw-1)).and.(jp.le.(iw+2))) then
c for linco
                            if ((iw.eq.jp).or.(iw.eq.(jp+1))) then
c                             ppco=parco(iw+1,ir,jp+1,mu,p+2)
                              ppco=linco(iw+1,ir,jp+1,mu,p+2)
                              if (ppco.ne.0.) then
                                if (ik.ne.3) csum =
     1                            beta(ir+ik-1,mu(iw+1),mu(iw+2),
     1                            t(ii+1),t(jl)) - beta(ir+ik-1,mu(iw+1)
     1                            ,mu(iw+2),t(ii),t(jl))
                                if (ik.eq.2) csum = csum + t(ii+1)*
     1                            beta(ir,mu(iw+1),mu(iw+2),
     1                            t(ii+1),t(jl)) - t(ii)*beta(ir,
     1                            mu(iw+1),mu(iw+2),t(ii),t(jl))
                                if (ik.eq.3) csum = 2*beta(ir+2,mu(iw+1)
```

```
     1                          ,mu(iw+2),t(ii+1),t(jl)) - 2*beta(ir+2
     1                          ,mu(iw+1),mu(iw+2),t(ii),t(jl))+
     1                          t(ii+1)**2*beta(ir,mu(iw+1),mu(iw+2),
     1                          t(ii+1),t(jl)) - t(ii)**2*beta(ir,
     1                          mu(iw+1),mu(iw+2),t(ii),t(jl)) +2*
     1                          t(ii+1)*beta(ir+1,mu(iw+1),mu(iw+2),
     1                          t(ii+1),t(jl)) -2*t(ii)*beta(ir+1,
     1                          mu(iw+1),mu(iw+2),t(ii),t(jl))
                              coe = coe - tsign * csum * tpco * ppco
                            endif
                          endif
                        endif
400               continue
                  endif
500             continue
                if (coe.ne.0.d0) write(10,1000) jl,jp,jj,coe
1000            format(1X,3I4,2X,1D15.8)
              endif
600         continue
      close(10)
      end
c
c
c
      real*8 function beta(b,mup,mup1,tj,tl)
c
c  This is the function beta defined on page 4 of the document on
c  computing moments of the radiation field.
c  The NAG function S13AAF is used to calculate values of the
c  exponential integral.
c
      integer b
      real*8 mup,mup1,tj,tl
      integer a,c,den,bfac,ifail0,ifail1
      real*8 e0,e1,term0,term1,tdiff,tdiffexp,sum
      real quo
      beta=0.
      if (tj.eq.tl) then
        beta=(mup1**b-mup**b)/b/2.
        return
      endif
      tdiff=tj-tl
      e0=0.
      if (mup.ne.0.) then
        ifail=0
        quo=tdiff/mup
        e0=s13aaf(quo,ifail)
      endif
      e1=0.
      if (mup1.ne.0.) then
        ifail=0
        quo=tdiff/mup1
        e1=s13aaf(quo,ifail)
      endif
      sum=0.
      do 200 a=1,b
```

```
        term0=0.
        term1=0.
        if (mup.ne.0.) term0=mup**(b+1-a)*dexp(-tdiff/mup)
        if (mup1.ne.0.) term1=mup1**(b+1-a)*dexp(-tdiff/mup1)
        c=b
        den=1
100     if (c.ge.b+1-a) then
          den=den*c
          c=c-1
          goto 100
        endif
        tdiffexp=1.
        if (a.gt.1) tdiffexp=(-tdiff)**(a-1)
        sum=sum+tdiffexp*(term0-term1)/den
200   continue
      bfac=1
      do 300 c=1,b
300     bfac=bfac*c
      beta=((-tdiff)**b*(e1-e0)/bfac-sum)/2.
      return
      end
c
c
c
      real*8 function linco(j,k,i,tau,ntau)
      implicit real*8 (a-d,l,p-z)
      real*8 tau(*)
      linco=0.D0
      if (k.gt.2) return
      if ((i.gt.j+1).or.(i.lt.j)) return
      d=tau(j+1)-tau(j)
      co=1./d
      if (k.eq.1) then
        if (i.eq.j) then
          co=co*tau(j+1)
        else
          co=-co*tau(j)
        endif
      else
        if (i.eq.j) co=-co
      endif
      linco=co
      return
      end
c
c
c
      real*8 function newparco(j,k,i,tau,ntau)
c
c  half the sum of the forward and backward parabolic interpolation coeffs
c
      implicit real*8 (a-d,l,p-z)
      real*8 tau(*)
      newparco=0.D0
      if ((i.gt.j+2).or.(i.lt.j-1)) return
      if (k.gt.3) return
```

```
      d1=tau(j+1)**2*(tau(j)-tau(j-1))+tau(j)**2*(tau(j-1)-tau(j+1))
     1     +tau(j-1)**2*(tau(j+1)-tau(j))
      d2=tau(j+2)**2*(tau(j+1)-tau(j))+tau(j+1)**2*(tau(j)-tau(j+2))
     1     +tau(j)**2*(tau(j+2)-tau(j+1))
      if (j.eq.1) goto 100
      if (j.eq.ntau) goto 200
      if (i.eq.j-1) then
        if (k.eq.3) then
          newparco=(tau(j+1)-tau(j))/d1
        elseif (k.eq.2) then
          newparco=(tau(j+1)**2-tau(j)**2)/d1
        else
          newparco=(tau(j+1)**2*tau(j)-tau(j)**2*tau(j+1))/d1
        endif
      elseif (i.eq.j) then
        if (k.eq.3) then
          newparco=((tau(j-1)-tau(j+1))/d1+(tau(j+2)-tau(j+1))/d2)/2
        elseif (k.eq.2) then
          newparco=((tau(j-1)**2-tau(j+1)**2)/d1+
     1              (tau(j+2)**2-tau(j+1)**2)/d2)/2
        else
          newparco=((tau(j-1)**2*tau(j+1)-tau(j+1)**2*tau(j-1))/d1+
     1              (tau(j+2)**2*tau(j+1)-tau(j+1)**2*tau(j+2))/d2)/2
        endif
      elseif (i.eq.j+1) then
        if (k.eq.3) then
          newparco=((tau(j)-tau(j-1))/d1+(tau(j)-tau(j+2))/d2)/2
        elseif (k.eq.2) then
          newparco=((tau(j)**2-tau(j-1)**2)/d1+
     1              (tau(j)**2-tau(j+2)**2)/d2)/2
        else
          newparco=((tau(j)**2*tau(j-1)-tau(j-1)**2*tau(j))/d1+
     1              (tau(j)**2*tau(j+2)-tau(j+2)**2*tau(j))/d2)/2
        endif
      else
        if (k.eq.3) then
          newparco=(tau(j+1)-tau(j))/d2
        elseif (k.eq.2) then
          newparco=(tau(j+1)**2-tau(j)**2)/d2
        else
          newparco=(tau(j+1)**2*tau(j)-tau(j)**2*tau(j+1))/d2
        endif
      endif
      return

  100 if (i.eq.j) then
        if (k.eq.3) then
          newparco=(tau(j+2)-tau(j+1))/d2
        elseif (k.eq.2) then
          newparco=(tau(j+2)**2-tau(j+1)**2)/d2
        else
          newparco=(tau(j+2)**2*tau(j+1)-tau(j+1)**2*tau(j+2))/d2
        endif
      elseif (i.eq.j+1) then
        if (k.eq.3) then
          newparco=(tau(j)-tau(j+2))/d2
```

```
      elseif (k.eq.2) then
        newparco=(tau(j)**2-tau(j+2)**2)/d2
      else
        newparco=(tau(j)**2*tau(j+2)-tau(j+2)**2*tau(j))/d2
      endif
    else
      if (k.eq.3) then
        newparco=(tau(j+1)-tau(j))/d2
      elseif (k.eq.2) then
        newparco=(tau(j+1)**2-tau(j)**2)/d2
      else
        newparco=(tau(j+1)**2*tau(j)-tau(j)**2*tau(j+1))/d2
      endif
    endif
    return

200 if (i.eq.j-1) then
      if (k.eq.3) then
        newparco=(tau(j+1)-tau(j))/d1
      elseif (k.eq.2) then
        newparco=(tau(j+1)**2-tau(j)**2)/d1
      else
        newparco=(tau(j+1)**2*tau(j)-tau(j)**2*tau(j+1))/d1
      endif
    elseif (i.eq.j) then
      if (k.eq.3) then
        newparco=(tau(j-1)-tau(j+1))/d2
      elseif (k.eq.2) then
        newparco=(tau(j-1)**2-tau(j+1)**2)/d2
      else
        newparco=(tau(j-1)**2*tau(j+1)-tau(j+1)**2*tau(j-1))/d2
      endif
    else
      if (k.eq.3) then
        newparco=(tau(j)-tau(j-1))/d2
      elseif (k.eq.2) then
        newparco=(tau(j)**2-tau(j-1)**2)/d2
      else
        newparco=(tau(j)**2*tau(j-1)-tau(j-1)**2*tau(j))/d2
      endif
    endif
    return
    end
```